THE CRANFIELD INSTITUTE OF TECHNOLOGY

TURBOMACHINERY DEPARTMENT

SCHOOL OF MECHANICAL ENGINEERING

Ph.D Thesis

1986

K.O. Toolsie

THE PREDICTION OF TRANSONIC FLOWS USING A POTENTIAL METHOD

Supervisors: Dr. A. Goulas
Prof. R.L. Elder

26th September 1986

ACKNOWLEDGEMENTS

I would like to express my gratitude to my Supervisors, Dr. A. Goulas and Professor R.L. Elder, for their inspiration and encouragement throughout the course of this work. I also wish to thank Dr. M.E. Gill for her help with the Computer Systems and Mrs. L. Simmons for typing this report.

ABSTRACT

Transonic flows are simulated within convergent divergent nozzles and within turbomachinery blade rows. The flow is represented by the conservative full potential equation approximated by a nine-node central-difference scheme, which is third order accurate. Artificial viscosity is included into the central-difference approximation of the potential equation, in regions where the flow is locally supersonic. The appoximation of the potential equation by central-differences, with an artificial viscosity term included, is equivalent to the approximation by upwind-differences and ensures that the upwind nature of the domain of dependence of supersonic flows is correctly modelled. The exact form of this artificial viscosity term is derived and contains third order derivatives of velocity-potential. The inclusion of artificial-viscosity allows the potential equation to be approximated everywhere by central-differences and the flow equation is everywhere elliptic. The Neuman boundary-condition is applied, along solid surfaces, if an inviscid solution is desired. Viscous effects are incorporated by the modification of this condition so as to allow a transpiration flow through the solid surfaces. A standard Successive-Line-Over-Relaxation technique, developed for the solution of simultaneous elliptic equations, is used to solve the discretized potential flow equations. Predictions are presented for both the inviscid and the viscous-corrected potential codes applied to the simulation of transonic flow through nozzles and cascade blade-rows. Comparisons are made with other theoretical models and with experimental data. The problem of non-uniqueness is considered and an estimate of numerical error is made by the application of the inviscid code with two computational grids of different levels of refinement. The stability of this potential code is examined and is found to depend on the level of smearing of the shock discontinuity predicted by the theoretical model.

NOMENCLATURE

a,b,c,d,e,f,g, h,p,q,r	=	coefficients in the discretized potential flow equation speed of sound
a	=	speed of sound
An	=	A specific set of nine constants used in the central-difference approximation to the first order derivative of potential with respect to x
b	=	blockage factor
Bn	=	as An for the first order partial derivative with respect to y
c	=	axial chord or speed of sound
C_E	=	entrainment coefficient
C_f	=	skin friction coefficient
CFO	=	coefficient of unknown potential in the discretized flow equation
C_n	=	a general set of nine constants, different for each partial derivative for each node, used in the central-difference approximations
$C_{(n)}$	=	a set of constants to which the potentials along the inlet plane are set
C1,C2	=	constants
D_n	=	a general set of six constants used in the upwind approximations
	or	a specific set of six constants used in the upwind approximation to the second order partial derivative with respect to x
$D_{(n)}$	=	a set of constants to which the potentials along the exit plane are set

E	=	energy
E_n	=	a specific set of six constants used in the upwind approximation to the second order partial derivative with respect to x and y
f1,f2,f3	=	functions
F_n	=	a specific set of six constants used in the upwind approximation to the second order partial derivative with respect to y
H	=	shape factor of boundary layer
H1	=	ratio of mass flow thickness to momentum thickness
Iori	=	specifies that the node is on the I (or i) row from the inlet plane
Jorj	=	specifies that the node is on the J (or j) column from the bottom
K1	=	a constant
l	=	number of iterations completed or a boundary-layer parameter
L_1, L_2	=	a function
M	=	mach number or number of nodes on a column
Ms	=	mach number along solid surface
n,s	=	cartesian coordiantes aligned with a streamline or a solid surface
n	=	number of nodes per column
NP	=	total number of nodes at which the potential is unknown
p	=	static pressure
pb	=	back pressure
q	=	velocity
r,θ,z	=	polar coordinates in radial, tangential and axial directions respectively
R	=	gas constant
Re	=	Reynolds number

s	=	pitch spacing
S_{ij}	=	central-difference approximation to the potential flow equation on column i and row j
t	=	time
T	=	temperature
T_{ij}	=	artificial viscosity at node on column i and row j
u	=	component of velocity in the x-direction
U_s	=	velocity along a solid surface
$\tilde{U}_s$	=	dimensionless velocity along a solid surface
v	=	component of velocity in the y-direction
V	=	maximum velocity in the flow-field or velocity
V_t	=	transpiration velocity
w	=	velocity or relaxation factor
x,y	=	Cartesian coordinates
$\tilde{x}$	=	dimensionless distance
α	=	air-flow angle
γ	=	ratio of specific heats
δ^*	=	boundary-layer displacement thickness
Δ	=	mass flow thickness
Δl	=	minimum dimensional length of element in computational grid
Δp	=	pressure rise
Δt	=	time step
ΔV	=	change in velocity predicted across the shock

$\Delta x, \Delta y$	=	spacing between two nodes in the x and y-direction respectively
Δx_f	=	spacing between two nodes in the x-direction on a fine grid
λ	=	dimensionless pressure gradient parameter
μ	=	switching function or coefficient of absolute viscosity
ρ	=	density
ϕ	=	velocity potential
Σ	=	summation
θ	=	boundary-layer momentum thickness
$\tilde{\theta}$	=	dimensionless momentum thickness
∇	=	gradient operator

Subscripts

C.D.	=	central-difference approximation to
n,o	=	at node n and node o respectively
o	=	stagnation
s,n	=	partial derivative with respect to s and n respectively
t	=	partial derivative with respect to time
x,y	=	partial derivative with respect to x and y respectively
UPWIND	=	upwind-difference approximation to
z,θ	=	partial derivative with respect to z and θrespectively
∞	=	at infinity

1,2	=	at inlet plane and outlet plane respectively

Abreviations

A.D.I.	=	Alternating-Direction-Implicit
A.V.	=	Aritifical Viscosity
CAS-IN	=	The inviscid potential code used to solve for transonic flow in cascade
CAS-VI	=	The viscous-corrected potential code used to solve for transonic flow in cascades
C.D.	=	Central-Difference
C.F.L.	=	Courant-Friedrichs-Lewi
ln	=	natural logarithm of
L.B.I.	=	Linearized-Block-Implicit
L.H.S.	=	Left-Hand-Side
N.E.C.	=	Numerical Error of Coarse computational grid
N.E.F.	=	Numerical Error of Fine computational grid
P.D.	=	Partial Derivative
R.H.S.	=	Right-Hand-Side
S.L.O.R.	=	Successsive-Line-Over-Relaxation
3-D	=	Three-Dimensional
2D-IN	=	The Inviscid Potential code used to solve for transonic flow in nozzles
2D-VI	=	The viscous-corrected Potential code used to solve for transonic flow in nozzles

CONTENTS PAGE

CONTENTS contd.

CONTENTS contd. PAGE

FIGURES

Tables

INTRODUCTION

1.1 The Problem

Aircraft gas turbine engines are often required to minimize their frontal area and/or weight, for a given duty. Any increase in frontal area will have the effect of increasing the installation drag of the engine, whilst an increase in weight will reduce the range and increase the fuel burn of the aircraft it is powering. Engines incorporating centrifugal compressors, in particular, suffer from a major disadvantage in that they require a much larger frontal area than do similar engines with axial-flow compressors. The quest for reduced engine size and higher engine thrust-to-weight ratios has led to an increase in the air velocities through both types of engines. The result of this increase in air velocities has often been to force the airflow around the compressor and turbine blades into the transonic regime, characterised by mixed subsonic-supersonic flow conditions. In addition, the advent of aircraft designed to operate just below the speed of sound has resulted in the occurence of transonic flows around their wings and engine nacelles. Transonic flow are also now common around helicopter rotors, around propeller and fan blades and around many forms of weapons.

Transonic flows are usually accompanied by shock waves which may adversely effect the aerodynamic efficiency of the compressor, turbine or wing due to wave drag, viscous interaction and unsteady effects. It is important, therefore, for the designer of these components to have a thorough understanding of transonic flow and a means of transonic airfoil-, cascade-, and channel-flow analysis. It is desirable that this analysis is capable of providing a reliable flow field prediction and may be used in a systematic approach to minimize the adverse shock effects.

Windtunnel testing is very expensive and time-consuming and such testing of transonic flows is subject to much uncertainty. Numerical methods which can produce accurate predictions of the flow field around components operating in the transonic regime are, therefore, very desirable.

The major complexity of simulating transonic flows is due to the flow being of mixed type with regions of both subsonic and of supersonic flow co-existing. The location of the boundaries separating the different regions of flow is unknown and is required as part of the fluid-flow solution. The physical behaviour of inviscid supersonic flow is very different to that of inviscid subsonic flow. In the latter a local disturbance in the flow is propagated in all directions, being described mathematically by equations which are elliptic in nature. In supersonic flow, however, the effects of a local disturbance are restricted to a region downstream of the disturbance bounded by the Mach cone. Such flows are described mathematically by equations which are hyperbolic in nature. Any numerical simulation of transonic flows, which is required to represent the flow to a reasonable accuracy, must model the different natures of these two different types of flow.

A further difficulty in simulating transonic flows results from the presence of the shock wave. Across a normal shock the flow changes from supersonic to subsonic, and inbetween there exists a discontinuity in the physical properties of the flow. This discontinuity makes it difficult to satisfy all the relevant flow equations in the region of the shock wave. As the position of the shock is not known a priori it is neccessary to compute the flow-field solution throughout the complete physical space. Thus, a computational mesh with a large number of points is required with subsequent requirements for large amounts of computer storage and fast computing speeds.

1.2 Historical Advances in the Solution of Transonic Flows

In spite of much effort for over twenty years, no numerical solution of the transonic flow problem could be obtained without such drastic simplifications, either in the governing equations or in their solution, that important features of the real flow were lost. In recent years, however, significant advances have been made in the numerical prediction of transonic flows, stimulated not only by the requirement for accurate transonic predictions in a variety of aerodynamic situations but also by the availability of powerful modern digital computers.

The first major advance was made by Magnus and Yoshira [1] who used the increased power of the new computers to advance the transient solution of the transonic problem forward in time to an asymptotic steady-state. This reduced the mixed elliptic-hyperbolic problem to one that is entirely hyperbolic (in time). The real breakthrough, however, was achieved by Murman and Cole [2] in 1970, with the solution of the transonic small-perturbation (TSP) equation for the velocity potential in two dimensions:

$$\left[1 - M_\infty^2 - (\gamma+1)\phi_x\right]\phi_{xx} + \phi_{yy} = 0 \qquad (1)$$

Their success relied on a novel Finite Difference scheme which used central differences to approximate the gradients of velocity potential in regions where the flow was subsonic, and backward (upwind) differences in regions where the flow was supersonic. The central difference approximation to the derivatives at any point in the subsonic region was, therefore, a function of the velocity potential both upstream and downstream of that point. Any local disturbance in the subsonic region of flow was thus allowed to propogate in all directions. The backward difference scheme used to

approximate derivatives of velocity potential at all points in the supersonic regions of flow, was however, only a function of the velocity potential of points upstream of the point of interest. Any local disturbance in the supersonic region of flow was thus allowed only to propagate downstream in the local direction of the flow and could not influence the fluid properties at any points upwind of the disturbance. Additionally, line-relaxation (implicit along x = constant lines) was used to solve the resulting algebraic equations which approximate the differential flow equations. This solution technique removed the stability restrictions near the sonic line and gave the authors very encouraging results. This was then followed by the solution of the exact potential equation

$$(c^2 - u^2)\phi_{xx} - 2uv\phi_{xy} + (c^2 - v^2)\phi_{yy} = 0 \qquad (2)$$

by Garabedian and Korn [3] in 1971, using a similar switched differencing scheme to Murman and cole. The speed of sound, c, was defined by Bernoulli's Law:

$$(u^2 + v^2)/2 + c^2/(\gamma-1) = 1/2 + M^{-2}/(\gamma-1) \qquad (3)$$

since that point, there was an amazingly rapid growth in the capability for solving transonic flow problems on modern digital computers: The flow was solved in three-dimensions, more accurate equations were used to represent the flow, viscous-inviscid interaction was included, and accuracy and efficiency of the numerical methods were increased significantly. Essentially there are at present three major methods for solving transonic flows. These are, in order of increasing simplicity, the solution of the viscous full Navier-Stokes equations, the solution of the inviscid Euler equations and the solution of the inviscid, irrotational velocity-potential equations.

1.3 The Solution of the Navier-Stokes Equations

Internal transonic flows are most accurately represented by the full ensemble averaged Navier-Stokes equations, as used by Shamroth, Gibeling and McDonald [4] and by Shamroth, McDonald and Briley [5]. The solution of the full Navier-Stokes equations includes all convective, pressure and diffusion terms necessary to model large sparated regions of flow and can be used to solve shear layers not alligned with any of the coordinate directions. The only approximation is associated with the replacement of fluctuating properties due to turbulence by their time-averaged values.

The numerical procedure used by the above to solve these governing equations was a consistently split linearixed block implicit (LBI) scheme orginally developed by Riley and McDonald [6]. In this method the governing equations are replaced by an implicit time difference approximation, optionally a backward difference or Crank-Nicolson scheme. Terms involving non-linearities at the implicit time level are linearized by Taylor's expansion in time about the solution at the known time level, and spatial difference approximations are introduced. This results in a system of multidimensional, coupled, linear difference equations for the dependent variables at the unknown time level. These difference equations are then solved using a Douglas-Gunn [7] procedure for generating alternating-direction implicit (ADI) schemes as perturbations of fundamental difference schemes. The flow equations are replaced by coupled linear difference equations having narrow block-banded matrix structures, which may be solved efficiently by standard block ellimination methods.

A simplification of the full Navier-Stokes solution is one based upon the thin shear layer equations. These equations contain all pressure and convective

terms but retain only those viscous terms significant in thin shear layer flow aligned with one coordinate direction. The remaining viscous terms are omitted from the analysis. Such an approach has been utilized by Steger, Pulliam and Chima [13].

The use of the Navier-Stokes equations to represent transonic flows has one major advantage: The entire flow-field (both boundary-layer and core region) is solved via a single set of equations, avoiding the division of the flow into separate viscous and inviscid regions. This leads to increased accuracy and simplifies the solution procedure. Fully viscous approaches to the modelling of transonic turbomachinery flows have given very good predictions of the flow field. However, such approaches are necessarilly expensive in terms of computer running time and memory requirements and in terms of man-hours needed to develop such a code. At present, the solution of the full Navier-Stokes equations as applied to transonic flows is limited to organisations with access to supercomputers Although it is likely that as computers become more powerful and cheaper such techniques will gain wider acceptance, a simplified solution of transonic flows is needed in the interim period.

1.4 Euler Equation Solution Procedures

One of the most widely used methods, at present, to simulate internal transonic flows is to time march the solution of the transient Euler equations to an asymptotic steady-state. The Euler equations are essentially the Navier-Stokes equations with all viscous terms removed. For inviscid, unsteady, two-dimensional flows through a stationary blade row the Euler equations can be expressed in a Cartesian coordinate system as:

Mass Continuity:

$$\partial\rho/\partial t + \partial(\rho u)/\partial x + \partial(\rho v)/\partial y = 0 \qquad (4)$$

x-momentum continuity:

$$\partial(\rho u)/\partial t + \partial(p+\rho u^2)/\partial x + \partial(\rho uv)/\partial y = 0 \qquad (5)$$

y-momentum continuity:

$$\partial(\rho v)/\partial t + \partial(\rho uv)/\partial x + \partial(p + \rho v^2)/\partial y = 0 \qquad (6)$$

Energy continuity:

$$\partial E/\partial t + \partial(\left[E+p\right]u)/\partial x + \partial(\left[E+p\right]v)/\partial y = 0 \qquad (7)$$

where: $E = p/(\gamma-1) + \rho(u^2+ v^2)/2 \qquad (8)$

Equations (4) to (7) may be written as:

$$\vec{W}_t + \vec{F}_x + \vec{G}_y = 0 \qquad (9)$$

where $\vec{W}$, $\vec{F}$ and $\vec{G}$ are column vectors given by:

$$\vec{W}= \begin{bmatrix} \rho \\ \rho u \\ \rho v \\ E \end{bmatrix} \quad \vec{F}= \begin{bmatrix} \rho u \\ p+\rho u^2 \\ \rho uv \\ (E+p)u \end{bmatrix} \quad \vec{G}= \begin{bmatrix} \rho v \\ \rho uv \\ p+\rho v^2 \\ (E+p)v \end{bmatrix}$$

Thus equation (9) together with the equation of state completely defines the problem.

The Euler equations have been solved both in two-dimensions, Denton [8], and in three-dimensions, Denton [9] and Singh [10]. In the three-dimensional solution, one additional equation of momentum continuity must be added to equations (4) to (8). Other examples of the solution of the Euler equations are the procedures of Couston [11] and of Gopalkrishan and Bozzola [12].

The Euler equations may be solved in either finite-difference, Pulliam [13], or in finite volume form, Schmidt and Jameson [14]. In the former approach the equations are approximated by conventional finite difference relations, relating values of the fluid properties stored at grid nodes. In the finite volume method the equations are regarded as conservation equations applied to a series of interconnected elementary volumes. Both approaches are equivalent on a rectangular Cartesian grid, but for highly distorted grids which must be used for real turbomachines it appears that it is easier to enforce global conservation using the finite volume method.

The solution procedure used in the finite-volume scheme of Denton [8 and 9] is to evaluate the fluxes, for each equation, through all the faces of the elements of the computational grid. This is accomplished using averages of the flow properties at the four corners of the face concerned (for 3-D flow). These flows are summed to find the change of the conservation property for each element, over the time step. One quarter of this change is then added to the values of the properties at the four downstream corners of the element. The manner of distributing this change does not affect the final solution, for which the sum of the fluxes at each element must be zero. It does, however, have a critical influence on the stability of the solution procedure.

Stability is enforced by using an effective pressure in the momentum equations, rather than the true pressure. This effective pressure is made equal to the current pressure at the next downstream grid point plus a correction. The correction at any point is obtained by an interpolation procedure which does not make use of the true pressure at that point. It is also necessary to damp the changes in the pressure correction after each time step, Denton [9] uses a relaxation factor of 0.05. This smoothing is very small and has been shown to have a negligible effect on the final solution.

Inviscid analyses suffer from two major defects. Firstly they are limited by their neglect of viscous displacement effects. In cases where the boundary layer remains thin, as in the flow through accelerating turbine blade rows, flow field predictions neglecting viscous effects may be quite accurate. However, if the boundary-layer thickens appreciably, the actual pressure distribution generated in the flow may be significantly affected by the boundary-layer development. In transonic flows, shock placement is very sensitive to the effective airfoil geometry and even small viscous displacement effects can significantly affect the blade passage pressure distribution. In these cases the interactive effects of the boundary layer with the rest of the flow field can become particularly severe. The other limitation of completely inviscid analyses is their inability to predict aerodynamic losses and heat-transfer rates. Nevertheless, inviscid analyses offer a considerable simplification of the problem and have been applied successfully to a variety of transonic flows.

In most solutions of the transonic flow problem using the inviscid Euler equations it is usual to introduce a correction, which accounts for the viscous phenomena, into the inviscid analysis. The simplest

such approach modifies the inviscid solution via empirical data correlations. This approach is limited, however, to flow conditions within the range of the correlating data and is not widely used nowadays.

A more widely used approach solves the boundary-layer equations, recognising the mutual dependence of the pressure distribution and the viscous effects. The boundary-layer blockage may be readilly incorporated into the inviscid Euler calculations either by displacing the blade surfaces by one boundary layer displacement perpendicular to the surface, or by forcing fluid to transpirate through the blade surfaces. Singh [10] adopted the fomer approach to obtain greatly improved predictions of the flow through a transonic compressor. Although the real boundary-layer flow is likely to be highly three-dimensional, suitable three-dimensional boundary layer prediction methods are not yet available. Singh was able to obtain good results by instead applying a two-dimensional boundary-layer method along the quasi-streamlines.

Denton [8,9], however, preferred a transpiration type boundary-layer displacement model, in which the approach fluid is assumed to flow through the blade surface at a rate sufficient to displace the mainstream by one boundary-layer displacement thickness. The advantage of the transpiration model is that the computational grid does not have to be regenerated everytime the boundary layer is updated. Denton chose to update the boundary-layer prediciton after every fifty time step calculations. A more sphisticated inviscid/viscous interaction was employed by Rizzetta and Borland [15], who modelled the displacement effect of the shock/boundary-layer interaction and utilized this in conjunction with the boundary-layer solution.

The solution of the (transient) Euler equations is usually achieved by marching forwards in time to arrive at the steady-state condition, through the transient behaviour of the flow. This technique provides a solution of the flow equations as a function of time and it is assumed that the asymptotic limit at large times is the desired steady-state solution of the problem. As a disturbance at any time level can only influence events at a later time level the solution is hyperbolic in time. Thus the solution of the steady mixed hyperbolic-elliptic problem, such as that encountered in transonic flow, is achieved by the solution of the transient equations which are hyperbolic in character, regardless of whether the flow is subsonic or supersonic. Such an approach is termed a 'time-marching' procedure. Even though an additional variable, time, is introduced into the computation, this type of technique is very attractive because it allows the use of a single numerical technique for the entire flow domain.

As with all explicit time marching methods the theoretical maximum stable time step is determined by the Courant-Friedrichs-Lewi (CFL) condition, depending on the space and time descretization as well as the mesh size. Denton [8] adheres to the following forms of the CFL conditon:

$$\Delta t < \Delta \ell / (v + c) \qquad (10)$$

where Δt is the maximum stable time step, v is the estimated maximum velocity in the field, $\Delta \ell$ is the minimum dimensional length of each element and c is taken for safety as the inlet stagnation speed of sound.

It is not necessary to take the same physical time-step, for each element or even for each equation, to obtain the correct steady-state solution. As long as the conservation equations are satisfied for every element the

steady-state solution is independent of the magnitude of the time-step Δt. Hence the maximum stable time-step can be chosen for each individual element to obtain the fastest convergence to the steady-state. This spatial variation in time-step results in significant reductions in computer running time. However, the intermediate transient solution then has no physical significance.

The advantage of time marched Euler solutions to internal transonic flows is that they make no assumption of irrotationality. As a result their use can be extended to flows with strong shock waves (Mach number at the shock greater than 1.4). In general, however, even allowing for spatial variations of the time-step, the CFL limitation of the time-step causes slow convergence and several hundreds of time-steps are needed to advance to the steady-state solution. Even if the CFL conditions are satisfied, stability problems may occur caused by a lack of dissipation allowing amplification of non-linear oscillations generated by the shockwaves in the solution. Therefore, all time-marched Euler solutions require an additional damping mechanism such as spatial smoothing [16], explicit artifical damping terms [17], or more ellaborate methods such as Coustons Damping surface technique [11] or Denton's 'Opposed Difference' technique [9]. Alternatively specialized numerical techniques, for example McCormack or Lax-Wendroff schemes, may be used. These schemes split the time step into two parts, elliminating the need for spatial smoothing at the expense of increased computer running time. They do, however, ensure the stability of the integration of the equations through time until a steady-state is achieved, without introducing the errors into the steady-state solution that smoothing does. Smoothing between each time-step has been known to cause significant underestimation of shock-strength and errors in shock location.

1.5 Velocity Potential Methods:-

The appearance of pressure in the Euler equation (5 to 7) complicates their solution, as the determination of pressure is not straightforward. Essentially the difficulty arises because there is no equation for pressure itself. Instead the pressure field must be chosen so that the solutions of the momentum equations, in which the pressure gradient features, yields a velocity field which also satisfies continuity.

The number of independent variables, in the Euler solution, which must be computed and stored means that such a technique is expensive in terms of computer storage. Also, as mentioned previously, the CFL condition causes the time-marched solution of the Euler equations to require large amounts of computer running time. As a result the solution of transonic flows is often computed in terms of a single variable, velocity potential. In order to reduce the system of Euler equations to a single equation, it is necessary to introduce the assumption that the flow is irrotational. The velocity potential, ϕ, may therefore be introduced such that:

$$\vec{V} = \text{grad } \phi \tag{11}$$

Thus the mass continuity equation may be written, for two-dimensional, steady, irrotational flow in a stationary blade row, as:

$$(\rho\phi_x)_x + (\rho\phi_y)_y = 0 \tag{12}$$

where $\phi_x = u$ and $\phi_y = v$ (13)

Combining the continuity equation with the momentum and energy conservation equations leads to a single equation in

velocity potential for isentropic, steady, inviscid two-dimensional flow:

$$(a^2-u^2)\phi_{xx} + (a^2-v^2)\phi_{yy}-2uv\phi_{xy} = 0 \qquad (14)$$

where a is the local speed of sound determined from the energy equation:

$$a^2= a_o{}^2-(\gamma-1)(u^2+v^2)/2 \qquad (15)$$

a_o being the speed of sound based on the stagnation temperature.

Equation (14) can be written with $u^2=\phi_x{}^2$ and $v^2=\phi_y{}^2$, or alterntively in terms of cylindrical coordinates:

$$(a^2-\phi_\theta{}^2/r^2)\phi_{\theta\theta}/r^2+ (a^2-\phi_{zz})\phi_{zz}-2/r^2(\phi_\theta\phi_z) = 0 \qquad (16)$$

Both forms of the equation have been widely used for the solution of transonic flows. Chen [18] and Garabedian and Korm [3] use the velocity potential equation in cartesian coordnates (eqn. 14), whilst McCarthy and Reyhner [19] opt for the cylindrical form (eqn. 16). A more general approach which is capable of solving the full potential equation for flows not aligned with any of the coordinate directions is Jameson's 'rotated' scheme. This is derived by writing the potential equation in the local Cartesian coordinate system orientated along the streamline and its normal. For example, for two-dimensional flows, ignoring the change of streamwise direction in the x-direction:

$$(a^2-q^2)\phi_{ss} + a^2\phi_{nn} = 0 \qquad (17)$$

where: $$\phi_{ss} = \frac{u^2}{q^2}\phi_{xx} + \frac{2uv}{q^2}\phi_{xy} + \frac{v^2}{q^2}\phi_{yy} \qquad (18)$$

$$\text{and} \quad \phi_{nn} = \frac{v^2}{q^2}\,\phi_{xx} - \frac{2uv}{q^2}\,\phi_{xy} + \frac{u^2}{q^2}\,\phi_{yy} \tag{19}$$

This form of the velocity potential equation (eqn.17) has been used by Jameson [20] and by Sobieczky and Dulikravich [21].

In all forms of the velocity potential equation (eqn.(12), (14), (16), or (17) the pressure does not feature, and the governing set of Euler equations has been replaced by a single equation. The resulting savings in computer time and storage are responsible for the widespread use of velocity-potential methods. The use of the velocity-potential does, however, assume that the flow is irrotational and isentropic. These assumptions limit the application of these methods to cases where the shock system is weak (Mach number at the shock less than 1.3). Fortunately most turbomachines operate without strong shocks, to minimize aerodynamic losses, and potential methods can be usefully applied to the vast majority of turbomachines. If however, flows with stronger shocks are required to be solved accurately a more sophisticated approach is needed, such as an Euler or Navier-Stokes solution.

The replacement of the separate equations of mass, momentum and energy conservation into a single velocity-potential equation depends on a flow field that satisfies each starting conservation equation independently. There is no guarantee that every solution to the single flow equation is a solution to all the conservation equations. Indeed, this is not the case when there exists a step or discontinuous change in velocity within the flow domain, such as a shock wave. Murman recognised the effect of such discontinuities and urged the use of a 'conservative' form of the equation.

The equation of mass continuity is often referred to as the 'strong conservation' form of the velocity potential equation:

$$(\rho\phi_x)_x + (\rho\phi_y)_y = 0 \tag{12}$$

This equation may be adapted to flow through a rotating blade row, again in the cartesian coordinate system, thus:

$$(\rho b\phi_x)_x + (\rho b\phi_y)_y = U\nabla(\rho b) \tag{20}$$

where b is a blockage factor taking into account the variation in streamtube thickness in the third (radial) direction. The right-hand side of the equation contains the effect of rotation of the blade row with speed U.

This rotational form of the strong conservation equation has been successfully utilized by Deconick and Hirsch [22]. The form for stationary blade rows (eqn 7) has been used by many researchers including Holst [23] and Deconick [24]. The mass continuity equation may also be written as:

$$\nabla^2\phi = -\nabla\phi.\nabla\ln\rho \tag{21}$$

This form of the strong conservation equation was solved by Ives and Llutermoza [25] but does not otherwise seemed to have been popular.

As mentioned previously, no velocity potential equation is capable of satisfying all the original Euler conservation equations across a shock wave. The strong conservation form, eqns(7, 21 or 22) does conserve mass across a shock but results in a loss in momentum. The alternative, eqn(14, 16 or 17) is derived from a combination of all the original conservation equations. However, across a shock wave it satisfies none of these original equations, predicting a loss in both mass

and momentum. The loss in momentum is, however, generally less than that resulting from the use of the strong conservative form. The best form of the velocity potential equations is the one which best approximates the true non-isentropic jump across the shock. For practical use, axial turbomachines are generally designed to have weak shock systems if any at all, to reduce loss and to avoid boundary-layer separation. A comparison between the two forms of the velocity potential equation has been made by comparing their predictions to one-dimensional flows. For flows with weak shocks, the discrepancies between the two methods was found to be negligible. Thus the choice of equation form appears to be a matter of convenience rather than accuracy: Both forms will violate one or more of the set of fluid dynamic equations across a discontinuity.

There is a school of thought which opts for the strong conservation form of the velocity-potential equation. The logic is that it is more acceptable to suffer some loss of momentum across a shock, which would simply be equivalent to a drag, than it is to suffer a loss of mass. Also it is more easy to introduce a blockage factor, representing the streamtube contraction in the third dimension, into the strong conservation form than into the alternative form. The use of the strong conservation form does have one disadvantage: It has been found to be more likely to predict non-unique solutions [26], in which more than one flow-field may be predicted which satisfies all the boundary conditions.

In all the velocity-potential schemes discussed here, the governing set of equations has been reduced to a single equation in a single unknown, ϕ. This equation is steady and cannot be solved by time-marching. Thus the problem is one of mixed hyperbolic-elliptic nature and the upwind dependence of supersonic flow regions must be modelled if an accurate solution is to be obtained.

Murman and Cole [2] achieved this by using two different finite-difference schemes to approximate derivatives in subsonic and supersonic flow.

The scheme used to represent derivatives in the subsonic flow regime, the central-difference scheme, contained nodes both upstream and downstream of the reference node. The scheme used to represent derivatives in the supersonic flow regime, the upwind difference scheme, contained only nodes situated upstream of the reference node. Thus, although not representing the exact conical shape of the domain of influence of points in supersonic flow, Murman and Cole did introduce a reasonably accurate domain of dependence for all points in the flow and were rewarded with very promising results.

In the more general rotated scheme of Jameson, upwind differences are used for all derivatives appearing in the equation for ϕ_{ss} (eqn 18) when the flow is locally supersonic. Central differencing is used for these terms when the flow is locally subsonic and is used to represent the derivatives in the expression of ϕ_{nn}, regardless of whether the flow is subsonic or supersonic.

Later researchers [27, 28, 29], by examining the exact form of the two different finite difference schemes and the truncation errors associated with each, proved that the upwind difference scheme could be replaced by a central-difference scheme plus some additional terms. These additional terms were called Artificial Viscosity because they contained second order derivatives of velocity. Thus the entire flow field was represented by a central-difference scheme with some additional terms being added to the flow equations representing regions of supersonic flow. The flow equations are, therefore, made effectively elliptic throughout the physical space and a single solution

procedure can be used to solve for all points within the flow-field. In addition to simplifying the solution procedure the inclusion of Artificial Viscosity terms was found to supress the tendency of the potential solution to produce unrealistic solutions containing, for example, expansion shocks. However, some smearing of the jump in flow properties across the shock was also found to result from the inclusion of Artifical Viscosity.

The solution of the steady velocity-potential equation is usually accomplished by relaxation methods. One of the most common forms of these techniques is known as Successive-Line-Over-Relaxation (SLOR). In this method the matrix, $[A]$ containing the coefficients of the flow equations along a single column of nodes is inverted by a Gaussian Ellimination Technique. This matrix is relatively small of size nxn, where n is the number of nodes per column (x=constant). In addition the matrix is sparse and only a few of the coefficients of the matrix need be stored. All references to nodes not in the column under consideration are included as constants on the right hand side of the equation in matrix $[K]$. Thus we can represent the flow equations along any column by:

$$[A]\,[\phi] = [K] \tag{22}$$

where A is the nxn matrix containing the coefficients of the flow equations, $[\phi]$ is a nxl matrix containing the velocity-potentials along the column and $[K]$ is also a nxl matrix containing the constants of the equations. This equation (22) represents a set of n equations relating the values of the velocity potential at the n nodes along the column under consideration. This matrix equation can then be solved using standard matrix procedures and the entire process is repeated for the next column downstream, and so on. A slightly different

technique is the Alternating-Direction-Implicit (ADI) method, which solves the flow equations alternatively along a single row and a single column. With both techniques a number of sweeps of the flow-field is generally needed before a converged solution is obtained, about 100 of these sweeps being the norm.

An alternative to solving the flow equations along a single column (or row) at a time is to solve the entire flow-field by a single matrix inversion. The governing equations of the entire flow-field are represented by a single matrix equation, the solution of which gives the values of the velocity potential at all nodes within the flow-field, concurrently. The matrixes involved are of course large: $[A]$ being of size NPxNP, and $[\phi]$ and $[K]$ being both of size NPx1, where NP is the number of nodes in the entire flow-field. Although the matrix $[A]$ containing the coefficients of the flow equations is again sparse (either tri-or penta-diagonal), such an approach requires considerable extra computer memory compared to a SLOR or ADI scheme. Also, with very large matrixes the accumulative round-off error in the solution procedure, due to computer inaccuracy, may well become significant. For these reasons direct matrix inversion of the entire flow-field is rarely used to solve the difference equations representing transonic-flow.

1.6 Relative Popularity of the Different Methods of Solving for Transonic Flows

There are three major methods of predicting transonic flows. The simplest is by solving for a single equation in velocity potential. This assumes that the flow is irrotational and isentropic and limits the use of such methods to flows in which the shock is weak. Nevertheless, the solution of the velocity-potential

equation is very economical in terms of computer storage and running time and has, to date, been the technique most widely used to simulate transonic flows.

The recent advances in computer power have led to the solution of the time-marched Euler equations gaining in popularity and they are, at present, the method most commonly used to predict transonic flows. The Euler equations are transient and inviscid and conserve mass, momentum in each dimension solved and energy. The flow is solved in terms of the primative variables (u,v,p etc) which introduces a further complexity compared to the velocity potential approach. The Euler equations make no assumption of irrotationality and can be used to solve for flows with strong shock systems. However, they are inviscid and, as with the velocity potential solution, a separate boundary-layer displacement type model must be incorporated if viscous effects are to be included. The solution of the Euler equations require more computer storage and running time than that of the velocity-potential equation but it is still an economical technique compared to the third method for solving transonic flows: the solution of time averaged Navier-Stokes equations.

The Navier-Stokes equations contain all convective, pressure and viscous terms necessary to model transonic flows. However their solution is extremely expensive in terms of computer storage and running time and the use of such techniques is restricted to organizations with access to supercomputers. However, it is likely that as the power of available computers continues to advance, the solution of the full Navier-Stokes equation will gain in popularity, as an accurate method of simulating transonic flows.

2 THE TECHNIQUE USED TO MODEL TRANSONIC FLOW

2.1 The Equation to be Solved

In this report, the strong conservative full velocity-potential equation is used to represent transonic flow. The flow-field is solved in two-dimensions and the flow is assumed to be steady, thus:

$$(\rho b \phi_x)_x + (\rho b \phi_y)_y = 0 \tag{23}$$

This equation applies to flow through a stationary blade row or duct. The equation contains no viscous terms and the use of the velocity-potential assumes that the flow is irrotational and isentropic. The assumption of irrotationality and isentropy limits the solution to flows with weak shock systems. The term b in equation (23) is the blockage factor which takes into account the variation of stream-tube thickness in the third direction due to a change in passage height and casing boundary layer thickness in the axial direction. This blockage factor is not calculated but must instead be specified before the solution is determined. For the solution of the transonic flow in the two-dimensional nozzle considered in this report, the change of streamtube thickness in the third direction is ignored and the value of b at every point is set equal to unity. For the solution of the flow in the two-dimensional transonic cascade blade row also considered in this report, however, a linear variation of b is imposed between the blade leading and trailing edges. Upstream of the leading edge and downstream of the trailing edge the blockage factor is assumed constant.

The density, ρ, in equation (23) is computed from the isentropic relation:

$$\rho = \rho o \left[1 - \frac{(\gamma-1)\,(\phi_x^2 + \phi_y^2)}{2\gamma R\, To} \right] 1/(\gamma-1) \tag{24}$$

The values of the velocities $u=\phi_x$ and $v = \phi_y$ used in the last equation are always taken from the most recently completed iteration. The total density ρo is based on the total temperature and pressure thus:

$$\rho o = \frac{P}{RTo} \tag{25}$$

The governing equation (eqn.23) has no simple analytic solution and must instead be solved numerically. To obtain a numerical solution it is necessary to first define a grid distribution over the flow domain with nodal points at which the flow properties are to be solved. Once the grid has been defined the next step is to replace the partial differentials in the governing equation with algebraic expressions. This will result in a system of algebraic equations which can be solved iteratively to obtain the value of velocity potential, and thence every other flow property, at each node.

2.2 The Computational Grid

2.2.1 The Computational Grid for the solution of the nozzle problem

The computational grid used for the solution of transonic flow in the two-dimensional covergent-divergent nozzle under investigation is very simple to construct. As the nozzle is symmetrical about the axial direction the flow is only solved above the centre-line, which is then treated as a solid wall. Essentially the grid consists of 87 vertical columns (lines along which x = constant) and 13 rows, see Figure 1. The columns are intersected by the rows in such a manner that, along any column, the spacing between any two consecutive rows, Δy, is constant. This spacing between rows will vary from column to column depending on the height of the nozzle upper wall above the centre-line at any particular column.

In order to be able to accurately apply the (Neuman) boundary conditions along the rows corresponding to the nozzle wall and centre-line, two rows of 'dummy' points are included external to the flow-field. One of these rows is situated one Δy spacing below the centre-line and the other is situated one Δy spacing above the upper wall. At each intersection between a row and a column there is situated a single node. This the computational grid comprises 87 column each of 13 nodes or 13 rows each of 87 nodes, giving a total of 1131 nodes. The solution of the flow-field is required in terms of the value of velocity potential, and thence every other fluid property, at each node.

In order to ensure stability of the solution procedure it is desirable for the elements of the grid to have sides of approximately equal length, with no abrupt change in these lengths from one element to its neighbour. In the grid utilized in this report the spacing, Δx, between any column I and the column immediately downstream, I+1, is made equal to the spacing Δy, between two consecutive nodes on column I. Thus in regions where the distance between the nozzle-wall and centre-line is small, for example at the throat, both the nodes and the columns are packed relatively closely together.

2.2.2 The Computational Grid for the solution of the Cascade Problem

The computational grid utilized in this report, in the solution of transonic flow in the two-dimensional cascade blade row is similar to that used to compute the flow in the nozzle; see Figure 2. As the distance between the topmost row of nodes and those at the bottom does not vary much, the spacing between one column and its immediate neighbour may be kept constant throughout the flow-field. Provided then that the number of rows is carefully chosen,

the height of most elements will be approximately equal to their width, as required for stability. The rows of nodes in the flowdomain upstream of the blade passage are straight lines inclined to the x-axis to an angle equal to the known inlet air-flow angle. Similarly, the rows downstream of the blade passage are straight lines inclined at an angle, equal to the set outlet air-flow angle, to the x-axis. Along all columns in the flow domain the rows are equally spaced and, as before, two additional rows of 'dummy' nodes are included.

Thus, the computational grid used in the computation of flow through the cascade blade row consists of fifty-seven columns, each containing nineteen nodes, giving a total of 1086 nodes. Twenty of these columns are situated upstream of the blade passage, a further twenty downstream of the blade passage and the remaining seventeen inside the blade passage. The position of the columns have been chosen so that no node coincides with either the leading or the trailing edge of the blade. It was felt that if a node coincided with either of these points the solution procedure would become complicated. That point would then be required to satisfy two boundary-conditions: one typical of points on the blade surface and the other typical of points on the periodic boundary. Instead the first column inside the blade passage is situated half a column spacing downstream of the leading edge and the last column within the blade passage is situated a similar distance upstream of the trailing edge.

2.3 The Finite Difference Approximation

The partial derivatives of velocity potential appearing in the governing flow equations are approximated, in this report, using finite difference approximations. Finite-difference techniques are, in general, well understood and maintain a direct connection with the mathematical

form of the governing equation. Precise mathematical conditions of existence and convergence exist for these techniques, as well as methods for error analysis. In addition, an 'upwind' finite-difference scheme may be readily incorporated to mirror the domain of dependence of supersonic flows, and powerful iterative methods have been developed for the solution of the resulting algebraic equations.

2.3.1 Taylor's Theorem

The finite-difference approximation used in this report is based on the Taylor's expansion in two independent variables, which relates the value of the velocity potential at any node n, to that at a reference node o by the following:

$$\phi_n = \phi_o + \phi_x (X_n - X_o) + \phi_y (Y_n - Y_o) + \phi_{xy} (X_n - X_o)(Y_n - Y_o)$$
$$+ \tfrac{1}{2}\phi_{xx} (X_n - X_o)^2 + \tfrac{1}{2}\phi_{yy} (Y_n - Y_o)^2 + \tfrac{1}{6}\phi_{xxx} (X_n - X_o)^3$$
$$+ \tfrac{1}{2}\phi_{xxy} (X_n - X_o)^2 (Y_n - Y_o) + \tfrac{1}{2}\phi_{xyy} (X_n - X_o)(Y_n - Y_o)^2$$
$$+ \tfrac{1}{6}\phi_{yyy} (Y_n - Y_o)^3 + \text{H.O.T.} \qquad (26)$$

where ϕ_n is the value of velocity potential at node n, situated at $X=X_n$, $y=y_n$; ϕ_o is the value of velocity potential at node o, situated at $X=X_o$, $y=y_o$; ϕ_x is the partial derivative $\partial\phi/\partial_x$, $\phi_{xy}=\partial^2\phi/\partial_x\partial_y$ etc; and H.O.T. which contains fourth order and higher partial derivatives of velocity potential is the error of the approximation.

From equation (26) it can be seen that, for third order accuracy, nine partial derivatives of velocity potential must be taken into account when approxmating any partial derivative of velocity potential by a function of the velocity potential at surrounding nodes.

2.3.2 Central-Difference Approximation

The central-differenced form of the finite-difference approximation is used to represent partial derivaties of velocity potential at regions in which the flow is locally subsonic. When approximating a particular derivative at any node using a central-differenced approximation, a lattice of nine nodes (in addition to the reference node) must be used, one for each derivative which must be considered. Equation (26) may then be applied to each of these nine nodes to give nine equations. It is required that each of these nine equations are multiplied throughout by a constant (say C_n, where $n = 1$ to 9). The nine constants, C_1 to C_9 are of value such that when the nine equations, each having previously been multiplied by the relevant constant, are summed together the coefficient of the particular partial derivative to be approximated is equal to unity. In addition, it is required that the coefficients of all the other eight partial derivatives be zero. Thus we have nine conditions from which the values of the constants C_1 to C_9 may be uniquely determined. For every partial derivative to which an approximation is required, a different set of coefficients must be determined. In the solution procedure used to simulate transonic flows in this report, approximations are required only of the first and second order partial derivatives of velocity potential.

The nine conditions from which the values of the particular set of coefficients required may be determined, can be written, in general, as:

$$\sum_{n=1}^{n=9} \left[C_n \, (X_n - X_o) \right] = a$$

$$\sum_{n=1}^{n=9} \left[C_n \, (Y_n - Y_o) \right] = b$$

$$\sum_{n=1}^{n=9} \left[C_n \, (X_n - X_o)^2 \right] = c$$

$$\sum_{n=1}^{n=9} \left[C_n \, (X_n - X_o)(Y_n - Y_o) \right] = d$$

$$\sum_{n=1}^{n=9} \left[C_n \, (Y_n - Y_o)^2 \right] = e \qquad (27)$$

$$\sum_{n=1}^{n=9} \left[C_n \, (X_n - X_o)^3 \right] = 0$$

$$\sum_{n=1}^{n=9} \left[C_n \, (X_n - X_o)^2 (Y_n - Y_o) \right] = 0$$

$$\sum_{n=1}^{n=9} \left[C_n \, (X_n - X_o) \, (Y_n - Y_o)^2 \right] = 0$$

$$\sum_{n=1}^{n=9} \left[C_n \, (Y_n - Y_o)^3 \right] = 0$$

The values of a,b,c,d and e depend on the particular derivative which is to be approximated, and are set in accordance with the table below:

Derivative	a	b	c	d	e
$\partial\phi/\partial x$	1	0	0	0	0
$\partial\phi/\partial y$	0	1	0	0	0
$\partial^2\phi/\partial x^2$	0	0	2	0	0
$\partial^2\phi/\partial x\partial y$	0	0	0	2	0
$\partial^2\phi/\partial y^2$	0	0	0	0	1

Table 1

For each node in the computational field, therefore, there is required five sets, each of nine coefficients, which enables all first and second order partial derivatives of velocity-potential to be approximated by central-differences. The partial derivative of velocity potential at any point O, can then be express as:

$$P.D.= \sum_{n=1}^{n=9} C_n\phi_n - \phi_o \sum_{n=1}^{n=9} C_n \qquad (28)$$

where P.D. is any first or second order partial derivative of velocity potential in x or y. C_n is the set of nine coefficients, for the particular node and derivative under consideration calculated from equation (27).

The above equation is third order accurate.

2.3.3. The Central-Difference Lattice

The partial derivatives of velocity-potential, at any particular node, may be represented by equation (28) as a function of the values of velocity-potential at nine points in the neighbourhood of that node. In theory at least, these nine nodes may be any nine nodes in the flow domain. However, the error of the finite-difference approximation is roughly proportional to the sum of the fourth powers of the spacings of each of these nine nodes from the node under consideration. To minimize this error the nine nodes chosen are in close proximity to the node under consideration. It has also been found that, for third order accuracy, it is desirable to have three of these nodes on the same column as the node under consideration, and a further three on the same row. Thus for the central-differenced approximation to any partial derivative of velocity potential at a general node on column I and row J, the form of the finite-difference lattice employed is as Figures [3] and [4].

2.3.4 The Upwind Difference Approximation

The finite-difference lattice, used for the central-differenced approximation of partial derivatives of velocity-potential, contains nodes both upwind and downwind of the nodes at which the derivative is being approximated. Thus the fluid properties at that node are influenced by the fluid properties at nodes all around and is representative of the behaviour of flow in a regime of subsonic flow. In supersonic flow, however, the fluid properties, at any node, are only influenced by the fluid properties at upstream nodes. To mirror this effect partial-derivatives of velocity-potential, at any node in a region of supersonic flow, are approximated as a function of the velocity-potential only of upstream nodes. This form of finite-difference approximation is known as a 'back-wind' or 'upwind' finite-difference scheme.

The lattice used in the upwind-difference scheme is similar to that used in the central-difference scheme but without all nodes downstream of the reference node Figs. 5 and 6 . Thus six nodes, in addition to the reference node, are used in the upwind-differenced lattice and equation (26) can be applied to each of these nodes to generate a set of six equations. It is now required that a set of six constants (say D_n, where n=1 to 6) be determined such that when the six equations are multiplied by the relevant constants and then all summed together the coefficient of the desired derivative is unity. A further five conditions are required to uniquely determine the values of the constants D_1 to D_6. The values of the constants D_n have been chosen so that they satisfy the following six conditions:

$$\sum_{n=1}^{n=6} \left[D_n \, (X_n - X_o) \right] = a$$

$$\sum_{n=1}^{n=6} \left[D_n \, (Y_n - Y_o) \right] = b$$

$$\sum_{n=1}^{n=6} \left[D_n \, (X_n - X_o)^2 \right] = c$$

$$\sum_{n=1}^{n=6} \left[D_n \, (X_n - X_o)(Y_n - Y_o) \right] = d \qquad (28)$$

$$\sum_{n=1}^{n=6} \left[D_n \, (Y_n - Y_o)^2 \right] = e$$

$$\sum_{n=1}^{n=6} \left[D_n \, (X_n - X_o)^2 (Y_n - Y_o) \right] = 0$$

where a,b,c,d and e depend on the derivative to be approximated, as given in Table 1. For each node in the computational field, therefore, five sets each of six coefficients are required to approximate the first and second order partial-derivatives of velocity potential using an upwind differenced scheme. The partial derivative of velocity-potential at any point, o, can then be approximated using the upwind-difference scheme by the following expression:

$$P.D.= \sum_{n=1}^{n=6} D_n\phi_n - \phi_o \sum_{n=1}^{n=6} D_n \qquad (29)$$

where P.D. is the partial-derivative of velocity potential in x and/or y, and D_n is the set of six coefficients, whose values will vary depending on which derivative is being approxmiated at which node.

2.4 Artifical Viscosity

The finite-difference lattice used to approximate partial-derivatives in the subsonic flow regime, contains nodes both upstream and downstream of the node at which the derivative is being approximated. The lattice used to approximate partial derivatives in the supersonic flow regime, however, contains only nodes upstream of the node at which the derivative is being approximated. The use of such a mixed-finite-difference scheme ensures that the domain of dependence actually experienced physically by the fluid at any point in the flow-field is modelled by the numerical scheme, whether the flow at that point is subsonic or supersonic.

By examining the form of the two types of finite-difference approximations and the truncation errors associated with each, it can be shown that the upwind-differenced

approximation is identical to the central-differenced approximation plus some additional terms. These additional terms are usually referred to as Artificial Viscosity because they contain second order derivatives of velocity. The exact nature of these Aritifical Viscosity terms will now be considered in detail.

2.4.1 The Rotated Scheme of Jameson

The treatment of flows which are not well aligned with the coordinate system requires the use of a difference scheme in which the upwind bias conforms to the local flow direction. To illustrate the construction of such a scheme consider the 'non-conservative' potential flow equation in Cartesian coordinates:

$$(a^2 - u^2)\phi_{xx} - 2uv\phi_{xy} + (a^2 - v^2)\phi_{yy} = 0 \qquad (2)$$

The required rotation of the upwind differencing at any particular point can be acomplished by introducing an auxiliary Cartesian coordinate system which is locally aligned with the flow at that point, as suggested by Jameson [20]. If s and n denote the local streamwise and normal directions, then equation (2) may be expressed as:

$$(a^2 - q^2)\ \phi_{ss} + a^2\phi_{nn} = 0 \qquad (30)$$

Since u/q and v/q are the local direction cosines, ϕ_{ss} and ϕ_{nn} can be expressed in the original coordinate system neglecting the variation of streamline direction in the x-direction, as:

$$\phi_{ss} = (u^2\phi_{xx} + 2uv\phi_{xy} + v^2\phi_{yy})/q^2 \qquad (31)$$

and

$$\phi_{nn} = (v^2\phi_{xx} - 2uv\phi_{xy} + u^2\phi_{yy})/q^2 \qquad (32)$$

The required rotation of the upwind differencing can then be achieved by using upwind-differenced approximations for the evaluation of the second order derivatives contributing to ϕ_{ss}, when the flow is locally supersonic. If the flow is locally subsonic, however, central-differenced formulae are used to evaluate these derivatives. The second order derivatives contributing to ϕ_{nn} are always approximated using central-differenced formula, regardless of whether the flow is subsonic or supersonic. Assuming that the computational grid is rectangular with constant spacings in the x- and y- directions, the application of the Taylors theorem, in one or two independent variables as appropriate, allows the following relationships to be derived:

$$\phi_{i-1,j} = \phi_{i,j} - \phi_x \Delta x + \tfrac{1}{2} \phi_{xx}\Delta x^2 - \tfrac{1}{6}\phi_{xxx}\Delta x^3 + \text{H.O.T.} \quad (33)$$

$$\phi_{i-2,j} = \phi_{i,j} - 2\phi_x\Delta x + 2\phi_{xx}\Delta x^2 - \tfrac{4}{3}\phi_{xxx}\Delta x^3 + \text{H.O.T.} \quad (34)$$

$$\phi_{i,j-1} = \phi_{i,j} - \phi_y \Delta y + \tfrac{1}{2}\phi_{yy}\Delta y - \tfrac{1}{6}\phi_{yyy}\Delta y^3 + \text{H.O.T.} \quad (35)$$

$$\phi_{i,j-2} = \phi_{i,j} - 2\phi_y\Delta y + 2\phi_{yy}\Delta y^2 - \tfrac{4}{3}\phi_{yyy}\Delta y^3 + \text{H.O.T.} \quad (36)$$

$$\begin{aligned}\phi_{i-1,j-1} = \phi_{i,j} &- \phi_x\Delta x - \phi_y\Delta y + \tfrac{1}{2}\phi_{xx}\Delta x^2 + \tfrac{1}{2}\phi_{yy}\Delta y^2 \\ &+ \phi_{xy}\Delta x\Delta y - \tfrac{1}{6}\phi_{xxx}\Delta x^3 - \tfrac{1}{6}\phi_{yyy}\Delta y^3 - \tfrac{1}{2}\phi_{xxy}\Delta x^2\Delta y \\ &- \tfrac{1}{2}\phi_{xyy}\Delta x\Delta y \end{aligned} \quad (37)$$

where H.O.T. incorporates fourth or higher, order terms.

The above expressions relate the velocity potential at all nodes, on a five-node upwind lattice applied to a square computational grid (fig.7), to the velocity potential $\phi_{i,j}$ at the reference node. From these expressions the following

upwind-differenced approximations can be derived:

equation (34) - 2 x equation (33):-

$$\phi_{xx} = \frac{\phi_{i,j} - 2\phi_{i-1,j} + \phi_{i-2,j}}{\Delta_x^2} + (\phi_{xxx}\Delta x) \qquad (38)$$

equation (37) - equation (33) - equation (35) :-

$$\phi_{xy} = \frac{\phi_{i,j} - \phi_{i-1,j} - \phi_{i,j-1} + \phi_{i-1,j-1}}{\Delta X \Delta Y}$$

$$+ (\tfrac{1}{2}\phi_{xxy}\Delta x + \tfrac{1}{2}\phi_{xyy}\Delta y) \qquad (39)$$

equation (36) - 2 x equation (35) :-

$$\phi_{yy} = \frac{\phi_{i,j} - 2\phi_{i,j-1} + \phi_{i,j-2}}{\Delta y^2} + (\phi_{yyy}\Delta y) \qquad (40)$$

where the terms in the brackets are the errors resulting from approximating the second order derivatives by the first part of the right-hand side of the equation only, ignoring fourth and higher, order terms. Thus the upwind-differenced formulae in equations (38) to (40) can be regarded as representations of $\phi_{xx} - \Delta x\phi_{xxx}$, $\phi_{xy} - (\frac{\Delta x}{2})\phi_{xxy} - (\frac{\Delta y}{2})\phi_{xyy}$ and $\phi_{yy} - \Delta y\phi_{yyy}$ respectively. The use of the following upwind-differenced approximations:

$$\phi_{xx} \simeq \frac{\phi_{i,j} - 2\phi_{i-j,j} + \phi_{i-2,j}}{\Delta x^2}$$

$$\phi_{xy} \simeq \frac{\phi_{i,j} - \phi_{i-1,j} - \phi_{i,j-1} + \phi_{i-1,j-1}}{\Delta x \Delta y} \qquad (41)$$

$$\phi_{yy} \simeq \frac{\phi_{i,j} - 2\phi_{i,j-1} + \phi_{i,j-2}}{\Delta y^2}$$

in the representation of ϕ_{ss} from equation (31), therefore, introduces the following additional terms into the representation of the potential equation (2):

$$A.V. = (1 - \frac{a^2}{q^2}) \{\Delta x(u^2 u_{xx} + uv\, v_{xx}) + \Delta y(uvu_{yy} + v^2 v_{yy})\} \quad (42)$$

where A.V. represents the additional terms referred to as artificial viscosity.

Often instead of solving for the non-conservative form of the potential equation the following 'fully conservative' potential equation is utilized

$$(\rho\phi_x)_x + (\rho\phi_y)_y = 0 \quad (12)$$

It can be shown that this fully conservative form of the potential equation is equivalent to the non conservative form (equation 2) multiplied by the term (ρ/a^2). Thus, if the conservative form of the potential equation is represented by upwind-differenced approximations, the artificial viscosity terms introduced will contain the terms of equation (42) multiplied by (ρ/a^2). In the construction of a discrete approximation to the conservative form (12) of the potential-flow equation, it has proved convenient to accomplish the switch to upwind differencing by the explicit addition of an artificial viscosity to the central-differenced formulae. Thus the equation to be solved is of the form:

$$S_{ij} + T_{ij} = 0 \quad (43)$$

where S_{ij} is a central-difference approximation to the left hand side of equation (12), and T_{ij} is the artificial viscosity which may be constructed as an expression in divergence form:

$$A.V. = \partial P/\partial x + \partial Q/\partial y \quad (44)$$

where P and Q are appropriate expressions.

Thus using the 'rotated' scheme of Jameson, it is required that the expressions P and Q be such that the sum of their partial derivatives, with respect to x and y respectively, equals the right-hand side of equation (42); i.e.:

$$\frac{\partial P}{\partial x} + \frac{\partial Q}{\partial y} = \left(\frac{\rho}{a^2}\right)\left(1-\frac{a^2}{q^2}\right)\{\Delta x\,(u^2u_{xx}+uvv_{xx})+\Delta y\,(uvu_{yy}+v^2v_{yy})\} \qquad (45)$$

Jameson adopted a scheme where P and Q are defined as:

$$P = -\mu\{|u|\Delta y\rho_x\} \qquad (46)$$

$$Q = -\mu\{|v|\Delta y\rho_y\} \qquad (47)$$

where μ is a switching function which is equal to zero in the subsonic zone:

$$\mu = \max\{0,\ 1-a^2/q^2\} \qquad (48)$$

P then approximates:

$$P = -\Delta x\left(1-\frac{a^2}{q^2}\right)u\rho_x = \Delta x\left(\frac{\rho}{a^2}\right)\left(1-\frac{a^2}{q^2}\right)(u^2u_x+uvv_x) \qquad (49)$$

and Q approximates:

$$Q = -\Delta y\left(1-\frac{a^2}{q^2}\right)v\rho_y = \Delta y\left(\frac{\rho}{a^2}\right)\left(1-\frac{a^2}{q^2}\right)(uvu_y+v^2v_y) \qquad (50)$$

When the above formula for P and Q are used it can be verified that the terms containing the highest derivatives of ϕ are the same as those in equation (45).

2.4.2 Application of the Rotated Scheme of Jameson to a Non-square Computational Grid

The derivation of the expression for artificial viscosity, equation (42), is based on a square computational grid. The computation grid described in section 2.2 is not square and, without the benefit of a coordinate transformation, the simple expressions of equations (33) to (37) cannot be utilized. Instead we must, in general, apply the Taylors expansion in two variables for all nodes in the 'upwind' lattice. For each of the six nodes in the upwinded-differences lattice we can express the relationship between the velocity-potential at that node, ϕ_n, and that at the reference node, ϕ_o. i.e.:

$$\phi_n = \phi_o + \phi_x (X_n - X_o) + \phi_y (Y_n - Y_o) + \phi_{xy} (X_n - X_o)(Y_n - Y_o)$$
$$+ \tfrac{1}{2}\phi_{xx} (X_n - X_o)^2 + \tfrac{1}{2}\phi_{yy} (Y_n - Y_o)^2 + \tfrac{1}{6}\phi_{xxx} (X_n - X_o)^3$$
$$+ \tfrac{1}{2}\phi_{xxy} (X_n - X_o)^2 (Y_n - Y_o) + \tfrac{1}{2}\phi_{xyy} (X_n - X_o)(Y_n - Y_o)^2$$
$$+ \tfrac{1}{6}\phi_{yyy} (Y_n - Y_o)^3 + \text{H.O.T.} \qquad (26)$$

As the lattice used in the upwind-difference scheme references only six nodes, other than the reference nodes, the set of coefficients Dn (where n=1to 6) for each derivative at each node can only be chosen so that they satisfy six conditions. These six conditions are as in equations (28). No conditions have been imposed on the resultant coefficients of ϕ_{xxx}, ϕ_{xyy} and ϕ_{yyy} and these will, in general, be non-zero; ie:

$$\sum_{n=1}^{n=6} \left[D_n (X_n - X_o)^3 \right] \neq 0$$

$$\sum_{n=1}^{n=6} \left[D_n (X_n - X_o)(Y_n - Y_o)^2 \right] \neq 0 \qquad (51)$$

$$\sum_{n=1}^{n=6} \left[D_n (Y_n - Y_o)^3 \right] \neq 0$$

The approximation of a derivative by an 'upwind' difference will, therefore be equivalent to the approximation of that derivative by a 'central' difference, plus some additional terms containing third-order derivatives of velocity potential. Thus:

$$(\phi_{xx})_{upwind} = (\phi_{xx})_{C.D.} + \tfrac{1}{6} \sum_{n=1}^{n=6} \left[D_n (X_n - X_o)^3 \right] \phi_{xxx} + \tfrac{1}{6} \sum_{n=1}^{n=6} \left[D_n (Y_n - Y_o)^3 \right] \phi_{yyy} + \tfrac{1}{2} \sum_{n=1}^{n=6} \left[D_n (X_n - X_o)(Y_n - Y_o)^2 \right] \phi_{xyy} \qquad (52)$$

$$(\phi_{xy})_{upwind} = (\phi_{xy})_{C.D.} + \tfrac{1}{6} \sum_{n=1}^{n=6} \left[E_n (X_n - X_o)^3 \right] \phi_{xxx} + \tfrac{1}{6} \sum_{n=1}^{n=6} \left[E_n (Y_n - Y_o)^3 \right] \phi_{yyy} + \tfrac{1}{2} \sum_{n=1}^{n=6} \left[E_n (X_n - X_o)(Y_n - Y_o)^2 \right] \phi_{xyy} \qquad (53)$$

$$(\phi_{yy})_{upwind} = (\phi_{yy})_{C.D.} + \tfrac{1}{6}\sum_{n=1}^{n=6}\left[F_n(X_n-X_o)^3\right]\phi_{xxx} + \tfrac{1}{6}\sum_{n=1}^{n=6}\left[F_n(Y_n-Y_o)^3\right]\phi_{yyy} + \tfrac{1}{2}\sum_{n=1}^{n=6}\left[F_n(X_n-X_o)(Y_n-Y_o)^2\right]\phi_{xyy} \quad (54)$$

By substituting the above expressions into equation (31) and thence into equation (30) it can be shown that the use of 'upwind' differences in the rotated coordinate scheme introduces an effective artificial viscosity (multiplied by ρ/a^2)of :

$$\begin{aligned}A.V. = {} & (a^2/q^2-1)(\rho/a^2)\{ (\tfrac{u^2}{6}\Sigma\left[D_n(X_n-X_o)^3\right] + \tfrac{uv}{3}\Sigma\left[E_n(X_n-X_o)^3\right] \\ & + \tfrac{v^2}{6}\Sigma\left[F_n(X_n-X_o)^3\right]) \phi_{xxx} \} \\ & + (a^2/q^2-1)(\rho/a^2)\{ (\tfrac{u^2}{2}\Sigma\left[D_n(X_n-X_o)(Y_n-Y_o)^2\right] + uv\Sigma\left[E_n(X_n-X_o)\right. \\ & \left.(Y_n-Y_o)^2\right] + \tfrac{v^2}{2}\Sigma\left[F_n(X_n-X_o)(Y_n-Y_o)^2\right]) \phi_{xyy} \} \\ & + (a^2/q^2-1)(\rho/a^2)\{ \tfrac{u^2}{6}\Sigma\left[D_n(Y_n-Y_o)^3\right] + \tfrac{uv}{3}\Sigma\left[E_n(Y_n-Y_o)^3\right] \\ & + \tfrac{v^2}{6}\Sigma\left[F_n(Y_n-Y_o)^3\right]) \phi_{yyy} \end{aligned} \quad (55)$$

$$\text{i.e.:} \quad A.V. = A\phi_{xxx} + B\phi_{xyy} + C\phi_{yyy} \quad (56)$$

where:

$$A = (a^2/q^2-1)(\rho/a^2)\left(\frac{u^2}{6}\left[D_n(X_n-X_o)^3\right] + \frac{uv}{3}\Sigma\left[E_n(X_n-X_o)^3\right] + \frac{v^2}{6}\Sigma\left[F_n(X_n-X_o)^3\right]\right) \quad (57)$$

$$B = (a^2/q^2-1)(\rho/a^2)\left(\frac{u^2}{2}\Sigma\left[D_n(X_n-X_o)(Y_n-Y_o)^2\right] + uv\,\Sigma\left[E_n(X_n-X_o)(Y_n-Y_o)^2\right] + \frac{v^2}{2}\Sigma\left[F_n(X_n-X_o)(Y_n-Y_o)^2\right]\right) \quad (58)$$

$$C = (a^2/q^2-1)(\rho/a^2)\left(\frac{u^2}{6}\Sigma\left[D_n(Y_n-Y_o)^3\right] + \frac{uv}{3}\Sigma\left[E_n(Y_n-Y_o)^3\right] + \frac{v^2}{6}\Sigma\left[F_n(Y_n-Y_o)^3\right]\right) \quad (59)$$

where D_n, E_n and F_n (n=1 to 6) are the sets of coefficients corresponding to the upwind approximations to partial derivatives ϕ_{xxx}, ϕ_{xyy} and ϕ_{yyy} respectively, and all the summations are from i=1 to i=6.

So, it has been shown that an upwind difference is equivalent to a central difference plus a certain additional term (A.V.). Thus it is argued that in supersonic flow, the 'upwind' representation of the flow equations can be replaced by the 'centred' representation plus an artificial viscosity This artificial viscosity is included explicitly into the flow equation, where required. In a regime of supersonic flow, therefore, we may replace the following representation of the 'conservative' potential equation:

$$\{(\rho b\,\phi_x)_x + (\rho b\phi_y)_y\}_{\text{upwind}} = 0 \quad (60)$$

by the centred-difference form with artificial viscosity:

$$\{(\rho b\,\phi_x)_x + (\rho b\phi_y)_y\}_{C.D.} + A.V. = 0$$

or

$$\{(\rho b\, \phi_x)_x + (\rho b \phi_y)_y\}_{C.D.} = - A.V. \qquad (61)$$

The above equation (61) may be applied to any region of the flow-field if the artificial viscosity term becomes zero in all regions of subsonic flow. The switched 'upwind/centre'-difference scheme of Murman and Cole [2] has, therefore, been replaced by a single finite-difference representation which greatly simplifies the solution procedure. Note, that for the artificial viscosity to vanish in all regions of subsonic flow the term (a^2/q^2-1) in equations (57) to (59) must be replaced by the term μ where:

$$\mu = \max \{1,\ 1 - a^2/q^2\}$$

and equation (61) becomes

$$\{(\rho b\, \phi_x)_x + (\rho b\, \phi_y)_y\}_{C.D.} = A.V. \qquad (62)$$

The artificial viscosity has not, in contradiction to the recomendation of Jameson, been formulated in a divergent form as the expression for artificial viscosity derived from a non-square computational grid was too complex. In order to add explicitly the artificial viscosity to the governing flow equation the third-order partial derivatives of velocity-potential need to be approximated. This is achieved by fitting a cubic approximation to the values of the second order derivatives which can then be differentiated analytically to yield the third-order derivatives.

The inclusion of artificial viscosity into the central-differenced approximation of the flow equation is necessary to model the domain of dependence of supersonic flows. If centred-differences are used to represent derivatives in supersonic flow without this artificial viscosity, the solution becomes unstable. The artificial

viscosity does, however, introduce an error into the final solution, resulting in smeared shocks. As the artificial viscosity is dependent on the third power of the mesh spacing, it reduces as the mesh spacing is reduced. In the limit of infinitely small mesh spacing the artificial viscosity becomes zero everywhere.

2.5 Boundary Conditions

2.5.1 Boundary Conditions for the Nozzle Calculation

The computational domain for the solution of the potential flow, in the convergent-divergent nozzle examined in this report, consists of the region of the nozzle, from inlet to outlet, between the centre-line and the upper wall. Due to the symmetry of the nozzle in the flow-direction the flow need only be solved in one half of the nozzle and the centre-line may be treated as if it were a solid wall. For elliptic quasilinear equations it is required that a boundary condition be applied to give an expression for the velocity potential at each node on the perimeter of the computational domain. For the solution of potential flow in a duct or nozzle the boundary conditions are well known. These are that the velocity of the fluid normal to the solid walls is zero.

i.e. $$\frac{\partial \phi}{\partial n} = 0 \qquad (63)$$

The physical significance of this boundary condition is that no fluid is allowed to flow through the solid walls. Such a boundary condition is used in preference to the no-slip condition which specifies that the velocity of the fluid tangential to the solid wall must equal zero.

i.e. $$\frac{\partial \phi}{\partial s} = 0 \qquad (64)$$

The no-slip condition describes the manner in which fluid actually behaves in practice but is dependent on the flow being viscous, as are all real flows. However, the potential formulation assumes that the flow is completely inviscid and cannot, therefore, satisfy the no slip condition. Instead the no through-flow condition must be applied.

Along the inlet plane of the nozzle, the total pressure and temperature are given. Also, the inlet flow angle, which in this case is zero is given. Thus the values of velocity-potential at all nodes on the inlet plane are set. The actual values to which they are set is not significant provided the nodes are all of the same potential, as required for a zero inlet angle. This is because the flow-field is dependent on the gradients of velocity potential and not on the actual values of potential themselves. The set values of velocity potential at all nodes on the inlet plane remain fixed as the solution progresses.

At the exit plane of the nozzle the back-pressure is given. The boundary condition which must be satisfied at this plane is that the static pressure of the fluid equals the nozzle exhaust (back) pressure. It is not possible to express this condition as a linear expression in velocity-potential and instead the values of the potential at the exit plane must be guessed. The solution is then iterated with the guessed values of potential at exit remaining invariant until convergence is achieved. The static pressure of the fluid at exit is then computed from the resulting calculated potential distribution and compared to the back pressure. If the static pressure at exit equals the back pressure the solution is complete, else the values of potential at exit are modified and the solution procedure repeated until equality is achieved.

The modification to the set values of potential at exit is accomplished by adding a constant value of potential to all nodes on the exit plane. This value of additional potential was assumed to be directly proportional to the percentage error of the predicted exit static pressure. So as not to introduce a sharp rise (or a fall) in potential between the nodes on the penultimate column and those along the exit column, the potential along nodes upstream of the exit column are also modified. A lineaily increasing change in potential was introduced to all nodes, from the shock to the exit so that, at the exit, the correct change in potential was introduced. The solution of the potential equation is then complete and from the computed potential distribution the velocity at every node may be calculated. The values of all the other primative variables (e.g. - ρ, p, t) may be calculated from these velocities using the standard isentropic relationships.

2.5.2 Boundary Conditions for the Cascade Solution

The computational domain used for the solution of the potential flow in the cascade problem consists of one passage of a blade row with the inlet and outlet boundaries a sufficient distance upstream and downstream of the blades to allow uniform flow conditions. This domain is a blade-to-blade surface of a cascade blade-row, Figure 8 delimited by ABCDEFGH, X is the coordinate in the axial direction and y the one in the tangential or pitchwise direction. For this system to be well posed the boundary conditions must be specified in a manner compatible with the governing flow equations and the physics of the problem.

Along the solid blade walls the condition that the normal velocity must equal zero is given again imposed:

$$\frac{\partial \phi}{\partial n} = 0 \tag{63}$$

If the effects of rotation are to be included then this derivative must be required to equal some function of the bladespeed [22]. Also, as will be discussed later, viscous effects can be included into the inviscid analysis by a modification of this boundary condition.

At the inlet of the flow domain we have the following boundary condition:

$$\frac{\rho b \partial \phi}{\partial n} = \rho_1 b_1 W_{x_1} \tag{65}$$

At outlet of the flow domain a similar condition applies:

$$\rho b \frac{\partial \phi}{\partial n} = \rho_2 b_2 W_{x_2} \tag{66}$$

where subscripts 1 and 2 denote the inlet and exit boundaries respectively, n is the direction normal to the boundary, and W_x and W_y are velocities in the x- and y- directions.

A particularity in cascade flows is the presence of periodic boundaries upstream (AB,HG) and downstream (CD,FE) of the blade row. As a blade row consists of a number of blades equally spaced, the properties of a fluid at any point are equal to those one pitch spacing away. Thus the primitive variables along AB must be equal to those along HG, and the primitive variables along CD must equal theose along FE. This results in a constant difference in potential between two corresponding points such as P and Q in Figure [8]:

$$\phi_Q = \phi_P + S_1 W_{y_1} \tag{67}$$

where P is any node on the surface AB and Q is the node, of the same valueox as P, on the surface HG.

Similarly downstream of the blade:

$$\phi_{Q'} = \phi_{P'} + S_2 W_{y_2} \tag{68}$$

where S is the pitch spacing.

From equations (65), (66), (67) and (68) together with the mass conservation the following expression can be derived:

$$\rho_1 \, b_1 \, W_{x_1} = \rho_2 \, b_2 \, W_{x_2} \tag{69}$$

As density, ρ, is a function of the x and y velocities, and the blockage factor, b, is a constant which must be specified equation (69) is of the form:

$$\text{Function } (W_{x_1}, W_{y_1}) = \text{Function } (W_{x_2}, W_{y_2}) \tag{70}$$

from which it is clear that only three independent quantities can be specified for both upstream and downstream boundaries including periodicity. Hence inlet Mach number and angle

(which specifies W_{x_1} and W_{y_1}) together with outlet Mach number or alternatively outlet angle completely determine the flow for a given geometrical configuration and blockage. In this report, the Kutta condition has been applied at the trailing edge which specifies that the fluid properties along the suction surface and the pressure surface must approach equality at the trailing edge. The use of the Kutta condition determines the outlet flow angle and no downstream condition need be specified.

The values of velocity-potential along the inlet plane, AH, are set so that the gradient of potential along this plane is constant and equal to the Y-component of velocity corresponding to the known inlet Mach number and angle. These values of velocity potential along the inlet plane are kept invariant as the solution progresses. At the exit plane, DE, the values of velocity potential are also set. Firstly, a value of exit flow angle is guessed, which together with the mass conservation equation (23) gives the exit Mach number. The potentials along the exit plane are then set so that the gradient of potential along this plane is constant and equal to the y-component of velocity corresponding to the guessed exit flow angle and resluting exit Mach number. The solution of the potential flow is then iterated, keeping the set values of potential along the inlet and exit planes constant. When a converged solution has been obtained the value of velocity at the trailing edge on the pressure surface is compared to that at the trailing edge on the suction surface. If the two velocities are equal then the guessed value of exit flow angle, and the resulting exit Mach number, are correct. If the two velocities are unequal the guessed value of exit flow angle is incorrect and must be altered. The soltuion procedure is then repeated until the Kutta condition of equal velocity at the trailing edge on pressure and suction blade surfaces is achieved. The change of guessed exit flow angle was implemented manually.

The Kutta condition has been used to determine the air-flow angle at the exit plane. From this angle, the Mach number of the flow at the exit plane may be determined from the mass conservation equation (69). Thus the values of Mach number and air-flow angle are known at both inlet and exit plane which for a given blade geometry and blockage completely defines the flow problem, in real flows. However, as will be shown later, the potential formulation can give rise to more than one different flow-field for the same values of inlet and exit Mach number and angle [29] , [30]. This problem of uniqueness of the potential formulation was overcome in the nozzle solution (for which the exit angle was known to equal zero) by comparing the exit pressure predicted by the potential formulation to that of the known back-pressure. A similar approach is used in the potential formulation of the cascade problem. This requires that the static pressure ratio across the blade be known a priori, which together with the total pressure and Mach number at inlet specify the value of the static pressure at exit. We now require that the static predicted by the potential solution at exit equals this given static pressure.

The Kutta condition is used to determine the value of the exit air-flow angle and thence the value of the exit Mach number. It is ensured that W_y at exit is equal to the W_y corresponding to this angle and Mach number, by setting the gradient of potential along the exit plane equal to W_y at all nodes on that plane. Thus the gradient of potential in the y-direction is specified but not the actual values of potential themselves. However, it is both the absolute values of potential at exit and their gradients which uniquely specify the potential flow solution. Thus, once the Kutta condition has been satisfied, the predicted static pressure at exit is compared to the known value of static pressure. If the two are equal the solution is complete and the flow is uniquely specified. If the values of predicted and known static pressure at exit are not equal then the set values of potential at exit must be altered

so that their absolute values change but their gradient in the y-direction remains unaltered. Thus the values of the air-flow angle and hence Mach number at exit remain unchanged. The solution procedure is then repeated with these new values of potential at exit until equality is achieved.

In summary, referring to Figure (8) , the boundary condition along AH is:

$$\phi_{(n)} = C_{(n)} \tag{71}$$

i.e. the values of potential at inlet are specified
Along HG and AB:

$$\phi_q = \phi_p + SW_{y_1} \tag{67}$$

i.e. the periodicity condition
Along GF and BC:

$$\frac{\partial \phi}{\partial n} = 0 \tag{63}$$

i.e. the know through flow condition
Along FE and CF:

$$\phi_q = \phi_p + SW_{y_2} \tag{68}$$

i.e. the periodicity condition
and along DE:

$$\phi_{(n)} = D_{(n)} \tag{72}$$

i.e. the values of potential are specified
C_n and D_n are two sets of values of potential which satisfy certain conditions and they remain invariant as the solution is iterated.

2.5.3 Total Pressure Loss

The potential solution of transonic flows is an isentropic solution and is, one its own, incapable of predicting a loss in total pressure, for example, across the shock-wave. However, an estimation is made of the total pressure loss across the shock-wave by the application of the standard one-dimensional shock relations. The total pressure between the inlet plane and the shock is then assumed constant, a step loss in total pressure is imposed at the shock, and this reduced total pressure is assumed downstream of the shock until the exit plane.

The estimated total pressure loss is updated after each iteration to take into account any change in predicted shock strength from iteration to iteration. This imposed total pressure loss will effect the values of the densities calculated downstream of the shock, and will thus effect the coefficients of the discretized potential equation and the ultimate solution itself.

The loss in total pressure is estimated along each row as being dependant on the shock strength predicted along that row. The total pressure downstream of the shock is thus estimated as being different along each row and no mixing of these total pressure was assumed. For the determination of the predicted exit static pressure, therefore, a mass averaged static pressure was calculated for the exit plane and taken as the predicted exit static pressure.

2.6 The Solution of the Discretized equations

2.6.1 Succesive-Line-Over-Relaxations

Using finite-difference approximations, with artificial viscosity introduced to model the domain of dependence of supersonic regions of flow, the conservative potential equation is represented by a set of elliptic algebraic equations. Together with the relevant boundary conditions one equation is derived for each node in the computational domain, relating the velocity-potential at that node to the velocity-potential at neighbouring nodes. The conservative potential equation (23) is expressed as:

$$(\rho b)_x \phi_x + (\rho b)\phi_{xx} + (\rho b)_y \phi_y + (\rho b)\phi_{yy} = 0 \qquad (73)$$

For any one sweep the distribution of density is taken from the most recently computed potential distribution, the blockage factor is specified and remains invariant Finite-difference approximations are, therefore, required for the following derivatives of potential:

$$\phi_x, \quad \phi_{xx}, \quad \phi_y, \quad \phi_{yy}$$

The replacement of these partial derivatives with their finite difference approximations thus produces a set of simultaneous elliptic algebraic equations in velocity potential. This set of equations may be expressed in a matrix formulation as:

$$[A] \; [\phi] \; = [K] \qquad (74)$$

where $[A]$ is a matrix of size $NP \times NP$ containing the coefficients of the potentials for every node. $[\phi]$ is the matrix of the potentials for every node from ϕ_1 to ϕ_{NP}, and $[K]$ is the matrix containing the terms on the right-hand side of

equation (73) for every node. This matrix $[K]$ is of size NPx1 and contains a zero term for each node in the subsonic flow regime, but a non-zero term corresponding to the explicit artificial viscosity for every node in the supersonic flow regime. NP is the number of nodes at which the velocity potential is unknown. It is, in theory, possible to directly invert the matrix $[A]$ to give a solution to the potential at all NP nodes simultaneously. Repeating this technique, updating the coefficients of A after each iteration, should then give increasingly better solutions to the governing flow equations until the final potential solution satisfies these equations to some acceptable degree. Such a technique was attempted but was found to exhibit a divergent behaviour. An alternative approach is thus required and one family of methods which has found much favour in the solution of large numbers of finite-difference equations is the matrix block iterative techniques. These usually involve considering each row or column (or both) of nodes as a separate block, and employing an iterative technique which solves for each block seperately. By utilising such a technique it is possible to write the complete set of equations (24) as :

$$\begin{bmatrix} C_2 & D_2 & & & & \\ B_3 & C_3 & D_3 & & & \\ A_4 & B_4 & C_4 & D_4 & & \\ & & & & & \\ & & & & & \\ & & A_{N-2} & B_{N-2} & C_{N-2} & D_{N-2} \\ & & & A_{N-1} & B_{N-1} & C_{N-1} \end{bmatrix} \begin{bmatrix} \bar{\phi}_2 \\ \bar{\phi}_3 \\ \bar{\phi}_4 \\ \\ \\ \bar{\phi}_{N-2} \\ \phi_{N-1} \end{bmatrix} = \begin{bmatrix} \bar{K}_2 \\ \bar{K}_3 \\ \bar{K}_4 \\ \\ \\ \bar{K}_{N-2} \\ K_{N-1} \end{bmatrix} \qquad (75)$$

where N is the number of vertical columns of nodes in the computational domain. The equations for the potentials along the inlet column (i=1) and the exit column (i=N) do not feature as the potentials along both these columns are specified and treated as known. Each of the terms A_i, B_i, C_i, ϕ_i and K_i in equation (75) are matrices themselves, giving the governing equations for the potential of the nodes along column i. Considering the set of equations (75) in more detail it can be seen that each matrix C_i is an irreducible matrix of size m x m whose non-zero entries give the coupling of any node on the column i with its neighbours on that column. With the nine-node central-differenced lattice of Figures 3 & 4, C_i has the following general form.

$$C_i = \begin{bmatrix} c_1 & d_1 & e_1 & & & & & & \\ b_2 & c_2 & d_2 & e_2 & & & & & \\ a_3 & b_3 & c_3 & d_3 & e_3 & & & & \\ & & a_n & b_n & c_n & d_n & e_n & & \\ & & & & a_{m-2} & b_{m-2} & c_{m-2} & d_{m-2} & e_{m-2} \\ & & & & & a_{m-1} & b_{m-1} & c_{m-1} & d_{m-1} \\ & & & & & & a_m & b_m & c_m \end{bmatrix}$$

where m is the number of nodes per column of the computational grid. Note that if $n < m/2$, then $a_n = 0$, else $e_n = 0$. Thus the velocity potential at any node on column i, away from the boundaries, is a function of the velocity potential at three other nodes on that same column.

The matrix B_i is a matrix of size mxm, whose non-zero terms contain the coupling coefficients of any node on column i with those nodes on the preceding column i-1. For the nine node central-differenced lattice, as before, the matrix B_i has the following general form:

$$B_i = \begin{bmatrix} g_1 & & & & & & & & \\ f_2 & g_2 & & & & & & & \\ & f_3 & g_3 & & & & & & \\ & & & & & & & & \\ & & & & & & & & \\ & & & & & & & & \\ & & & & & & f_{m-1} & g_{m-1} & \\ & & & & & & & f_m & g_m \end{bmatrix}$$

The matrix A_i is a matrix of size mxm, whose non-zero terms contain the coupling coefficients of any node on column i with those nodes on the column i-2. For the nine node central-differenced lattice, A_i has the following general form:

$$A_i = \begin{bmatrix} h_1 & & & & & & & & \\ & h_2 & & & & & & & \\ & & h_3 & & & & & & \\ & & & & & & & & \\ & & & & & & & & \\ & & & & & & & & \\ & & & & & & h_{m-1} & & \\ & & & & & & & h_m & \end{bmatrix}$$

D_i is a matrix of size mxm whose non-zero terms contain the coupling coefficients of any node on column i with those nodes on the following column i+1.
Thus, for the nine-node central-differenced lattice, the matrix D_i is of the following general form:

$$D_i = \begin{bmatrix} q_1 & r_1 & & & & \\ p_2 & q_2 & r_2 & & & \\ & p_3 & q_3 & r_3 & & \\ & & & & & \\ & & & & p_{m-1} & q_{m-1} & r_{m-1} \\ & & & & & p_m & q_m \end{bmatrix}$$

The matrix $\bar{\phi}_i$ is the matrix containing the velocity potentials of all nodes on column i. Thus $\bar{\phi}_i$ has the form:

$$\bar{\phi}_i = \begin{vmatrix} \phi_1 \\ \phi_2 \\ \phi_3 \\ \\ \\ \\ \phi_{m-1} \\ \phi_m \end{vmatrix} \qquad \bar{K}_i = \begin{vmatrix} K_1 \\ K_2 \\ K_3 \\ \\ \\ \\ K_{m-1} \\ K_m \end{vmatrix}$$

where $\bar{K}_i$ is the vector of constants containing the terms on the Right-Hand-side of the flow equations which determine the potentials on column i.

The matrices A_i, B_i, C_i, and D_i are sparse matrices banded around the diagonal. The non-zero terms of these matrices need not be stored nor utilized in the matrix manipulations.

The governing flow equation (23) may then be replaced at any general node on column i and now j, thus:

$$h_{ij}\,\phi_{i-2,j} + f_{i,j}\,\phi_{i-1,j-1} + g_{i,j}\,\phi_{i-1,j} + a_{i,j}\,\phi_{i,j-2}$$

$$+ b_{i,j}\,\phi_{i,j-1} + d_{i,j}\,\phi_{i,j+1} + p_{i,j}\,\phi_{ih,j-1} + q_{i,j}\,\phi_{ih,j}$$

$$+ r_{i,j}\,\phi_{ih,j+1} + c_{i,j}\;\;i,j = k_{i,j} \qquad (76)$$

where $j > m/2$; or :

$$h_{i,j}\,\phi_{i-2,j} + f_{i,j}\,\phi_{i-1,j-1} + g_{i,j}\,\phi_{i-1,j} + b_{i,j}\,\phi_{i,j-1}$$

$$+ d_{i,j}\,\phi_{i,j+1} + e_{i,j}\,\phi_{i,j+2} + p_{i,j}\,\phi_{i+1,j-1} + q_{i,j}\,\phi_{ih,j}$$

$$+ r_{i,j}\,\phi_{ih,j+1} + c\phi_{i,j} = k_{i,j} \qquad (77)$$

where $j < m/2$

Thus the governing flow equations for every node along column i is represented by:

$$[A]_i\,[\phi]_{i-2} + [B]_i\,[\phi]_{i-1} + [C]_i\,[\phi]_i + [D]_i\,[\phi]_{i+1} = [k]_i \qquad (78)$$

The values of the velocity potentials at the nodes along column i, $[\phi]_i$, may be determined simultaneously using

a block-iterative technique known as Successive-Line-Over-Relaxation (SLOR). In this technique expressions involving the potential of nodes not on the column i are taken over to the right-hand side of equation (73). Thus if we solve for successive columns, from inlet towards exit, and always utilize the most recently determined value of potential at any node, the potential along column i at iteration (ℓ+1) may be express as:

$$[C]_i \, [\hat{\phi}]_i^{(\ell+1)} = [k]_i - [A]_i \, [\bar{\phi}]_{i-2}^{(\ell+1)} - [B]_i \, [\bar{\phi}]_{i-1}^{(\ell+1)} - [D]_i \, [\phi]_{i+1}^{(\ell)} \qquad (79)$$

The right-hand side of equation (79) is easily determined using standard matrix techniques of multiplication and addition. Thence, by inverting the matrix C_i it is possible to determine the potential, $[\hat{\phi}]_i^{(\ell+1)}$, which satisfies equation (74). The potential at column i for iteration ℓ+1 is, however, modified so that it is a function of the potential at column i for iteration ℓ, as well as that at iteration ℓ+1.Thus:

$$[\bar{\phi}]_i^{(\ell+1)} = w\left([\hat{\phi}]_i^{(\ell+1)} - [\phi]_i^{(\ell)}\right) + [\phi]_i^{(\ell)} \qquad (80)$$

If w is equal to unity then we have the Gauss-Seidel Block Iteration scheme where the function of the potential at a new iterative sweep is not constrained in any manner by the value at the previous sweep. If w is greater than unity, the change in potential from one iteration to the next is greater than it would be for the Gauss-Seidel Block Iterative scheme. This is termed over-relaxation and is used to accelerate the convergence of the iterative technique towards the asymptotic solution, where the solution remains unchanged for further iterations. Over-relaxation is commonly used where the stability of the governing system of equations is high. However, in many cases over-relaxation can cause the iterative solution scheme to diverge. In such

cases, under-relaxation must be used. Under-relaxation involves the use of a relaxation factor, w, which is less than unity. A few different values of relaxation factor were attempted in the solution of the flow equations, in this report, and an optimum value of w = 0.45 was determined. For values other than this the solution either required more iterations to achieve the same convergence criteria, or failed to converge at all.

Using this Line-Relaxation technique the potentials were first determined at the most upstream column at which the potentials are unknown. The potentials are then determined at succesive downstream columns until the potential has been determined at every node in the computational domain. From this new potential-distribution a new density distribution is determined which, from equation (73) will slightly alter the matrix equations of flow for every column. Thus using this new potential distribution the procedure is repeated, sweeping from the inlet plane to the exit plane until some pre-determined convergence criteria is satisfied. It was felt that sweeping in a downstream direction best modelled the true physical behaviour of the flow in which disturbances in regions of high Mach numbers tend to propagate downstream much more readily than they do upstream. An alternative approach was attempted in which the solution swept alternatively in an upstream and then a downstream direction, but was not found to be significantly different from sweeping in a solely downstream direction.

2.6.2 Convergence Criteria

The convergence criteria utilized to determine when the iterative solution has converged is, too some degree, arbitary. The most commonly used criteria is to insert the values of potential determined by the last iteration $\left[\hat{\phi}\right]_i^{\ell+1}$

into equation (79) and determine the values of the left and right-hand sides of this equation. The difference between these two values is the residual, a measure of the degree of accuracy of the solution procedure. Summing the residuals for each column gives a total residual and this is usually required to be less than some chosen value. The maximum permissible value of the residual is usually chosen as between 10^{-5} and 10^{-7}. The smaller the value of this maximum permissible residual then the more accurate the final solution, but the more the iterations that are required to achieve this solution. Thus for each iteration, the total summed residual must be determined and compared to a chosen value. If the residual is greater than this value the solution must progress a further iteration until finally the residual is less than the chosen value. The determination of this residual does, however, involve a fairly large number of computer operations and, in this report, a different convergence criteria has been utilised.

The convergence criteria utilized in this report is simply the sum of the difference in potentials determined at iteration $\ell+1$ and that at iteration ℓ. This difference is divided by the local mesh spacing and is summed over all the nodes. The division by the mesh spacing means that the total value is now representative of the difference in velocity, from one iteration to the next, rather than the difference in potential. This total is compared to some chosen value and if it is less than this value the solution is said to have converged; Else the solution must progress a further iteration. For a computational mesh with approximately 1000 nodes it is usually required that this sum of the charges in potential from one iteration to the next, divided by the local mesh spacing, is less than a value between 500 and 1000 for convergence to have been satisfied. This signifies that the average change in velocity at each point is less than a value between 0.5 m/s and 1.0 m/s, from one iteration to another. For average velocities in the flow-field of about 300 m/s, this signifies that at a

converged state, the average change in velocity at a node, from one iteration to the next is between 0.16% and 0.33%. The advantage of such a convergence criteria in a line-relaxation iterative technique is that the change in potential from one iteration to the next must be determined anyway, see equation (80). Thus very little additional computational operations are required which makes the use of such a criteria very efficient in terms of computer run-time.

2.7 The Viscous Correction

Transonic internal flows are strongly dependent on the form and size of the associated boundary layer. In a transonic convergent-divergent nozzle the flow upstream of the shock wave will be accelerating and the boundary-layer in this region will, in general, remain thin. Downstream of the normal shock, however, the flow is subsonic and decelerating. The boundary layer in this region, therefore, experiences an adverse pressure gradient, corresponding to this decelerating flow, causing it to thicken. The deceleration of the flow downstream of the shock is thus reduced and the value of the static pressure at exit of the nozzle would fall if the strength and position of the shock remained unchanged. However this static pressure must always equal the back pressure (which remains unchanged) and the viscous flow adjusts itself to satisfy the condition by reducing the strength of the shock and/or shifting its position upstream of that which it would occupy in the absence of a boundary-layer. The significance of the viscous boundary-layer effects will depend on the geometry and operating conditions of the nozzle but will, in general, have a considerable effect on the performance of the nozzle.

The influence of the boundary-layer on cascade blade flows is more complicated due to the combined effects of change in effective flow area and in blade circulation. These viscous effects will, in general, significantly

affect the flow and account for the deviation of the flow at outlet of the blade-row.

The solution of the flow equations must, therefore, account for viscous effects if an accurate predictions of the flow is required. This is achieved by the application of a transpiration type of boundary-layer displacement model, in which the approach fluid is assumed to flow through the solid walls at a rate sufficient to displace the mainstream along these surfaces by one boundary-layer displacement thickness. This approach has been used by many authors including Denton [9] and Ives and Liutermoza [25]. For an inviscid calculation the boundary conditions require that the flow normal to the solid walls is zero. To account for fluid viscosity, this is modified so that the flow normal to these surfaces is no longer set equal to zero, but instead set equal to the local value of the transpiration velocity V_t. The transpiration velocity may be calculated from the following equation:

$$\rho V_t = \frac{\partial (\rho U_s \delta^*)}{\partial s} \qquad (81)$$

where ρ is the local value of denisty at the surface

U_s is the local value of velocity at the surface

δ^* is the local value of boundary layer displacement thickness, and

s is the distance along the surface.

Thus, to know the distribution of transpiration velocity we must calculate the distribution of boundary layer displacement thickness.

2.7.1 Boundary Layer Calculations

In general, the boundary layer will be initially laminar, undergoing a transition to turbulence a small distance downstream of the nozzle inlet. In addition, an interaction is liable to occur between the boundary layer and the shock wave.

2.7.2 Laminar Boundary Layer

The laminar boundary layer was solved using the method devised by Thwaites [31] and since used in a slightly different manner by many authors inlcuding Rangaswamy and Elder [32] This method is based on the Von Kármán momentum integral equation, first derived in 1921 [33], and makes no assumption as to the form of the velocity profile within the boundary layer. The momentum integral equation may be expressed in the following form:

$$\frac{d\theta}{dx} + \frac{\theta}{U_s}(2+H)\frac{dU_s}{dx} = \tfrac{1}{2} C_f \qquad (82)$$

in which

$$H \equiv \delta^*/\theta \qquad (83)$$

where: H is the shape factor of the boundary-layer profile
δ^* is the boundary-layer displacement thickness
θ is the boundary-layer momentum thickness
C_f is the skin friction coefficient
and U_s is the velocity at the outer edge of the boundary-layer (assumed to be the velocity along the solid surface derived from the potential flow solution)

The momentum integral equation contains too many unknowns, θ, H and C_f (U_s is known from the potential flow calculation), to be useful by itself and so it is supplemented by algebraic equations among the unknowns. Such relations are simpler in terms of the dimensionless variables and we, therefore, make θ and x dimensionless by forming Reynolds numbers:

$$Re_\theta \equiv \frac{\rho U_s \theta}{\mu} \qquad (84)$$

$$Re_x \equiv \frac{\rho U_s x}{\mu} \qquad (85)$$

where μ is the coefficient of absolute viscosity.

Although H and C_f are already dimensionless, the skin friction coefficient is rather a strong function of the Reynolds number. Thus we introduce the parameter

$$\ell \equiv \tfrac{1}{2} \mathrm{Re}_\theta C_f \tag{86}$$

which is independent of the Reynolds number, not only for the flat-plate problem but for broad classes of exact solutions of the boundary layer equations.

Thus we multiply the momentum integral equation (82) through by Re_θ to get

$$\frac{\rho U_s \theta}{\mu} \frac{d\theta}{dx} + \frac{\rho \theta^2}{\mu} (2+H) \frac{dU_s}{dx} = \ell \tag{87}$$

Thwaites defined a dimensionless pressure gradient parameter

$$\lambda \equiv \frac{\rho \theta^2}{\mu} \frac{dU_s}{dx} \tag{88}$$

and rewrote the above equation as

$$\frac{\rho U_s}{\mu} \frac{d\theta^2}{dx} = 2 \quad \ell - (2+H) 2 \tag{89}$$

If we use Pohlhausen's quatic velocity profile, ℓ and H can be shown to be functions only of λ. Thwaites found that, to an excellent approximation, the same is true of the available, exact solutions of the laminar boundary layer equations.

That is, when the values of ℓ and H for such solutions are plotted against λ, the data cluster around a single curve with very little scatter. In fact, the right side of equation (89) is very well approximated by the linear formula

$$2 \left[\ell - (2+H) \lambda \right] \simeq 0.45 - 6\lambda \tag{90}$$

When this and the definition (83) of λ are substituted into equation (84), we obtain.

$$\frac{\rho U_s}{\mu} \frac{d\theta^2}{dx} = 0.45 - 6 \frac{\rho \theta^2}{\mu} \frac{dU_s}{dx} \tag{91}$$

which we can rearrange to give:

$$\frac{\rho}{\mu} \frac{d}{dx} (\theta^2 U_s^6) = 0.45 \, U_s^5 \tag{92}$$

We can rewrite this equation in terms of the dimensionless variables:

$$\tilde{U}_s = U_s / V_{ref}$$
$$\tilde{x} = x / L_{ref}$$
$$\tilde{\theta} = \theta / L_{ref}$$

giving

$$\tilde{\theta}^2 = \frac{0.45}{Re} \frac{1}{\tilde{U}_s^6} \int_0^{\tilde{x}} \tilde{U}_s^5 \, d\tilde{x} \tag{93}$$

Thus for any given distribution of $U_s(x)$, the distribution of $\theta(x)$ can be readily determined by the integration of a single first-order differential equation. Once θ is known λ can be calculated from equation (88) and $H(\lambda)$ then calculated from an empirical relation, proposed by Dunham [34] :

$$H = 1.622 \, (\lambda + 0.11)^{-0.209} \tag{94}$$

Thus the distribution, $\delta^*(x)$, of the boundary-layer displacement thickness may be determined.

The integral of equation (93) is numerically approximated using the trapezoidal rule.

2.7.3 Transition from a Laminar to a Turbulent Boundary-Layer

In the general case of flow past a solid surface, the boundary layer is initially laminar. However, sooner or later, all boundary layers become unstable and any small disturbance initiates transition to the unsteady turbulent state. Transition starts at a particular value of Reynolds number (Re_{crit}) based on the distance x, along the surface, from the start of the boundary layer.

Transition to turbulence is not an instantaneous process. Instead the flow is intermittently laminar and turbulent over a certain length of surface. The length of this transition regime, upwind of which the flow is always laminar and downwind of which the flow is always turbulent, can be much larger than the length over which the flow is purely laminar. The skin friction usually increases dramatically across the transition region and it would, therefore, be desirable to utilise an integral method to describe the transition process. As no such method exists it is necessary in calculating boundary-layer growth by an integral method to assume that the flow changes instantaneously from laminar to turbulent at a transition point. It is usual to assume that transition occurs when the Reynolds number based on the momentum thickness (Re_θ) is greater than some critical Reynolds number (Re_{crit}). The value of this critical Reynolds number depends on many factors as discussed by Schlichting [35]. Probably the two most important factors are the pressure gradient imposed on the boundary layer by the inviscid flow and the roughness of the surface along which that fluid is flowing. An increase in either surface roughness or positive pressure gradient will hasten transition or, looked at another way, will decrease the critical value of Reynolds number.

In this report, the value of the critical Reynolds number was based upon a modified form of Seyb's correlation. Instantaneous transition from a laminar to a turbulent boundary layer was assumed to occur when the value of λ (see equ. 88) was greater than -0.09 or when $Re_\theta > Re_{crit}$, where:

$$Re_{crit} = \frac{10^3}{1.2 + 0.7T_u} + 10 \left[\frac{\lambda + 0.09}{0.0106 + 0.036T_u} \right]^{2.62} \qquad (95)$$

and T_u is the percentage of turbulence (assumed to lie between 0.15% and 4%).

This formula for critical Ryenold's number does account for the effect of pressure gradient, although indirectly, because the momentum thickness grows more rapidly in a positive pressure thereby increasing Re_θ. However, the influence of surface roughness is ignored which limits the situations to which this correlation may be applied. Fortunately this correlation was based on data taken on turbomachinery cascades and should be applicable to other airfoils and nozzles with a similar degree of surface roughness. As can be seen, the influence of mainstream turbulence is also taken into account.

As will be discussed later, the method used to calculate the turbulent boundary layer from immediately downstream of the transition point onwards, is based on Head's set of equations. This method solves two simultaneous first-order ordinary differential equations and two initial conditions are required, therefore, to start the calculations. Thwaite's method gives values of θ, H and C_f up to the transition point, but H and C_f change drastically during transition so that only the initial turbulent vlaue of θ can be taken from the laminar calculations. The initial turbulent value of the shape factor, H_I, is given by the relations proposed by Maskell [36] ,

where:

$$H_I = 1.754 - 0.0647 \ln(Re_\theta) + 0.001916 \left[\ln(Re_\theta)\right]^2$$

if $\lambda > 0$ or $\lambda < 0$ and $Re_\theta > 2{,}500$

and

$$H_I = 1.754 - 0.0647 \ln(Re_\theta) + 0.001916 \left[\ln(Re_\theta)\right]^2 + \left[1.32 - 126\ (Re_\theta)^{-0.752}\right]^{-4}$$

when $\lambda < 0$ and $Re_\theta < 2{,}500$ (96)

Thus, two initial conditions are known and the solution of the turbulent boundary layer calculations can progress.

2.7.4 Turbulent Boundary Layer

The method used to predict the turbulent boundary-layer growth is based on that devised by Head [37] and widely used, with slight modifications, by many authors including Green [38]. Head proposed that the turbulent boundary layer growth be predicted by the simultaneous forward integration of the Von Kármán momentum integral equation and the entrainment equation. The entrainment equation is an expression for the streamwise rate of change of the mass flow thickness, which may be written as:

$$\frac{d\Delta}{dx} = C_E - (1-M_s^2)\frac{\Delta}{Us}\frac{dUs}{dx} \tag{97}$$

where M_s is the Mach number at the edge of the boundary-layer and Δ is the mass flow thickness defined as:

$$\Delta = \int_0^\delta \frac{\rho U}{\rho_s U_s}\, dy \tag{98}$$

where y is normal to the surface.

Δ is the ratio of the mass of fluid flowing through the boundary layer to that which would flow through the boundary-layer if all the fluid within were at velocity equal to that at the outer edge of the boundary-layer.

C_E is the entrainment coefficient defined as:

$$C_E = \frac{1}{\rho_s U_s} \frac{d}{dx} (\rho_s U_s \Delta) \qquad (99)$$

It can be seen from the form of equ. (99), that the entrainment coefficient represents the rate at which fluid from the outer (inviscid) flow is entrained by the boundary-layer.

Whilst, in calculating the growth of the laminar boundary-layer the outer flow was assumed incompressible (a fair assumption if the pressure ratio across the nozzle is not too high and transition occurs fairly rapidly) the same cannot be assumed in calculating the growth of the turbulent boundary layer. Hence the presence of a Mach number in equation (97). The momentum integral equation is also used in its compressible form:

$$\frac{d\theta}{dx} = \frac{Cf}{2} - (H + 2 - M_s^2) \frac{\theta}{U_s} \frac{dUs}{dx} \qquad (100)$$

which when combined with equation (97) gives:

$$\frac{\theta dH_1}{dx} = C_E - H_1 \left(\frac{Cf}{2} - (H+1) \frac{\theta}{Us} \frac{dUs}{dx} \right) \qquad (101)$$

where $H_1 = \Delta/\theta = (\delta - \delta^*)/\theta$ (102)

Thus we have two simultaneous first order differential equations, (100) and (101), expressing gradients of θ and H_1 respectively. However, the additional unknowns C_E, C_f and H feature in these equations and we, therefore, require additional relations in these variables to be able to solve the set of equations.

The additional relations used are the Ludwieg and Tillman skin friction relation:

$$C_f = 0.246\ Re_\theta^{-0.268}\ e^{-1.56H} \tag{103}$$

the Cebeci and Bradshaw [39] correlations for the relation between H_1 and H:

$$\left.\begin{aligned} H_1 &= 3.3 + 0.8234(H-1.1)^{-1.287} \quad \text{for } H \leq 1.6 \\ \text{and} \\ H_1 &= 3.3 + 1.5501(H-0.6798)^{-3.064} \quad \text{for } H > 1.6 \end{aligned}\right\} \tag{104}$$

and finally the relation between C_E and H_1 given by Thompson [40] as a fit to Head's graphical relationships:

$$C_E = 0.0299\ (H_1-3.0)^{-0.6169} \tag{105}$$

Thus we have 5 equations (100,101, 103, 104 and 105) in 5 unknowns (θ, H_1, H, C_E and C_f) and given that we have initial values of two of the unknowns, in this case θ and H_1 we can simultaneously integrate the two ordinary differential equations to give the turbulent boundary-layer growth. The numberical method chosen to integrate these two equations is the Runge-Kutta method, widely used for the numerical integration of one or more ordinary differential equations.

2.7.5 Boundary-Layer Interaction with the Shock Wave:

The interaction between a normal shock wave in transonic flow over a solid surface and the boundary-layer along that surface is extremely complicated and has received considerable theoretical attention (see Ref. [41] for a critical review). There are two opposing schools of thought as to whether this interaction should be treated in a special way.

Lock [42] argues that no special treatment of the interaction is necessary. Instead he believes that it is sufficient merely to regard the interaction as a region in which an ordinary turbulent boundary-layer is subject to a local rapid rise in pressure, followed by a milder (but usually still adverse) pressure gradient. This approach was initially proposed by Green [43], who suggested that, provided the pressure jump through the shock-wave is spread over a few boundary-layer ticknesses, then any reliable method of calculating turbulent boundary-layers should be expected to predict the main effect of the interaction on the subsequent development of the boundary-layer. This approach is subject to the boundary-layer remaining attached and may require some artificial smearing of the flow property changes across the shock. The relative success of this procedure can be judged by the encouraging results obtained by many authors, for example, Bauer, Garabedian, Korn and Jameson [44], Bavitz [45], Collyer and Lock [46] and Melnik [47].

Nandan, Stanewsky and Inger [48], however, argue that a more detailed and physically correct treatment is required of the interaction of the boundary layer with the shock wave. This is necessary because of the way this interaction governs the way the boundary-layer responds to the subsequent adverse pressure gradients, thereby influencing the flow conditions at the exit plane of the nozzle (or the trailing-edge of an airfoil). Their flow solution is obtained by embedding an analytical solution for near-normal shock/boundary-layer interaction as a module within a boundary-layer inviscid flow computation code. For the analytical solution of the interaction a nonasymptotic triple deck disturbance model is employed. This model comprised an upper mixed flow region, outside the boundary layer, consisting of an incoming potential supersonic flow and a subsonic potential flow separated by a given shock discontinuity. Below these regions lay a doubly-infinite nonuniform boundary-layer region,

containing a highly rotational, mixed transonic linear disturbance flow. Near the wall, lay a viscous disturbance sublayer containing the upstream influence and the skin friction perturbation.

The results obtained using the above model to describe the shock/boundary-layer interaction showed that, in some cases, although the error in not treating the interaction in a special way was small in the region of the shock, this error was amplified as the solution was integrated downstream. Thus Nandanan, Stanewsky and Inger argued that an analytical treatment of the interaction was necessary to ensure accurate computation.

A third approach is possible, however, though it has until now found little application. This consists of applying correlations obtained from experimental data, relating the change in the boundary layer variables of shape factor and momentum and displacement thickness with the outer flow variables of Mach number and mainstream turbulence before the shock. Although further experimental data is needed, before the correlations are perfected it is possible to make first order approximations from data obtained by Raghunathan and McAdam [49] and Kooi [50].

No attempt has been made, in this report, to model analytically the shock/boundary-layer interaction. Instead the pressure rise across the shock was smeared and the boundary layer then solved merely as if it was in the presence of a strong pressure gradient. However a small step change in shape factor was imposed across the shock so that the total change in shape factor across the smeared shock was of a magnitude indicated by Ragunathan and McAdam.

2.7.6 Boundary Layer Separation

If the flow in a boundary-layer experiences an adverse pressure gradient, it will lose momentum in flowing

against this pressure gradient. If the region of adverse pressure gradient is of sufficient length, there will come a point at which some of the fluid in the boundary-layer will have lost all of its initial momentum and will stagnate. Further past this point some fluid will under the influence of the pressure gradient, have reversed its original direction and will flow in an opposite direction to that of the outer inviscid flow. The point at which the boundary-layer flow stagnates varies across a plane normal to the solid surface. The flow nearest the wall, will, in general, have had the least initial momentum before it experienced the adverse pressure gradient, and will therefore, be the first to stagnate. Flow further from the wall will stagnate a point further downstream. Thus, there will appear a locus of points within the boundary layer at which the velocity, u, is zero. Also, there must be one streamline, a dividing streamline, which separates streamlines that reverse their direction at the u=0 locus, from those that start further upstream. This streamline, because of the variation at which the boundary-layer fluid stagnates, comes out of the wall and the flow is said to have separated from the solid boundary. That is, the streamlines no longer follow the wall.

This phenomenum is termed boundary-layer separation. The onset of separation can usually be determined by monitoring the value of the shape factor, H, as the boundary layer solution is integrated downstream. If the value of H suddenly rises sharply reaching a value of approximately 2.4 or greater, then the boundary layer can be assumed to have separated. Eqns (104) relating H_1 to H are no longer valid, once separation has occured. Fortunately an alternative relation exists, as used by Heritage [51], which is valid in the region and downstream of boundary-layer separation

$$H_1 = \frac{H(0.5H + 1)}{H-1} \qquad (106)$$

This relation has been used in this report, where separation has been detected.

3 RESULTS AND DISCUSSIONS

3.1 The Inviscid Solution of the Nozzle Problem

Figure (9) shows the solutions obtained for the components of velocity in the axial (x-) direction against axial distance from nozzle inlet, along both the centre-line and the wall of the two-dimensional, symmetrical convergent-divergent nozzle specified in Table (2). The values of the inlet total temperature and pressure were 293.15(K) and 93428.0(Pa) respectively, and the value of the back pressure was 79040.06 (Pa). The fluid was assumed to be air with a ratio of specific heats equal to 1.4 and the gas constant, R, was taken as 288.7 KJ/KgK. The numerical solution scheme, 2D-IN, was inviscid, the effects of boundary-layer growth along the nozzle-walls being ignored. Onto Figure (9) have been plotted the results of Damia-Torres [52] , obtained by the application of his inviscid code to an identical nozzle operating under identical conditions.

The general form of the predicted velocity distributions is as expected. A mostly continuous acceleration of the flow is observed until a point some distance downstream of the throat of the nozzle. At this point a sharp fall in velocity is predicted, after which the flow decelerates gradually to the exit of the nozzle. The acceleration of the flow through the entire convergent section, upto the throat and thence through some of the divergent section, indicates that the flow at inlet is subsonic, but that it accelerates through a choked throat (at which the velocity is sonic) to a supersonic value. The predicted sharp fall in velocity represents the discontinuity at the shock wave, across which the total velocity falls from a supersonic to a subsonic value. The gradual deceleration downstream of the shock wave indicates that the flow after the shock-wave is, as expected, subsonic.

A further point of interest is the fact that the sharp fall in velocity along the wall is predicted to occur a small distance upstream of the corresponding point on the centre-line. The significance of this distance being small is that the solution predicts the presence of a nearly (but not exactly) normal shock-wave in the nozzle duct.

The agreement between the velocity distributions predicted by the 2D-IN scheme and those predicted by the inviscid code of Damia-Torres is very good. Only in the region a small distance upstream of the predicted location of the shock wave is the difference between the two solutions significant. The maximum discrepancy is between the value of velocity predicted at the shock and is approximately five percent (5%). However, as Damia Torres readily admits his inviscid code, in particular, results in an overprediction of the values of velocity at the shock, when compared to interpolated values obtained experimentally using Laser-Doppler anemometry. Thus it appears that the present inviscid code (2D-IN) is slightly more accurate, for this test case at least, then the inviscid code of Damia Torres. The number of nodes used in the 2D-IN code is similar to that used in the inviscid code of Damia Torres, approximately 1000. The 2D-IN code required approximately 10 minutes of CPU time on a Perkin-Elmer 3210 mini-computer, corresponding to approximately one-hundred iterations, to achieve a satisfactory convergence. The number of iterations and the CPU time required by the inviscid code of Damia Torres is not known to this author.

It can be seen that the 2D-IN code predicts an undershoot in velocity immediately after the shock, particularly along the wall. This results in the wiggle in velocity distribution after the shock. Such a wiggle is commonly predicted using potential methods to model transonic flows and is caused by the sharp change in artificial viscosity as the flow goes from supersonic

(high artificial-viscosity) to subsonic (zero artificial-viscosity) across the shock. It was not felt that this undershoot was of sufficient magnitude to significantly affect the validity of the solution.

Figure (10) shows the distributions of Mach number, again along the centre-line and the nozzle-wall, predicted by the inviscid 2D-IN solution code for the above nozzle operating at the same conditions as before. The general trends of the predicted Mach-number distributions are similar to those of the axial-velocity distributions.

3.2 The Viscous Solution of the Nozzle-Problem

Figure (11) shows the distributions of axial (x-) velocities, along both the centre-line and the wall of a two-dimensional convergent-divergent nozzle, predicted by a two-dimensional viscous solution procedure, 2D-VI. The nozzle geometry and operating conditions were as in section 3.1. The effects of viscosity were included into the main inviscid code by applying a transpiration model along the nozzle-wall. The growth of the boundary-layer was predicted using integral methods (one for a laminar boundary-layer and the other for a turbulent boundary-layer). A transpiration fluid was then allowed to flow through the nozzle wall of value sufficient to displace the stream-line along the wall by one boundary-layer displacement thickness. Onto Figure (11) have been plotted the predictions obtained by Damia Torres using his viscous-adiabatic Navier-Stokes model applied to the identical nozzle operating under the identical conditions.

The general form of the velocity distributions predicted by the viscous 2D-VI code is similar to those predicted by the inviscid 2D-IN code: The flow accelerates from an initial subsonic value through a choked throat to a supersonic velocity followed by a gradual deceleration of

the flow in the divergent section of the nozzle. The regions of acceleration and deceleration are separated by a sharp drop in velocity signifying the pressure of a shock wave. The difference between the positions of the shock-waves along the centre line and along the wall of the nozzle is greater using the viscous 2D-VI code than that predicted by the inviscid 2D-IN code. Thus, the inclusion of viscous effects results in a prediction of a shock wave across the nozzle which is more curved than that which would be predicted if viscous effects were ignored.

The agreement between the velocity distributions predicted by the viscous (2D-VI) code and those predicted by the viscous code of Damia Torres is good. The values of the maximum velocities (at the shock) predicted by the two viscous codes are very nearly identical. The only difference between the two viscous codes is that the code of Damia Torres predicts slightly lower velocities along the wall after the shock and predicts the shock along the wall at a position slightly upstream, compared to the 2D-VI code.

The viscous potential code predicts finite values of fluid velocity at solid walls, as does the inviscid potential code. In neither code is the no slip condition, that the fluid at solid walls must be at rest, imposed. The viscous correction effects are achieved by imposing a finite value for the potential gradient normal to the wall, whereas in the fully inviscid analysis this gradient is set to zero. In reality the no slip condition does apply and the fluid velocity along a solid wall must be zero. Care must be taken therefore when comparing actual experimentally determined results to those predicted by a viscous-correction type potnetial method. It is suggested that the fluid is measured experimentally just outside the boundary-layer rather than on a solid wall itself.

As mentioned previously the viscous (corrected) 2D-VI code predicts higher values of axial velocity along

the wall, after the wall shock-wave, than does the corresponding code of Damia Torres. The 2D-VI code ensures that, at exit from the nozzle, the flow is uniform. Hence at the exit plane, the velocity of the fluid along the wall is equal to that at the centre-line. This is not the case for the code of Damia Torres, and at exit the velocities predicted by the two codes are slightly different.

Figure (12) gives the velocity-vector plot of the convergent section of the nozzle obtained using the viscous 2D-VI potential code. A velocity-vector has been drawn for every node in the computational flow field in the convergent section of the nozzle, containing the information on both magnitude and direction of the total velocity at each node. Due to the symmetry of the nozzle about its axial centre-line, only the half of the nozzle flow field above this centre-line is shown. Figure (13) gives the corresponding plot of velocity-vectors for the divergent section of the nozzle. From these two vector plots it can be seen that the flow is everywhere smooth. The acceleration in the convergent section is demonstrated by the increase in magnitude of the velocity vectors. In the divergent section the rapid decrease in velocity at the shock and the resulting gradual deceleration to exit is also clearly displayed.

Figure (14) shows the distributions of Mach number, along the centre-line and outer wall, predicted by the viscous 2D-VI potential code for the nozzle operating under the identical conditions as specified previously.

3.3 Comparison Between the Viscous and Inviscid Potential Codes

Figure (15) shows the solutions obtained for the axial-velocity distributions, along the nozzle wall, using both the completely inviscid potential code, 2D-IN,

and the viscous-corrected potential code 2D-VI. The nozzle geometry and operating conditions were as before. It can be seen that for the region from the nozzle inlet to a small distance upstream of the shock, the velocities predicted by the two different potential codes are identical. In this region the flow is accelerating rapidly and the boundary layer remains in consequence, thin. Thus the inclusion of a boundary-layer correction into the inviscid core solution will have little effect on the final solution. Downstream of this region, however, there is a significant difference in the velocity distributions predicted by the two codes. The viscous code predicts the shock position some distance upstream of that predicted by the inviscid code (119.20mm compared to 123.08mm axially from the nozzle inlet). Also, the viscous potential code predicts a lower value of velocity immediately upstream of the shock (399.88 m/s) than that predicted by the inviscid code (419.18 m/s). Downstream of the shock the velocities predicted by the viscous code are slightly higher than those predicted by the inviscid code. Thus, not suprisingly, the greatest discrepancies between the inviscid and viscous potential codes occur in the regions where the boundary-layer grows most rapidly. As can be seen from Figure (16) the boundary-layer grows most rapidly at the shock itself, due to the interaction effects between the shock and the boundary layer. This is responsible for the change in shock position and strength observed to occur with the inclusion of viscous effects. Downstream of the shock the boundary-layer grows gradually due to the adverse pressure gradient and the difference in the velocity distributions predicted by the two potential codes is more modest, though still significant. The effect of viscosity in reducing the predicted shock strength will also reduce the total pressure loss and thus increase the total pressure at exit.

The effect of viscosity in reducing the velocity at the shock and in forcing the shock upstream was also encountered by Damia Torres and by many other researchers in the field. Thus it appears that, qualitatively at least, the influence of the boundary-layer growth on the

nozzle walls has been correctly modelled. The viscous code of Damia Torres predicted velocities after the shock of values lower than that predicted by this inviscid code. The 2D-VI viscous code of this author, however, predicts velocities after the shock of values higher than that predicted by the 2D-IN, completely inviscid, code of this author.

The discrepancy between the velocities near the wall, downstream of the shock, predicted by the viscous code of Damia Torres and that of this author is due to the method whereby the viscous effects are modelled. The code of Damia Torres solves the Navier-Stokes equations utilizing a turbulence model whereas that of this author uses a transpiration flow to introduce viscous effects. Thus the code of Damia Torres will enforce the no-slip conditions along solid walls and will result in low velocities near these walls. The 2D-VI code, however, enforces the no-through flow condition (modified slightly to allow some transpiration) and results in relatively high values of velocity near the walls. Thus it is not surprising that the 2D-VI code predicts higher velocities near the wall, in regions where the boundary-layer is thick, than does the viscous code of Damia Torres. In addition the code of Damia Torres does not assume isentropy and allows for a gain in entropy across the shock and a loss in total pressure due to the viscous losses associated with the boundary-layer. This will also result in a difference in the velocities predicted by the two models, in the region downstream of the shock where the boundary-layer grows sinificantly.

3.4 Prediction of Boundary Layer Displacement thickness

Figure (16) shows the shape of the boundary-layer displacement thickness along the nozzle wall, predicted by the integral method utilized in the 2D-VI code. The nozzle geometry and operating conditions were as before,

and the scale in the y-direction has been stretched by a factor of five so as to magnify the boundary-layer.

From this figure it can be seen that, upstream of the shock wave, the boundary-layer displacement thickness is very small. In this region the flow is accelerating rapidly and the boundary layer encounters, therefore, a strong negative pressure gradient. This negative pressure gradient assists the flow of the fluid within the boundary layer and keeps the boundary-layer thin.

The large jump in boundary-layer thickness, visible in Figure (16) is due to the interaction between the boundary-layer and the shock wave. It is known that such an interaction results in a sudden change in boundary-layer displacement-thickness, momentum thickness and shape factor. The fluid processes occuring within a shock/boundary-layer interaction are very complex and difficult to model. The effects of such an interaction on the boundary-layer development have been introduced by use of correlations, as described in section 2.7.5.

Downstream of the shock-wave it can be seen from Figure (16), that the flow decelerates gradually to the exit plane of the nozzle. The boundary layer in this region will therefore encounter an adverse (positive) pressure gradient. The fluid within this boundary layer will lose momentum in flowing against this pressure gradient and will thicken, as shown in Figure (16).

3.5 The Solution of the Nozzle Flow at a Lower Pressure Ratio

In order to further validate the potential flow models, used in this report, both the 2D-IN and the 2D-VI codes have been applied to the identical nozzle as before operating under different conditions. Figure (17) shows the axial velocity distributions, along both the centre-line

and the wall of the nozzle, predicted using the inviscid 2D-IN potential code. The nozzle geometry was as specified previously but the operating conditions were slightly different. The conditions at the nozzle inlet were exactly as before but the value of the back pressure was increased from its previous value of 79040.06 (Pa) to 82040.06 (Pa). Thus the nozzle is modelled operating at a lower total inlet-to-exit static pressure ratio. No results obtained using either of the potential codes of Damia Torres were available for the nozzle operating at this pressure-ratio and instread the velocity-distribution predicted by the analytic one-dimensional method has also been plotted onto Figure (17).

Comparing the velocity predictions obtained from the 2D-IN code applied to the nozzle operating at the higher value of pressure ratio, Figure (9), to those obtained by application of the same code to the same nozzle operating at the lower value of pressure ratio, Figure (17), reveals the following: The values of velocities predicted for the two cases are very nearly identical in the region from nozzle inlet to the position at which the shock occurs in the lower pressure-ratio case. For the case of the lower operating pressure-ratio, however, the shock along both the wall and the centre-line is predicted as occuring some distance upstream of the corresponding location of the shock predicted for the case of the higher operating pressure ratio. Also the value of the velocity at the shock has decreased as the shock has moved upstream as a result of the increase in back-pressure. Thus the 2D-IN unviscid potential code predicts that the shock moves towards the throat with an accompanying decrease in velocity at the shock, as the back pressure is increased. This is exactly the effect expected from established convergent-divergent nozzle theory and that this behaviour occurs has been proven conclusively by experimental observation. It appears, therefore, that the 2D-IN code reacts correctly to a change in nozzle operating conditions.

Figure (18) shows the distributions of x-velocities predicted by the viscous 2D-VI potential code for the above nozzle operating at the higher value of back pressure (pb = 82040.06), with the inlet conditions as before. Comparing these results to those predicted by the same code for that nozzle operating with a lower value of back pressure, Figure (11), and it can be seen that the viscous potential code reacts to a change in nozzle-operating conditions in a similar manner to that of the inviscid potential code: An increase in back pressure forces the shock towards the throat and reduces the value of velocity at the shock.

Figures (19) and (20) shows the distributions of Mach number along the nozzle wall predicted by the inviscid and viscous potential codes respectively, for the nozzle operating at the lower value of inlet-to-exit pressure ratio.

3.6 The Convergence of the Solution

The value of the change in velocity potential, from iteration to iteration, divided by the local value of mesh spacing is calculated for each node in the flow field as the solution progresses. The sum of these (absolute) values at all nodes then represents the total change in velocity at all nodes and gives an indication as to how well the solution has converged. Convergence is assumed to have occured, and the solution terminated, when this sum falls below some predetermined value. In figure (21) this sum, called for convenience the residual, is plotted against the number of iterations completed for the inviscid solution procedure, 2D-IN. The nozzle geometry and inlet operating conditions were as before and the back pressure was 79040.06 Pa. The residual initially decays rapidly and then approaches asymptotically some near-zero value, signifying that a satisfactory convergence of the solution has been achieved. The solution was assumed to have

converged when the value of this residual fell below 500. As the solution was achieved on a computational mesh of 1000 nodes this signifies that the average change in velocity, from iteration to iteration, was on average 0.5m/s. A change of a mere 0.17% approximately. Note that this residual is not the residual often used to express convergence [11] where the calculated values of potential are inserted into the governing flow equations at each node and the difference in the L.H.S. and the R.H.S. of the equations are summed. This alternative form of residual was determined for the above case. At convergence, where the residual calculated in the fomer manner was about 500, the residual calculated in the alternative manner was 6.59×10^{-6}.

In Figure (22) the value of the residual after each iteration is displayed for the viscous 2D-VI code applied to the nozzle operating at the above conditions. The behaviour of this residual is similar to that for the inviscid potential code, but the decay in the value of the residual is subject to some oscillation. This is caused mostly by the change in values of the transpiration velocity of the fluid allowed to flow through the nozzle-wall, from iteration to iteration, required to model the viscous effects. The boundary-layer calculation is updated after each iteration and hence the distribution of transpiration velocity changes likewise. During the latter iterations some of the oscillation in the value of the residual is also due to the change in the value of the velocity potential at exit required to match the exit static pressure predicted by the solution to the known value of nozzle back pressure.

3.7 The Inviscid Solution of the Cascade Problem

Figure (23) shows the distributions of Mach number against fraction of axial-chord, along both the suction and the pressure surface of a double-circular-arc

compressor cascade, predicted by the inviscid potential code CAS-IN. The geometry of the blade is as specified in Table (3) and it is assumed to be operating with an inlet air-flow Mach number and angle of 0.995 and 58.42^{o} respectively and an inlet total temperature and pressure of 288.15K and 101325.0 Pa respectively. A blockage factor, accounting for annulus boundary-layer and change in blade height from inlet to outlet, of 1.16 is assumed and the static pressure ratio across the blade is known to equal 1.242. The blade spacing is 56.43 mm and the stagger angle of the blades is 47.4^{o}. The fluid flowing through the cascade is assumed to be air with a ratio of specific-heads, γ, equal to 1.4 and a gas constant, R, equal to 288.7J/KgK.

The numerical solution scheme, CAS-IN, used to predict transonic flows in turbomachinery cascades is based on the inviscid potential scheme, 2D-IN used previously to predict two-dimensional transonic flows in nozzles. Thus the potential code, CAS-IN, is completely inviscid and ignores the effects of the growth in boundary-layer along the blade surfaces. As the compressor blade is part of a stationary cascade this code also ignores rotational effects.

The cascade blade row specified above has been experimentally investigated at the Von-Karman Institute of Fluid Dynamics [53], and the experimental distributions of Mach number obtained at the above operating conditions have been plotted onto Figure (23).

The flow inlet to the blade is initially subsonic as required by the solution procedure. The inviscid potential code, CAS-IN, predicts that, along the pressure-surface, the flow diffuses gently to a Mach number at the trailing-edge less than that at the leading edge. Along the suction surface, the flow is predicted as accelerating rapidly in the region of the leading-edge to a maximum value of Mach number of approximately 1.24.

Thence, the flow is predicted as decelerating rapidly to a Mach number of approximately 0.9, after which it decelerates gradually to the trailing edge of the blade. The rapid deceleration of the flow along the suction surface, at a fraction (x/c) of axial chord equal to approximately 0.38, represents the presence of a normal shock-wave at this point.

The values of Mach number, predicted by the CAS-IN code along the suction and pressure surfaces of the blade, are very nearly equal in the region close to the blade trailing-edge. Thus the Kutta condition, that the Mach numbers along these two surfaces are equal at the trailing edge, is satisfied. This Kutta condition was achieved by an iterative process whereby the outlet air-flow angle was varied until the two Mach-numbers at the trailing edge were equal. The outlet air-flow angle which satisfied this condition was found to equal 37.75^{o}.

The outlet air-flow angle determined by experiment is, in contrast, 43.79 degrees. Thus the inviscid potential code predicts that the flow is turned through an angle approximately 6^{o} greater than that which occurs in reality. The outlet air-flow angle predicted by the CAS-IN code is very close to the blade outlet angle, 37.5 degrees. Thus, it appears that the inviscid potential code predicts that the deviation of the flow is very nearly nill. The inability of the 2D-IN code to predict deviation is due to its neglect of the boundary-layer development on the blade surfaces and of the wakes which occur downstream of the blades. These viscous effects are largely responsible for the fluid experiencing, in practice, a deviation. Thus any model which ignores these effects cannot be expected to predict a deviation, and hence the correct value of outlet air-flow angle.

The CAS-IN potential code applied to the cascade blade-row operating under the conditions described previously predicts that the flow is turned by an angle of about 20^{o}, from inlet to outlet, accompanied by an overall deceleration of the flow. This deceleration of the flow is largely due to the change in flow area from inlet to outlet corresponding to the change in air-flow angle. The deceleration of the flow at outlet compared to that at inlet will result in a rise in static pressure from inlet to outlet, as given by the compressible form of the Bernoulli's equation. It is this rise in static pressure which a stationary compressor blade row is required to produce and a measure of the ratio of the losses incurred in achieving this rise to the value of the rise itself gives an indication of the efficiency of the compressor blade row.

The inviscid potential code has predicted Mach numbers on the suction surface as almost everywhere greater than the corresponding point on the pressure surface. Thus from the compressible form of the Bernoull's equation the static pressure along the pressure surface will be everywhere greater than the corresponding point on the suction surface. This pressure difference between the two surfaces of the blade will cause a force to be exerted on the blade, and this blade-loading will depend on the integral of the difference in pressure on suction and pressure surface along the blade.

The agreement between the Mach number distributions predicted by the inviscid potential-code, CAS-IN and those obtained by experiment is in general good. Some discrepancy does occur at the shock, with the CAS-IN code underpredicting the value of Mach number at the shock, on the suction surface, by approximately 6%. Also the deceleration predicted across the shock has been smeared by the potential code, compared to the experimental results.

The smearing of the shock has been noticed by many researchers and is a result of the inclusion of artificial-viscosity into the potential code [2]. Artificial viscosity is included into the potential code to provide stability to the numberical scheme and to enable the use of a simplified solution scheme but its inclusion does introduce an error into the final solution. The artificial viscosity acts in a manner similar to actual fluid viscosity and produces a smeared shock-wave of thickness greater than that which occurs in actual practice. This smearing is unavoidable and can only be reduced by reducing the artificial viscosity by, for example, refining the computational mesh. This will, however, reduce the stability of the numerical solution scheme and may lead to a divergence in the solution procedure. In practice it is necessary, therefore, to utilise an artificial viscosity which satisfies some compromise between accuracy and stability. Elsewhere on the suction surface, away from the vicinity of the shock-wave, the predictions of the inviscid potential code CAS-IN corresponds well to experimental observations.

Along the pressure surface of the blade, the CAS-IN code predicts Mach numbers which are very close to those suggested by experiment everywhere except in the immediate vicinity of the leading-edge of the blade. In this region the inviscid potential code predicts Mach numbers higher than those obtained by experiment. It is likely that this error is as a consequence of the blade not seeing exactly the correct angle of incidence at the leading-edge. It is known that a minor change in this angle can have significant effects on the Mach-number distributions at the leading edge, particularly on the pressure surface.

The error in the angle of incidence experienced by the blade is most likely caused by either a small error in the mathematical approximation of the blade geometry at the leading-edge or, alternatively, is

due to the effect of ignoring the boundary-layer in this region. The geometry of the blade is specified as a number of discrete points and in order to construct the computational grid it is necessary to fit curves through these points and to interpolate between them. As the blade is most highly curved at the leading-edge it is possible that the cubic-spline approximations used in this interpolation result in small errors in the specification of the location of the nodes on the blade surfaces and the gradients at these nodes. Thus an effective blade geometry is described which is slightly different, at the leading edge, from the actual blade which is being modelled. This difference in geometry at the leading edge will cause some error in the angle of incidence seen by the blade with possibly the consequential errors in the predictions of Mach-number in the region of the leading-edge, seen in Figure (23).

Alternatively, it may be that the effect of ignoring the growth of the boundary-layer on the blade surfaces is responsible for the errors in Mach-number distribtuions predicted near the leading edge by the CAS-IN code. This boundary-layer will effectively change the geometry of the blade with a resultant change in incidence angle. Although this change in blade geometry will be small due to the thinness of the boundary-layer near the leading edge, its effects may well be significant.

The vector plot of the velocities predicted by the CAS-IN potential code, within the blade row of the cascade specified in Table (3) and operating at the conditions specified previously, is given in Figure (24). From this vector plot it can be seen that the flow is smooth and follows the shape of the blade geometry. The velocities on the suction surface are everywhere greater than at the corresponding point on the pressure surface with the exception of the first node from the leading-edge. The velocity along the pressure surface is seen to rise

fairly rapidly in the immediate vicinity of the leading edge and then to fall equally as rapidly. This is due to the effect of incidence angle mentioned previously. The incidence angle experienced by the modelled blade is obviously smaller than that experienced in practice by the blade operating at the same conditions. Thus the flow on the pressure surface is predicted as accelerating around the leading edge.

3.8 The Viscous Solution of the Cascade Problem

Figure (25) shows the distributions of Mach-number against fraction of axial-chord, along both the suction and the pressure surface of the stationary cascade blade row specified previously, predicted by the viscous-corrected potential code CAS-VI. The operating conditions of the cascade are as before and the blockage factor is again taken as 1.16.

The numerical solution scheme, CAS-VI, used to predict viscous transonic flows in turbomachinery cascades is based on the viscous-corrected potential scheme, 2D-VI, used previously to predict two-dimensional, viscous, transonic flows in nozzles. The potential code CAS-VI computes the development of the boundary-layer on both the suction and pressure surface of the blade and imposes a distribution of transpiration velocity along each blade surface, which displaces the streamline along that surface by the distance of the boundary-layer displacement thickness on that surface. As in the CAS-IN code rotational effects are ignored as the cascade is assumed to be stationary. The experimentally obtained distributions of Mach-number obtained at the Von Karman Institute of Fluid Dynamics, for this cascade row at these conditions have also been plotted onto Figure (25).

The viscous potential code CAS-VI predicts that, along the pressure surface of the blade, the flow

diffuses gently to a Mach number at the trailing-edge less than that at the leading-edge. Along the suction-surface, the flow is predicted as accelerating rapidly in the region of the leading-edge to a maximum value of Mach number of approximately 1.29. Thence the flow is predicted as decelerating rapidly to a Mach number of about 0.92 after which it decelerates gradually to the trailing edge of the blade. The increase in predicted shock strength will result in an increase in the assumed total pressure loss, compared to the completely inviscid solution.

The value of exit air-flow angle at which the viscous potential-code satisfies the Kutta condition for the above blade operating at the above conditions is, as for the inviscid code, 37.75^{o}. The CAS-VI code applied to this blade thus predicts that the flow is turned through an angle of approximately 20^{o} from inlet to outlet, accompanied by an overall deceleration of the flow and a subsequent rise in static pressure. The values of Mach number predicted on the suction surface are everywhere greater than those predicted on the corresponding point on the pressure surface. Thus, a pressure difference is predicted as occuring between the two surfaces of the blade from which the lift on the blade may be calculated.

The agreemeent between the Mach number distributions predicted by the viscous-corrected potential code, CAS-VI, and those obtained by experiments is very good. As with the inviscid potential code the value of Mach number predicted as occuring immediately upstream of the shock, on the suction surface, is less than that observed by experiment. The error between the predicted and experimentally determined value of Mach number at this point is only 3%, however, one-half of the corresponding error of the inviscid code. The reason why the viscous potential code predicts a Mach number at the shock less than that occuring in reality is most likely due to an error in the estimation of the total pressure loss of the fluid due to the effect of boundary-layer. As will be discussed in a later section, the potential difference between

inlet and exit of the computational grid is varied iteratively until the static pressure at exit predicted by the solution is equal to the known value of static pressure at exit of the cascade row. Changing the value of potential difference between inlet and exit results in a change in the value of Mach number predicted at the shock. Thus the accuracy to which this Mach number is predicted is dependant on the accuracy to which the static pressure at exit is predicted. This value of static pressure depends on the value of total pressure at exit as well as the value of Mach number predicted at exit. The total pressure at exit is calculated as the total pressure at inlet minus losses in total pressure due to the shock-wave and due to the growth of the boundary-layer along the blade surfaces. The calculation of total pressure loss due to the shock is straightforward but the calculation of the loss due to the boundary-layer is more complicated. A fairly crude estimate has been made of this viscous caused loss (approximately 2% of the inlet value) and this will cause an error in the calculation of the static pressure at exit and thus an error in the value of potential difference set between inlet and outlet. It is likely that it is this error in the value of potential-difference set between inlet and outlet which is responsible for the underestimation of the value of Mach number at the shock predicted by the CAS-VI potential code.

In common with the inviscid solution the viscous-corrected solution predicts a shock on the suction-surface, signified by the rapid fall in velocity, which is significantly smeared compared to that occuring in reality. The cause of this smearing of the shock is the inclusion of the artificial viscosity terms into the solution which, as described in the previous section, acts in a manner similar to real viscosity causing a smearing of the shock.

Elsewhere on the suction surface, away from the immediate vicinity of the shock and along the entire length of the pressure surface the predictions of the CAS-VI potential code compare extremely well with experimental observations. The values of Mach number along the pressure surface predicted by the viscous-corrected CAS-VI code are slightly greater than those predicted by the inviscid CAS-IN code, resulting in the viscous code comparing more favourably to the experimental results than does the inviscid code. Similarly the viscous code predicts slightly higher Mach numbers, downstream of the shock along the suction-surface, than does the completely inviscid code, these higher values of Mach number again comparing more favourably with experiment.

The vector plot of the velocities predicted by the CAS-VI potential code, within the blade row of the cascade specified previously is given in Figure (26). From this vector plot it is apparent that, unlike the flow-field predicted by the inviscid potential code, the flow around the leading-edge of the blade is predicted as being smooth without any sharp acceleration around the leading-edge. It appears, therefore, that the inclusion of the boundary-layer effects has resulted in a change in the effective geometry of the blade near the leading-edge which has caused a change in the angle of incidence seen by the blade. The change in 'effective' blade-geometry, although most likely small, has had a significant effect on the predictions of Mach number around the leading edge.

The viscous-corrected code CAS-VI satisfies the Kutta condition for the same outlet air-flow angle as did the inviscid code CAS-IN. Thus, the CAS-VI code fails to predict deviation even though it takes into account the growth of boundary-layers on the blade surfaces. This inability to predict deviation must be due to either the limitations of the transpiration-type viscous correction or to the neglect of wakes downstream of

the blade. The transpiration type viscous correction simply alters the gradient of potential normal to the blade surface from a zero to a non-zero value. These non-zero values were set so that the streamline along the blade surface is displaced by one boundary-layer diplacement thickness. However, the core solution procedure remains inviscid, with the result that non-zero velocities are also predicted tangential to the blade surfaces. Also the potential core code does not predict a boundary-layer in which the velocities change from some relatively high value to zero along the blade surface. Instead an inviscid solution is predicted on what is essentially a modified blade geometry. It is possible that such a simplified viscous correction is unable to predict deviation.

More likely, the inability of the viscous-corrected potential code to predict deviation is due to its neglect of the wake mixing which occur, in reality, downstream of the blade row. These wakes are regions of relatively low-momentum fluid resulting from the separation of the boundary-layer at the blade trailing-edge. It is difficult to model wake mixing using a transpiration-type viscous correction. The boundary condition for the inviscid code, along the blade surfaces, was that the velocity normal to the blade surface was set (to zero). The viscous correction merely changed the value to which these velocities were set (to non-zero values). Downstream of the blades, however, the corresponding boundary condition expresses the periodicity of cascade flow, see section 2.5.2. The periodicity condition does not take a form which can easily be altered to include viscous effects. Thus the modelling of wake mixing is very difficult and has not been attempted in this report. The flow predicted downstream of the blades will, of course, be altered by the viscous correction occuring within the blade-row but, in the absence of a wake-mixing model, will not experience any deviation.

In the absence of a technique to model wakes, it is likely that the viscous-corrected potential code will be unable to predict deviation at exit from the blade row. Thus, whilst the introduction of a viscous correction has improved the predictions of Mach number distributions within the blade row, the effects of deviation remain ignored and the CAS-VI code (as does the CAS-IN code) predicts an incorrect exit flow angle.

For the test case of the cascade blade row specified in Table (3) operating at the conditions described previously, the viscous-corrected potential code CAS-VI has been found to give considerably improved predictions of the Mach-number distributions over the blade, compared to the inviscid potential code CAS-IN. In particular, the inclusion of viscous effects resulted in greatly improved predictions of the flow around the blade leading edge and of the shock strength. More modest improvements were obtained in the prediction of the flow on the suction surface downstream of the shock, and in the prediction of the flow along the pressure surface away from the leading-edge.

Thus, from this test case it is concluded that the viscous-corrected potential code CAS-VI gives improvements in the flow-field prediction of sufficient magnitude to strongly justify the use of this code in preference to the inviscid CAS-IN potential code. The preference given to the viscous-corrected code over the completely inviscid code is reinforced by the knowledge that the former requires only fractionally more computing time and storage compared to the latter.

3.9 Convergence of the Inviscid Solution of the Cascade Problem

In Figure (27) the residual of the completely inviscid solution of the cascade problem by the CAS-IN potential code has been plotted against the number of completed

iterations of the solution procedure. As in the solutions of nozzle-flow the residual used here is defined as the sum, over all nodes, of the change in velocity potential between that predicted at the previous and at the present iteration, divided by the local value of mesh spacing. Thus the magnitude of the residual gives an indication to the extent by which the solution changes from iteration to iteration, and can be used, therefore, as a monitor of convergence. Convergence was assumed to have occured when the value of this residual fell below 1200 (m/s). As the residual sums changes in potential divided by the local mesh spacing it actually is a sum of the change, from iteration to iteration, of the change not in velocity potential but in velocity itself. As approximately 1200 nodes were employed in the computational grid, a residual of 1200 (m/s) indicates that the average change in velocity from iteration to iteration is, on average, 1 m/s. Thus the average change in velocity is a mere 0.3%.

During the first ten iterations the residual falls very rapidly from an intial value of approximately 13,000 (m/s) to a value of approximately 3,000 (m/s). Thereafter, the residual decays much less rapidly and asymptotically approaches a near-zero value. A further sixty five iterations are necessary to reduce the residual from 3,000 (m/s) to a value below 1,200 (m/s).

The residual used here to monitor convergence is not that often used elsewhere in which the residual is the sum of the difference in the two sides of the governing flow equation when the computed potential distribution at a given iteration is inserted into the governing equations. The value of such a residual, at convergence, is usually very small (of order 10^{-5}), not the large values obtained using the alternative definition of residual (10^{3}).

3.10 Convergence of the Viscous Solution of the Cascade Problem

In Figure (28), the residual of the viscous-corrected solution of the cascade problem by the CAS-VI code has been plotted against the number of completed iterations. This residual is calculated, as described in the previous section, as the sum over all nodes of the change in the solution of velocity potential, from iteration to iteration, divided by the local value of mesh spacing. As for the inviscid cascade solution, convergence of the solution is assumed to have occured when the value of this residual falls below 1200 (m/s).

During the initial few iterations, the residual falls rapidly from an initial value of 13000 (m/s) approximately to around 3000 (m/s). The small rise in the value of the residual at the tenth iteration is due to the first alteration of the boundary conditions, made so as to include the effects of boundary-layer growth. Thereafter the residually falls gradually, approaching a near-zero value. Finally, after seventy-five iterations the residual falls below the pre-set value of 1200 (m/s) and the solution is assumed to be converged and is, therefore, terminated.

3.11 The Solution of the Cascade Flow Problem with Different Inlet Air-Flow Angles

In sections 3.7 to 3.8 it was shown that the viscous-corrected potential code CAS-VI gives more accurate predictions to the cascade flow problem than does the inviscid potential code CAS-IN. As this increased accuracy is obtained with very little extra cost in terms of computer storage requirements and running time it is recommended that the viscous CAS-VI code always be used in preference to the inviscid CAS-IN code.

In order to further validate the CAS-VI code it has been applied to the cascade specified previously operating at the same conditions described previously, with the exception of the inlet air-flow angle to the cascade and consequentially the static pressure ratio across the cascade. No experimental data was available for this cascade at other inlet air-flow angles and, therefore, no conclusions can be drawn as to the accuracy of CAS-VI code at these angles. However, it was felt to be of interest to determine qualitatively the effects predicted by this code as the inlet angle varies.

As will be discussed in a later section, the potential solution is non-unique and for the solution of transonic flows requires that the value of static pressure at exit from the cascade is known a priori. No information is known to this author on the variation of the static pressure rise, across the cascade considered in this report, with change in inlet air-flow angle. An estimation of this pressure rise at inlet angles other than 58.42 must, therefore, be made. A crude estimation has been made by assuming that the pressure rise varies approximately linearly with air-flow angle. This will result in errors in the predicitons by the CAS-VI code at angles other than 58.42, but this was not felt to be important as it is the qualitative effects of change in inlet air-flow angle which is of interest, in the absence of experimental data at these other angles. Thus, the static pressures at exit of the cascade are set in accordance with the values of pressure rise across the cascade given below:

Figure	Inlet Air Angle α_1	Pressure Rise $\Delta p/\frac{1}{2}\rho V_1^2$
29	56.42	0.2915
30	57.42	0.3192
31	58.42	0.3512 (known)
32	59.42	0.3763

Table 4

Figures (29), (30), (31) and (32) give the distributions of Mach number against fraction of axial chord predicted by the CAS-VI potential code, for the cascade specified previously operating with an inlet air-flow angle as given in Table 4.

Comparing Figures (29) to (32) it can be seen that the viscous-corrected potential code predicts that, as the inlet air-flow increases, the value of the Mach number at the shock also increased contributing to an increase in the lift on the blade. The value of Mach-number near the trailing-edge of the blade, however, is predicted as decreasing as the inlet air flow angle increases. Also of interest is the fact that, at lower values of inlet air-flow angle, the velocity on the pressure-surface near the leading-edge is higher than that at higher inlet angles. This effect is obviously due to the change in incidence angle seen by the blade with change in inlet air-flow angle. This observation agrees with the hypothesis that the cause for the overestimation of Mach-number, on the pressure surface near the leading edge, by the inviscid CAS-IN code is caused by the blade seeing an incorrect value of incidence angle.

The reduction in Mach-number at exit from the cascade with increase in inlet angle, predicted by the CAS-VI code, is as expected to occur in practice. An increase in inlet air-flow angle will result in a reduction in the outlet-to-inlet area ratio of the flow, A_2/A_1, as these areas are proportional to the cosine of the relevant air-flow angle. The flows at inlet and exit are both subsonic and, therefore from mass-continuity, the Mach-number at exit will fall with an increase in inlet angle, always provided the inlet Mach number remains constant. The predicted fall in Mach number at exit of the cascade contributes to the rise in exit static-pressure, with increase in inlet air-flow angle.

The viscous potential code, CAS-VI, predicts that the blade loading increases with increase in inlet air-flow angle, an effect which is expected from experimental observations of many other cascade blade rows. Thus this code predicts qualitatively at least, the correct response of the flow through a cascade to a change in the value of inlet air-flow angle.

3.12 Non-Uniqueness of the Potential Solution

It has been shown that the potential solution of transonic flows can result in more than one prediction of flow-field, for the same values of inlet and exit Mach number and angle. These multiple solutions usually vary most significantly from each other in their predicted values of Mach number at the shock and in the position of the shock itself. It is, therefore, necessary to have some means of establishing which of these multiple solutions corresponds to the actual physical flow which is being modelled. The non-uniqueness of the potential solution is due to its assumption of isentropy, which is invalid across the shock-wave. Thus it is necessary to establish which of the multiple solutions is the correct one by means of a non-isentropic exit variable. The isentropic potential flow model leads to a uniquely defined outlet state through the isentropic connection between inlet and outlet. Across a shock-wave, however, the flow is non-isentropic, the change in entropy being dependant on the strength of the shock. It is not, therefore, possible for a given inlet state to directly fix the shock position and strength by means of a physical outlet boundary parameter such as velocity density or pressure.

In the four potential codes described in this report, 2D-IN, 2D-VI, CAS-IN and CAS-VI, the strength and position of the shock wave was fixed by the specification of the difference in velocity potential between inlet and outlet. It was found that for any given potential difference,

between inlet and outlet, there exists a single unique potential solution for a fixed mass flow rate and inlet state. This potential solution will differ from others obtained, at the same mass-flow rate and inlet state, using a different value of potential difference between inlet and outlet.

The problem of determining which of a series of potential solutions corresponds to the actual physical flow being modelled is therefore, one of determining which value of inlet-to-exit potential difference corresponds to the physical flow being modelled. In the four potential codes described in this report this problem has been solved in an iterative manner. Initially a value of the potential difference between inlet and outlet was guessed and the potential flow-field corresponding to this potential-difference solved. The loss in total pressure across the shock, in this particular flow-field, is then estimated by means of the one-dimensional normal shock relationships which relate the loss in total pressure to the Mach number at the shock. Thence, by using the estimated (non-isentropic) value of total pressure at exit, the non-isentropic outlet static pressure corresponding to this guessed value of inlet-to-exit potential difference is calculated, a posteriori. This calculated value of the non-isentropic static pressure at exit is then compared to the actual value of static pressure existing at exit. If these two values of exit static pressure are equal then the guessed value of inlet-to-exit potential difference is the correct one, corresponding to the actual physical flow being modelled. If these two static pressures are unequal, however, the guessed value of potential-difference is altered and the above procedure repeated until the calculated non-isentropic static pressure at exit equals the known value which exists in practice.

The potential solution of transonic flows as described above requires that one of the non-isentropic exit paramaters, in this case the exit static pressure, be

known a priori. In general it is desirable, particularly for internal turbomachinery blade flows, that the numerical technique used to model flows through turbomachinery components can accurately predict the flow-field within these components without the need for specifying in advance any parameters at exit. The requirement that the static pressure at exit be known a priori is a major disadvantage of potential solutions and limits their application to components where this exit static pressure is either known or can be accurately estimated. For the prediction of flows within blade rows, the potential solution requires that the exit static pressure be estimated, in advance, either from experimental observations or by using cascade correlations.

For the solution of flows within convergent-divergent nozzles the potential code is a very useful tool as it is usual to prescribe, in advance, the static pressure to which the nozzle will be discharging. The iterative manner of the potential solution, in which the position and strength of the shock is altered (by altering the inlet-to-exit potential difference) until the exit static pressure corresponds to a known value, is very similar to the method used to solve for flows within these nozzles using a one-dimensional analytic method. In such an analytic method the flow is assumed isentropic up to the shock, which is initially guessed as occuring immediately downstream of the throat. Thus, from the isentropic one-dimensional flow relations, the flow up to the shock can be calculated analytically (without the need for any iterations). Thence from the normal one-dimensional shock relations the loss in total pressure across the shock can be calculated. Assuming the flow downstream of the shock to exit to be once more isentropic, the isentropic relations can again be used to determine the flow parameters everywhere in this region. The predicted value of exit static pressure is then compared to the prescribed value and if the two are unequal the position at which the shock is guessed is altered. The above procedure is then repeated until the predicted and prescribed values of exit static pressure are equal. Indeed, such a

solution procedure is not far removed from what actually occurs in practice. The flow within a nozzle, before it settles to its steady-state may well have a shock at a position different from its stready-state position. This will result in a difference in the exit static pressure and the discharge pressure which will send a pressure wave is an upstream direction through the nozzle. This pressure wave will cause the position of the shock to change until the exit static pressure equal the back pressure, at which point the pressure wave will die out. Thus it is felt that, although the requisite that the value of exit static pressure be known a priori is a major limitation of potential methods, at least the logic of the solution procedure is based on what happens in reality.

Figure	Predicted exit pressure ρexit (N/m^2)	error in back pressure ($\rho b - \rho exit)/\rho b$ (%)
29	67141.9	0.732
30	66962.9	0.250
31	66804.9	-0.170
32	66672.1	-0.534

Table 5

Figures (33) to (36) show the distributions of Mach number all predicted by the CAS-VI code applied to the cascade blade row specified previously; but with different values of potential difference between inlet and outlet. The values of exit static pressure predicted for these four cases are 67141.9, 66962.9, 66804.9 and 66672.1 Pa respectively. As the exit static pressure was known to be equal to 66870.3 Pa the errors in the prediction of exit static pressure $(P_{predict} - P_{given})/0.5 * \rho V_1^2$ are 0.732 %, 0.25%, -0.17% and -0.534% respectively. The error in predicted static pressure for the potential solution of Figure (35) was the only case within the acceptable limit of $\pm$ 0.18%, and the predicted flow field was taken as the one which corresponds to the actual physical flow-field.

Comparing Figures (33) to (36) it can be seen that changing the potential difference between inlet and exit does not result in a change in the value of Mach numbers predicted at inlet or exit from the blade row. However, changing this potential difference has resulted in a major change in the shock strength predicted by the potential soluiton. Thus the loss in total pressure estimated in these four solutions all vary significantly with a correspondant variation in the value of the static pressure predicted at exit from the cascade. It is by comparing this predicted static pressure at exit to the known value, that it is possible to establish which of the four potential solutions corresponds best to the actual physical flow-field which is being modelled.

Note that the flow-field predicted in Figure (36) gives Mach-numbers which are closer to those obtained by experiment than does the flow-field predicted in Figure (35). This is inspite of the latter predicting a value of exit static pressure which is closer to the known value, than does the former. This apparent anomaly is due to the errors associated with the estimation of the loss in total pressure between inlet and outlet, caused by the presence of the boundary layers on the blade surfaces and by the shock-wave. In particular the estimation of total pressure loss due to the effect of boundary layer is very crude. Also the estimation of total pressure loss across the shock is made assuming that the shock wave is normal and one-dimensional. This is not the case exactly in this cascade and so an error will arise in the estimation of total pressure, and thus static pressure, at exit of the cascade.

3.13 Stability of the Potential Code

The inviscid potential code 2D-IN was applied to the prediction of transonic flow through the nozzle specified previously, but with a change in either the number of nodes used in the computational grid or in the

operating conditions. It was found that an instability originates in the region of the shock when the absolute value of the gradient of velocity in the shock exceeds $1.x10^5 s^{-1}$. This instability was of sufficient severity to prevent convergence of the solution.

For constant operating conditions, reducing the size of the mesh spacing of the computational grid results in improved numerical accuracy of the solution, as the finite-differencing errors are also reduced. However, a reduction in mesh spacing is also accompanied by an increase in the magnitude of apparent velocity gradient across the shock. The gradient of velocity across the shock is, theoretically, infinite as at the shock there is a discontinuity in velocity. However, due to the inclusion of artificial-viscosity into the solution scheme the true step change in velocity is predicted as being smeared over a couple of mesh spacings. The increase in velocity gradient with reduction in mesh spacing is the result of the solution predicting an increasingly sharper shock jump, as the mesh spacing is reduced. It was found that there is a limit to which the mesh spacing can be reduced, below which instabilities in the solution become critical. The absolute value of gradient of velocity across the shock, at this limiting mesh size, was found to be approximately $1x10^5$.

Alternatively, if the mesh spacing is kept fixed and the back pressure of the nozzle reduced, then the potential solution responds so as to predict, as expected, an increase in shock strength. This increase in velocity at the shock is accompanied by an increase in the absolute value of velocity gradient across the shock. For a fixed mesh spacing, it was found that there exists a limit of back pressure, below which the potential solution diverges. The absolute value of the gradient of velocity across the shock corresponding to this limiting value of back pressure was found, as before, to be approximately $1.x10^5 s^{-1}$.

Thus, for stability of the present potential solution, it is required that:

$$\left(\frac{\Delta v}{\Delta x}\right)_{\substack{\text{absolute} \\ \text{max.}}} < 1. \times 10^5 \ (s^{-1}) \qquad (107)$$

The units of velocity gradient are second^{-1}, so equation (107) is of the following form:

$$\frac{1}{\Delta t} < 1. \times 10^5$$

where Δt is some length of time

so, for stability of the potential solution, it is required that:

$$\Delta t < 1. \times 10^{-5} \qquad (108)$$

The solution of the steady state potential equation of transonic flow is constrained by the requirement that some pseudo-time-step, Δt, is less than 10 microseconds. As an alternative to the solution of transonic flows by the steady-state flow equations, it is possible to 'march' the transient flow equations forward in time until a steady-state is achieved. The existence of a maximum limit of the step in time, in which the solution can be marched forward in one iteration of these 'time-marching' techniques is well known and has been well documented [54]. Thus the stability requirement of the steady-state potential solution of transonic flows is very similar in form to that existing for the time-marched solutions. Both types of solution require that, for stability, some time-step Δt is less than a certain value.

The limit in the magnitude of the time-step utilized in time-marched techniques is given by the Courant-Friedrich-Lewi (CFL) condition. This condition specifies that the time step, Δt, from one iteration to the next

must not be so large that a disturbance originating at any node is allowed to reach neighbouring nodes with a single time-step. The CFL condition may, therefore, be expressed as:

$$\Delta t < \frac{\Delta x}{v + c} \tag{109}$$

where, for the region of the computational grid under consideration, Δx is the size of the mesh spacing and v is the velocity. The potential solutions, discussed earlier in this seciton, were obtained with a mesh spacing of typically 2mm in the region of the shock and an axial velocity at the shock of approximately 400 m/s. Thus the CFL condition requires that the time-step, Δt, used in the time-marching techniques is such that:

$$\Delta t < \frac{2. \times 10^{-3}}{400 \times 350}$$

i.e:

$$\Delta t < 2.5 \times 10^{-6} \text{ (s)} \tag{110}$$

The maximum limit of time step of the time-marched solutions as required for stability is given by the CFL criteria to be approximately 2.5 microseconds. Thus the limit of the actual time-step for the transient time-marched solution of transonic flow is a factor of 4 times smaller than that which apparently exits for the pseudo-time-step of the steady-state solution. This may explain why the transient time-marched techniques require, in general, a factor of 4 or more times as many iterations to achieve convergence as do the steady-state techniques.

The steady-state potential equation used to model transonic flows, in this report, is:

$$(\rho b \phi_x)_x + (\rho b \phi_y)_y = 0 \qquad (23)$$

Across the shock, the gradient in the y-direction will be much smaller than those in the x-direction. Thus, for the purpose of a stability analysis, we may ignore all gradients in the y-direction. Ignoring these gradients in the y-direction, the potential equation (23) may be expressed as:

$$(\rho b)\phi_{xx} + (\rho b)_x \phi_x = 0 \qquad (111)$$

from which the following exression for velocity gradient may be derived

$$\frac{\partial v}{\partial x} = \phi_{xx} = - \frac{(\rho b)_x \phi_x}{\rho b} \qquad (112)$$

From equation (107), we require that for stability of the steady-state potential solution of transonic flow, that:

$$\left(\frac{\partial v}{\partial x}\right)_{\text{shock}} > - 1. \times 10^5 \qquad (113)$$

The gradient of velocity is negative across the shock, as velocity falls across a shock-wave.

Substituting for the expression of velocity gradient from equation (112) into equation (113), the condition for stability becomes:

$$- \frac{(\rho b)_x \phi_x}{\rho b} > -1. \times 10^5$$

or:

$$\frac{(\rho b)_x}{(\rho b)} < \frac{1. \times 10^5}{v} \qquad (114)$$

Equation (114) may also be expressed as:

$$\frac{\partial}{\partial x} \{ \ln (\rho b) \} < \frac{1. \times 10^5}{v} \qquad (115)$$

The velocity, v, at the shock, for the potential solutions discussed in this section is appproximately 400m/s. Thus the criteria for stability, equation (107), requiring that the absolute gradient of velocity at the shock is less than 100000 (s^{-1}) is equivalent to stating that gradient with respect to axial distance (x) of the natural log of the product of density and blockage factor, at the shock, must be less than 250 i.e.:-

$$\frac{\partial}{\partial x} \{ \ln (\rho b) \} < 250 \qquad (116)$$

The discussions on stability above have centred on limiting values of certain gradient across the shock-wave. To be strictly correct, it is required that the maximum values of these gradients in the entire flow-field should be less than the corresponding limiting value, for stability. For transonic flows however, the maximum gradients of velocity and density almost always occur at the shock, and it is sufficient to monitor only these gradients in this region.

The relationship between the natural log of any function, in this case (ρb) the product of fluid density and blockage factor, and the function is as shown in Figure (37). From Figure (37), it can be seen that at low values of the product of density and blockage (ρb), a small change in magnitude of (ρb) will be accompanied by a large change in the magnitude of $\ln_e(\rho b)$. Thus it appears that the steady-state potential solution will exceed the stability requirement of equation (11) and fail to converge when the value of the product of density and

blockage becomes small. This limits the operating conditions of nozzles or cascades at which the potential solution can give meaningful results to those which result in the minimum value of density in the flow field remaining relatively high. From Figure (37) it can be seen that below a density of 0.1 kg/m^3, a small change in density will result in a large change in the natural log of density, which will probably result in the potential solution diverging. The Mach number corresponding to this value of density is approximately 2.85 which is outside the range of flows which may be usefully modelled by potential methods.

Figures (38) and (39) show the distributions of (ρb) and $ln_e\ (\rho b)$ respectively predicted by the 2D-IN potential code for a convergent-divergent transonic nozzle. The operating conditions of the nozzle and the mesh spacing of the computational grid were chosen such that the solution was at its limit of stability. Thus, for example, any further reduction in mesh spacing would have resulted in the solution becoming unstable. It can be seen from Figure (38) that the minimum value of density predicted in the flow-field occurs at the shock where the density is approximately 0.5 kg/m^3. Thus the gradient of $ln_e\ (\rho b)$ across the shock will be approximately double the value of gradient of (ρb) across the shock.

For this particular flow field the density has not fallen so low as to practically make convergence of the solution impossible. However, across the shock the density rises rapidly due to the rapid rise in static pressure across the shock. The gradient of (ρb) and $ln_e\ (\rho b)$ in this region will, therefore, be high. Figures (40) and (41) show the distributions of $(\rho b)x$ and $\{ln(\rho b)\}x$ predicted by the inviscid 2D-IN potential code for the nozzle operating at the conditions and with the mesh spacing, as mentioned above. It can be seen that the maximum value of the gradient of (ρb) across the shock is approximately 150, whilst that of the gradient of $ln_e(\rho b)$ is approximately 300. As expected, the latter gradient is about twice the magnitude of the former corresponding to a density of 0.5kg/m^3. As this solution was obtained at the limit of stability it seems that the

stability criteria of equation (116) is unnecessarily strict and should be modified to:

$$\frac{\partial}{\partial x} \{\ln (\rho b)\} < 300 \qquad (117)$$

The limiting value of the gradient of the natural log of the product of density and blockage has been found, from Figure (39), to be 300. This differs slightly from the limiting value of 250 derived previously, equation (116). The difference between the two limiting values is due to the neglect of the gradients in the y-direction, in the derivation of equation (116). Thus it is recommended that the limiting value of the gradient of the natural log of the product of density and blockage be taken as 300.

The steady-state potential solution will remain stable provided that the maximum gradient of the natural log of the product of density and blockage remains below about 300. For the range of operating conditions at which transonic nozzles and turbomachinery blade row operate in practice, the steady-state potential solution remains stable provided the mesh spacing in the region of the shock is not made excesively fine. For very fine meshes, the solution attempts to predict very sharp changes in the flow properties across the shock with the result that the stability criteria (equation(12)), is violated with a consequential divergence of the solution. For components in which the density becomes very low it seems likely that the potential solution will be unable to converge, even with coarse computationl grids.

The above stability requirements have been derived with reference to the inviscid potential code 2D-IN used to predict transonic flows in nozzles. However, as the solution procedure of the viscous corrected potential code 2D-VI, and those of the cascade codes CAS-IN and CAS-VI are very similar to that of the 2D-IN code, then the stability requirement derived in this section relates equally as well to all four potential codes.

3.14 Accuracy of the Potential Solution

The numerical error associated with approximating a partial derivative of velocity potential by the nine-node central-difference scheme (equation 28) is, in general, a function of the products of the fourth order partial derivatives of potential and the mesh spacing. Thus, assuming that the mesh spacing in the x-direction, Δx, is equal to that in the y-direction, Δy, then:

$$\text{Numerical Error} = L_1(\phi_{xxxx}\Delta x^4, \phi_{xxxy}\Delta x^4, \phi_{xxyy}\Delta x^4, \phi_{xyyy}\Delta x^4, \phi_{yyyy}\Delta x^4)$$

If however, this partial derivative is approximated using the six-node upwind-difference scheme, the numerical error is also a function of the products of the third order partial derivatives of potential and the cube of the mesh spacing. The numerical error of the upwind-difference scheme is of a lower order than that of the central-difference scheme. This is because, with only six nodes in the finite-difference lattice, three of the partial derivatives of potential of third order or less (equation 59) cannot be set to zero. These partial derivatives are chosen to be of third order and thus contribute third order terms to the numerical error of the upwind-difference scheme. As the mesh spacing is small these third order products are much larger than the fourth order products, and these latter products can be ignored. Thus the numerical error of the upwind-difference scheme is:

$$\text{Numerical Error} = L_2(\phi_{xxx}\Delta x^3, \phi_{yyy}\Delta x^3, \phi_{xyy}\Delta x^3) \qquad (118)$$

In regions of supersonic flow, partial derivatives of potential, instead of being approximated by an upwind difference, have been approximated by a central difference plus some additional terms. These additional terms are called artificial viscosity and are equal to the numerical error of the upwind-difference scheme, equation (29).

Thus, whether parital derivatives are approximated by upwind-differences or central-differences plus artificial viscosity, the numerical error of the approximation will contain third order partial derivatives of potential. This numerical error is, from equation (55), also a function of the mesh spacing, Δx, of the computational grid. Thus, by comparing different predictions obtained on computational grids of different mesh spacings, and by analysing the form of the numerical error, a quantitative estimate of the numerical error of the potential code can be made.

Figure (42) shows the distributions of axial velocity, along the nozzle-wall and centre-line, predicted by the inviscid 2D-IN potential code applied to the nozzle specified in Table (2). The inlet total temperature and pressure were 293.15k and 93428.0 pa respectively and the back pressure was 79040.06 pa. Again the fluid was assumed to be air with a ratio of specific heats of 1.4 and a gas constant of 288.7 kj/kgk. The computational grid used had an average mesh spacing 4.0mm and the grid was such that the spacing in the x-direction was equal to that in the y-direction. Figure (43) shows the distributions of axial velocity, along the nozzle-wall and centre-line, predicted by the 2D-IN code applied to the identical nozzle operating at the identical conditions, but derived using a different computational grid. The mesh spacing of the computational grid used in the predictions of Figure (43) was, on average, 2.0mm. Thus the latter set of these predictions was obtained using a computational grid twice as fine as that used to obtain the former set of predictions.

The two sets of predictions compare very well Figure (44) and (45). The closeness of these two sets of predictions is very encouraging as it suggests that the numerical error of the CAS-IN potential code is low. The largest discrepancies between the two sets of predictions

occur in the predicted velocity along the wall at x=38mm and in the predicted velocity along the centre-line at the shock.

The CAS-IN code, with the coarse grid predicts an axial velocity along the centre-line, at the shock, equal to 383.4m/s. The same code used with the fine grid predicts an axial velocity at this point, however, equal to 393.5m/s. Thus the percentage difference in the predicted value of axial velocity at the shock along the centre-line is 2.5%.

In regions of supersonic flow the major contribution to the numerical error of the potential solution is due to the inclusion of aritifical viscosity (A.V.), necessary if regions of such flow are to be represented by ellpitic equations. From the expression for A.V., equation (55), it can be seen that the artificial viscosity at any node is a function of both the poperties of the fluid and of the computational grid. Thus, A.V. is a function of the following fluid properties:

$$a, \rho, u, v, U_{xx}, U_{yy}, v_{yy}$$

and the following properties of the computational grid:

$$\Delta x^3, \Delta y^3, D_n, E_n \text{ and } F_n$$

where:

- a is the local speed of sound
- ρ is the local density of the fluid
- u is the local component of velocity in the x-direction
- v is the local component of velocity in the y-direction
- Δx is the mesh spacing in the x-direction
- Δy is the mesh spacing in the y-direction

D_n, E_n and F_n, where n=1 to 6, are the sets of coefficients used in the approximation of the partial derivatives of ϕ_{xx}, ϕ_{xy} and ϕ_{yy} respectively

Assuming that the mesh spacing Δx is equal to that Δy, the artifical viscosity is a function of the following properties of the computational grid:

$$\Delta x^3, D_n, E_n \text{ and } F_n$$

The three sets of coefficients D_n, E_n and F_n are the coefficients used to approximate the second order derivatives of potential and are, therefore, approximately proportional to the inverse of the square of the mesh spacing.

i.e. :-
$$D_n \alpha 1/\Delta x^2$$
$$E_n \alpha 1/\Delta x^2$$
$$F_n \alpha 1/\Delta x^2$$

From equation (55), the artificial viscosity is equal to a function of the sum of these coefficients (from n=1 to 6) multiplied by the cube of the mesh spacing. Thus A.V. is a function of the mesh spacing Δx.

i.e. $\text{A.V.} = f_1(\Delta x)$

A.V. is, as mentioned previously, also a function of the fluid properties, thus:

$$\text{A.V.} = f_2(a, \rho, u, v, U_{xx}, U_{yy}, v_{yy}, \Delta x) \qquad (119)$$

From equations (15) and (24), the local speed of sound and density are function of the fluid velocities u and v only. Thus, equation (119) may be simplified to:

$$\text{A.V.} = f_3(u, v, U_{xx}, U_{yy}, v_{yy}, \Delta x) \qquad (120)$$

It can be seen from Figures (40) and (41), that the distributions of u and v along the nozzle, predicted by the 2D-IN code, do not vary much with mesh spacing, except across the shock itself. Thus, it can be assumed that the components of velocity and their derivatives are independent of the mesh spacing of the computational grid. Thus equation (120) can be simplified to:

$$A.V. = k\Delta x \tag{121}$$

where k is a constant

Thus, the artificial viscostiy introduced into the solution scheme is proportional to the mesh spacing and will increase if the mesh spacing is increased. However, the central-difference approximation to the potential flow equation contains the terms An,Bn,Dn and Fn (n=1 to 9) utilised to approximate the partial derivatives $\phi_x, \phi_y, \phi_{xx}$ and ϕ_{yy} respectively. These terms also vary with the mesh spacing and therefore the coefficient of the unknown velocity potential, in the governing potential flow equation, will also vary with mesh spacing. The conservative form of the potential equation can be expressed as:

$$(\rho b)_x \phi_x + (\rho b)_y \phi_y + \rho b \left(\phi_{xx} + \phi_{yy} \right) = 0 \tag{122}$$

In regions of supersonic flow the left hand side of this equation is approximated using central-differences and an artificial viscosity term is included into the right-hand side. Thus, for supersonic flow, equation (122) is represented as:

$$\{ (\rho b)_x \phi_x + (\rho b)_y \phi_y + \rho b \left(\phi_{xx} + \phi_{yy} \right) \}_{C.D.} = A.V. \tag{123}$$

Using the central-difference approximations of equation (28) to approximate the partial derivatives of equation (123), reduces this equation to:

$$(\rho b)_x \{\Sigma A_n \phi_n - \phi_o \Sigma A_n\} + (\rho b)_y \{\Sigma B_n \phi_n - \phi_o \Sigma B_n\}$$

$$+ \rho b\{\Sigma D_n \phi_n + \Sigma F_n \phi_n - \phi_o \Sigma D_n + \Sigma F_n\} = A.V. \qquad (124)$$

where: ϕ_o is the value of the unknown velocity potential

ϕ_n is the value of velocity potential at neighbouring nodes,

for n=1 to 9

Σ is a summation from n=1 to n=9

A_n, B_n, D_n and F_n are the terms, equivalent to the general C_n of equation (28), used to approximate, by central differences, partial derivatives of ϕ_x, ϕ_y ϕ_{xx} and ϕ_{yy} respectively.

The coefficient (CFO) ofthe unknown velocity potential in equation (124) can be expressed as:

$$CFO = (\rho b)_x \Sigma A_n + (\rho b)_y \Sigma B_n + \rho b (\Sigma D_n + \Sigma F_n) \qquad (125)$$

The density and blockage terms in equation (124) remain approximately constant as the mesh spacing is changed, except in the region corresponding to the shock jump. The terms A_n, B_n, D_n and F_n, however, vary according to the following:

For the approximation of first order gradients:

$A_n \alpha\ 1/\Delta x$
$B_n \alpha\ 1/\Delta x$

and for the approximation of second order derivatives:

$D_n \alpha\ 1/\Delta x^2$
$F_n \alpha\ 1/\Delta x^2$

Thus the coefficient (CFO) of the unknown velocity potential, ϕ_o, in equation (124) may be approximated as:

$$CFO = \frac{C1}{\Delta x} + \frac{C2}{\Delta x^2} \qquad (126)$$

where C1 and C2 are constants related to the local density and blockage.

The mesh spacing, Δx, is very small (between 2×10^{-3} and 4×10^{-3}).

Thus equation (126) may be approximated as:

$$CFO = \frac{C2}{\Delta x^2} \tag{127}$$

The coefficient of the unknown velocity potential of the discretized flow equation (124) is, therefore, inversely proportional to the square of the mesh spacing and decreases as the mesh spacing is increased. The artificial viscosity, however, is approximately proportional to the mesh spacing. Thus the percentage of numerical error introduced into the solution by the inclusion of artificial viscosity is proportional to the cube of the mesh spacing. Thus:

$$\text{Numerical Error} \quad \alpha \ \Delta x^3 \tag{128}$$

This numerical error is the error due to the inclusion of artificial viscosity into the solution procedure and will disappear in the immaginary case when there are an infinite number of nodes with a mesh spacing equal to zero. This error is identical to the error introduced by approximating partial derivatives by upwind rather than central differences.

The maximum numerical error (NEF) associated with using the fine computational grid, where the average mesh spacing is 2mm, is:

$$NEF = K_1 \Delta x_f^3 \tag{129}$$

where k_1 is some constant

The maximum numerical error (NEC) associated with using the coarse computational grid, where the average mesh spacing is 4 mm, is:

$$NEC = k_1 (2\Delta x_f)^3 \qquad (130)$$

Δx_f is the mesh spacing, upstream of the shock, of the fine grid.

The mesh spacing at an identical point on the coarse grid is approximately twice this value and is, therefore, represented by $2\Delta x_f$.

The difference in the numerical errors of the coarse and fine grids has been found to be a maximum of 2.5%, thus:

$$NEC - NEF = 2.5 \qquad (131)$$

Substituting the above expressions for NEC and NEF into equation (131):

$$8k_1 \Delta x_f{}^3 - k_1 x \Delta x_f{}^3 = 2.5$$

$$k_1 = \frac{2.5}{7\Delta x_f} \qquad (132)$$

Now substituting this expression for the constant k_1 into the equations (129) and (130) allows the maximum numerical error of the 2D-IN code, when applied with the two different computational grids discussed in this section, to be determined:

For the fine grid:

$$\text{Numerical Error (NEF)} = \frac{2.5}{7\Delta x_f{}^3} \times \Delta x_f{}^3 = 0.36\%$$

and for the coarse grid

$$\text{Numerical Error (NEC)} = \frac{2.5}{7\Delta x_f{}^3} \times (2\Delta x_f)^3 = 2.86\%$$

The computational grid used to generate the predictions of Figures (9) to (20) had an average mesh spacing of 2.59mm.

The mesh spacing of such a grid is $1.295\Delta x_f$ and the associated value of the maximum numerical error is:

$$\text{Numerical Error} = \frac{2.5}{7\Delta x_{f^3}} x(1.29\Delta x_f)^3 = 0.78\%$$

The numerical error of the 2D-IN inviscid potential code is proportional to the cube of the mesh spacing. A compromise between accuracy and the number of nodes in the computational grid must be made. Many nodes will result in a small error due to the associated small value of mesh spacing, but will be expensive in terms of requried computer storage and running time. Using a computational grid of average mesh spacing of 4mm results in a maximum numerical error of 2.86%. Reducing this mesh spacing to 2.59mm results in a numerical error of 0.78 %, whilst reducing the mesh spacing further to 2mm reduces the maximum numerical error to a mere 0.36%. Reducing the mesh spacing below an average of 2.5mm therefore has little effects on the numerical error of the solution scheme. In most cases, in this report, a computational grid of average mesh spacing equal to 2.59mm was used with the 2D-IN potential code, giving very low numerical error of 0.78%.

The preceding estimates of numerical accuracy have been derived with reference to the inviscid potential code 2D-IN used to predict transonic flows in nozzles. However, as the solution procedure of the viscous corrected nozzle code 2D-VI and those of the cascade potential codes are very similar to that of the 2D-IN code, the above analysis may be assumed to be representative of all four codes. The average mesh spacing used in the computational grid for the cascade solution was about 3.5mm and the numerical error of this solution was, therefore, approximately 1.91%. This is felt to be an acceptable value for numerical error.

Numerical error is due to errors in the finite-difference approximations, which are dependent on the computational grid utilized. It is not the total error of the model compared to the actual physical flow. This total error is a sum of the numerical error, the error due to computer round-off and the error due to any simplifying assumptions. This total error can only be estimated by comparing theoretical predictions to experimental data and will, in general, be greater than the numerical error.

4 CONCLUSIONS AND RECOMENDATIONS FOR FURTHER WORK

4.1 Conclusions Regarding the Nozzle-Flow Models

Potential flow models have been developed to simulate transonic flows in convergent-divergent nozzles. These models may be either inviscid (as the 2D-IN code) or may have a viscous correction to model the effects of boundary-layer development along the solid walls (as does the 2D-VI code). Both the viscous and the inviscid model solve the flow in two-dimensions. These potential flow models always predict a unique solution of the flow-field provided that the nozzle back pressure is satisfied. Both the inviscid and the viscous-corrected potential models were compared to the corresponding models developed by Damia-Torres [52], and were found to compare very well. The inclusion of the viscous effects due to boundary-layer development was found to have the effect of forcing the shock, near the wall, upstream and reducing the Mach number at the shock.

These models were shown to react correctly to a change in nozzle back pressure: They predicted that increasing the back pressure forces the shock towards the nozzle-throat with a corresponding reduction in Mach number at the shock.

The solution of the potential flow converged rapidly, in less than 100 iterations. The solution procedure remains stable provided that the (absolute) gradient of velocity predicted as occuring across the shock is less than $1.x10^5$. This limits the average size of the mesh spacing of the computational grid to a minimum of 1.9mm. It is recommended that an average mesh spacing of about 2.6mm be employed, which results in a maximum numerical error, at the shock, of 0.78%.

The potential solution assumes that the flow is irrotational and isentropic which limits the use of these codes to cases in which the Mach-number at the shock is less than 1.4 - 1.5.

4.2 Conclusions Regarding the Cascade Flow Solution

Potential flow models have been developed to simulate transonic flows in cascade blade rows. Both an inviscid (CAS-IN) model and one which has a viscous correction to model the effects of boundary-layer development on the blade surfaces have been developed. These codes solve the flow-field, within stationary cascade blade-rows, in two dimensions. The potential assumption that the flow is irrotational and isentropic limit the application of these codes to cases in which the Mach-number at the shock is less than about 1.4.

In order to be able to predict a unique flow-field these potential models require that the static pressure, at exit of the cascade blade-row, be known a priori. This is a serious disadvantage of potential-flow models when used to simulate transonic flows in cascade, and limits their use to cases where this static pressure is known or can be obtained from correlations. Provided that the static pressure at exit is known a priori, however, the potential codes predict a unique flow-field.

The predictions of Mach-number distribution obtained with both the CAS-IN and the CAS-VI codes have been compared to those obtained experimentally. The viscous corrected (CAS-VI) code, in particular, predicts Mach-number distributions on the blade surfaces which are very similar to those observed by experiment. The only discrepancy between the theoretically and experimentally obtained distribution of Mach-number occurs across the shock. The change in fluid properties across the shock is observed experimentally as being very sudden, almost a step change. In the theoretical predictions, however,

this change has been smeared over a few column spacings. The smearing of the shock-jump is due to the inclusion of artificial viscosity into the solution and can only be reduced by reducing the mesh spacing of the computational grid.

The viscous-corrected potential code (CAS-VI) has also been applied to the cascade operating over a range of inlet air-flow angles. This code predicts that the Mach-number at the shock (on the suction-surface) increases and the Mach-number near the trailing-edge decreases, as the inlet air-flow angle increases. The overall effect, predicted by the CAS_VI code, is that the blade loading increases with increase in air-flow angle at inlet.

The viscous-corrected code (CAS-VI) has been seen to give significant improvements in the prediction of the flow-field compared to the inviscid code (CAS-IN). These improvements have been achieved with very little penalty in required computer running-time and storage and it is recommended that the CAS-VI code be always used in preference to the CAS-IN code.

4.3 Recommendations for Further Work

The viscous-corrected potential codes 2D-VI and CAS-VI have been used in this report to simulate transonic flows in convergent-divergent nozzles and in axial turbomachinery blade-rows, respectively. These codes have given flow-field predictions which compare well with other theoretical models or with experimental data, at least for the test cases considered in this report. However, each of these codes has only been applied to a single geometry. Further comparisons of their predictions with experimental observation, for other geometries, must be made before their use can be recommended without reservation. In particular, the 2D-VI code has only been compared against other theoretical models. The

flow-field predictions of this code need to be compared against experimental data, therefore, so that the accuracy of this code may be ascertained.

Viscous effects have been included into the 2D-VI and the CAS-VI potential codes by allowing a transpiration flow through solid walls. The amount of this transpiration flow is a function of the gradient of the boundary-layer displacement thickness and it is, therefore, first necessary to compute the distribution of the boundary-layer displacement thickness along the relevant solid surface. The method used, in this report, to compute this distribution is a simple one-dimensional boundary-layer model, which does not allow, for example, separation and reattachment of the boundary-layer. In convergent-divergent nozzles and in cascade blade rows the influence of the boundary-layer is very marked and the solution of the flow is highly dependant on the accuracy to which the boundary-layer has been computed. It is felt that there is a need to improve this boundary-layer calculation, by using a more sophisticated model to solve in two-dimensions. It is desirable that this improved model can predict boundary-layer separation and reattachment. Also, the correlation used to model the influence of the shock /boundary-layer interaction is very crude. It is felt that, as the boundary-layer displacement-thickness distribution is so sensitive to this interaction, that an improved representation of this interaction will lead to significantly improved results. This may be achieved by the use of either an improved correlation or by actually modelling the interaction itself.

The other improvement which can be made to these potential models is to extend their solution from two-dimensions into full three-dimensions. In the search for improved efficiency of turbomachinery components their designers are increasingly becoming interested in the three-dimensional flow through these machines, in both

stationary and rotating components. The potential solution is a very efficient solution and it is not thought that such a solution in three-dimensions would be prohibitively demanding in terms of computer run-time. It would however require much greater computer memory than would a similar solution in only two-dimensions. Apart from the possible limitations due to computer memory requirements, there does not appear to be any difficulty in extending the potential solution into three dimensions. This is in contrast to a stream-function solution which, although similar in many ways to a potential solution, does not exist in three-dimensions.

Finally it is felt that, particularly if the potential solution is to be extended into three-dimensions, it would be beneficial to include the effects of rotation into the solution. This can be achieved by a fairly minor modification of the governing flow-equation and of the boundary-conditions along the surfaces of the turbomachinery blades [22] . A great deal of information can be obtained on the behaviour of a rotating blade-row from a knowledge of its behaviour in a stationary cascade. However, particularly near the tip, it is desirable to have a complete knowledge of the flow under rotating conditions. Such a knowledge can then be used to reduce effects such as over-tip leakage and thus improve aerodynamic efficiency.

References:

1. Magnus, R
   Yoshihara, H.
   "Inviscid Transonic Flow over Aerofoils." AlAA paper No. 70-47 (1970).

2. Murman, E.M.
   Cole, J.D.
   "Calculation of Plane Steady Transonic Flows." AlAA Journal Vol. 9, No.1, ppll4-121 (1971).

3. Garabedien, P.R.
   Korn, D.G.
   "Analysis of Transonic Airfoils" Communications on Pure and Applied Mathematics, Vol.24, pp841-851 (1971).

4. Shamroth, S.J.
   Gibeling, H.J.
   McDonald, H.
   "A Navier-Stokes solution for Laminar and Turbulent Flow Through a Cascade of Airfoils." AlAA Paper No.80-1426 (1980).

5. Shamroth, S.J.
   McDonald, H.
   Briley, W.R.
   "Application of Navier-Stokes Analysis to Transonic Cascade Flow-Fields." ASME Paper 82-GT-117 (1982).

6. Briley, W.R.
   McDonald, H.
   "Solution of the Multidmensional Compressible Navier-Stokes Equations by a Generalized Implicit Method." J. Comp. Physics, Vol. 24, No.4 August 1977. p.372.

7. Douglas, J.
   Gunn, J.E.
   "A General Formulation of Alternating Direction Methods." Numensche Math, Vol.6, 1964, pp428-453

8. Denton, J.D. "An Improved Time-Marching Method for Turbomachinery Flow Calculation." ASME Paper 82-GT-239 (1982).

9. Denton, J.D. "A Method of Calculating Fully Three Dimensional Inviscid Flow Through any type of Turbomachine Blade Row." Short Course on Advanced Flow Calculations for Internal Flow and Turbomachinery." Given at the Cranfield Institute of Technology. Presented by the Fluid Engineering Unit of C.I.T., 12-14 April (1983).

10. Singh, U.K. "A Computation and Comparison with Measurements of Transonic Flow in an Axial Compressor Stage with shock and Boundary-Layer Interaction. "ASME Paper 81-Gr/GT-S (1981).

11. Couston, M. "Time Marching Finite Area Method" VKI-LS-84, 1976, Von Karman Inst. for Fluid Mechanics (1976).

12. Gopalkrishnan, S. Bozzola, R. "A numerical Technique for the Calculation of Transonic Flows in Turbomachinery Cascades." ASME Paper 71-GT-42 (1971).

13. Steger, J.L. Pulliam, T.H. Chima., R.V. "An Implicit Finite Difference Code for Inviscid and Viscous Cascade Flow." AlAA Paper 80-1427 (1980).

14. Schmidt, W.
Jameson, A.
"Euler Solvers as an Analysis, Tool for Aircraft Aerodynamics." Advances in Computational Transonics, 4th Vol., Ed. Habashi, W.G. Pineridge Press (1980).

15. Rizzetta, D.P.
Borland, G.J.
"Unsteady Transonic Flow over Wings Including Inviscid/Viscous Interaction." AlAA Journal, Vol. 21, No. 3, March (1983).

16. McDonald, P.W.
"The computation of Transonic Flow through Two-Dimensional Gas Turbine Cascades." ASME Paper 71-GT-8 (1971).

17. Veuillot, J.P.
"Calcui Numerique de l'ecoulement transsonique d'un Fluide parfait dans une gille d'aubes." No. 1975 La Recherche Aerospatiole, pp327-338.

18. Chen, Lee-Tzong.
"Improved Finite-Difference Scheme for Transonic Airfoil Flowfield Calculations." AlAA Journal, Vol. 20, No.2, (1981).

19. McCarthy, D.R.
Reyhner, T.A.
"Multigrid Code for Three-Dimensional Transonic Potential Flow about Inlets." AlAA Journal. Vol.20, Nol.1, January (1982).

20. Jameson, A.
"Transonic Potential Flow Calculations using Potential Form." AlAA 2nd comput. Fluid Dynamics Conf., pp 148-161 (1975).

21. Sobieczky, H.
Dulikravich, D.S.
"A Computational Design Method for Transonic Turbomachinery Cascades." ASME paper 82-GT-117 (1982).

22. Deconick, H
Hirsch, C.
"Finite Element Methods for Transonic Blade-to-Blade Calculation in Turbomachines." ASME paper 81-GT-5 (1981).

23. Holst, T.L.
"An Implicit Algorithm for the Conservative Transonic Full-Potential Equation using an Arbitary Mesh." AlAA paper 78-113, July (1978).

24. Deconick, H.
"The Numerical Computation of Transonic Potential Flows." Ph.D Thesis, Vrije Universiteit Brussel (1983).

25. Ives, D.C.
Luitermoza, J.F.
"Second Order Accurate Calculation of Transonic Flow over Turbomahcinery Cascades." AlAA paper 78-1149 (1978).

26. Salas, M.D.
"Foundations for the Numerical Solution of the Euler Equations" Advances in Computational Transonics, 4th Vol, pp 343-369, Ed. Habashi, W.G. Pineridge Press (1983).

27. Holst, T.L.
"An Implicit Algorithm for the Transonic Full-Potential Equation in Conservative Form." Computing method in Applied Sciences and Eng. R. Glowinski and J. Lions (eds), North Holland Publishing Co. (1980).

28. Jameson, A.
"Iterative Solutions of Transonic Flows over Airfoils and Wings, Including Flows at Mach 1" Comm. Pure Appl. Maths, Vol. 27, pp 283-309, (1974).

29. Dulikravich, G.S. "Common Misconceptions in the Calculation of Transonic Full Potential Flows." ASME paper 84-GT-211 (1981).

30. Deconick, H.
Hirsch, C. "Boundary Conditions for the Potential Equation in Transonic Internal Flow Calculation." ASME paper 83-GT-135 (1983).

31. Thwaites, B. "Approximate Calculation of the Laminary Boundary Layer." Aeornaut. Q.1., pp 245-280. (1949).

32. Rangaswamy, C.
Elder, R. "Description of a Computer Programme for the Potential Flow and Boundary Layer Calculations around Cascades." SME note No.6, Internal Publication, S.M.E. Cranfield, I.T. (1975).

33. Von Karman, T. "Uber Lamunare and Turbulents Rubing." 2AMM1, pp233-252 (1921).

34. Dunham, J. Unpublished notes from N.G.T.E.

35. Schlichting, H. "Boundary-Layer Theory, Translated by J. Kesten McGraw-Hill, New York, 6th ed. (1968).

36. Maskell, E.C. "Approximate calculation of the turbulent boundary layer on two dimensional uncompressible flow" A.R.C. 11-654, (1951).

37. Head, M.R. "Entrainment in the turbulent boundary layer" A.R.C. R&M 3152 (1958).

38. Green, J.E. "Application of Heads entrainment method to the prediction of turbulent boundary layers and wakes in compressible flow" ARC 34052, R&M 3788, TR72079 (1972).

39. Cebeci, T. Bradshaw, P. "Momentum Transfer in Boundary Layers." McGraw-Hill/Hemisphere, Washington, D.C. (1977).

40. Thompson, B.G.J. "The Calculation of Shape Parameter Development in Incompressible Turbulent Boundary Layers with or without Transpiration", AGARD 97, 159-190 (1965).

41. Adamson, T.C. Messiter, A.F. "Analysis of two-dimensional Interactions between shock Waves and Boundary Layers," Ann. Rev. Fluid Mech. 12, p 103 (1980).

42. Lock, R.C. "A Review of Methods for Predicting Viscous Effects on Aerofoils and Wings at Transonic Speeds" R.A.E., Techn Memo. Aero 1860. (1980).

43. Green, J.E. "A discussion of the vicous/inviscid Interactions at Transonic speeds," R.A.E. Tech. Rep. 72050 (1972).

44. Bauer, F. Garabedian, P.R. "Computer Simulation of Shock Wave Boundary Layer Interaction," Comm. Pure Appl. Mat. 26 p659 (1973).

45. Bavitz, P.C. "An analysis method for two-dimensional transonic viscous flows" NASA TN D-7718 (1975).

46. Collyer, M.R.
Lock, R.C.
"Prediction of viscous effect in steady transonic flow past an aerofoil" Aero. Qu., 30, p485 (1979).

47. Melnik, R.E.
"Recent developments in a boundary layer theory for computing viscous flows over airfoils. Paper presented at VSAF/FRG Data Exchange Meeting Meersberb (1979).

48. Nandanan and Stanewsky, E.
"Airfoil Flow with a special solution for Shock/Boundary Layer Interaction", AlAA Journal Vol. 19, No. 12. pp1540-1546 (1980).

49. Raghunathan, S.
McAdam, R.J.W.
"Boundary Layer and Turbulence Intensity Measurements in a shock Wave/Boundary Layer Interaction" AlAA Journal, Vol.21, No. 9, pp1349-1350, (1983).

50. Kooi, J.W.
"Influence of Free Stream Mach Number on Transonic shock wave Boundary Layer Interaction", National Aerospace Laboratory MP78013, (1978).

51. Heritage, Jane.
"A New Method for Separated Boundary Layers", Internal Publication, BHRA Fluid Engineering Unit (1984).

52. Damia-Torres, J.A.
"Time-Marching Solutions of Transonic Duct Flow", Ph.D Thesis, University of London, Imperial College of Science and Technology, Mechanical Engineering Dept. (1980).

53. Meauze, G.
Starken, H.

"Turbine and Compressor Cascade Test Cases, Part II-Compressor Cascades," L.S.84, Transonic Flows in Axial Turbomachinery Von Karman Institute for Fluid Dynamics (1976).

54. Roache, P.J.

"Computational Fluid Dynamic." Albuguerge, New Mexico Hormosa Publishers (1972).

TABLES

Axial dist. from throat x (mm)	Height of Nozzle wall above centre-line y (mm)
105.62	37.25
105.00	37.25
102.50	37.25
100.00	37.25
97.50	37.25
95.00	37.25
92.50	37.25
90.00	37.25
87.50	37.25
85.00	37.25
82.50	37.25
80.23	37.25
78.71	37.22
76.16	37.12
73.63	36.84
71.09	36.33
68.55	35.57
66.01	34.53
63.48	33.13
60.94	31.36
58.40	29.02
55.86	26.96
53.32	24.76
50.78	22.67
48.24	21.25
45.70	20.11
43.16	19.17
40.62	18.33
38.09	17.65
35.55	17.01
33.01	16.43
30.47	16.00
27.93	15.61
25.39	15.31
22.85	15.10
20.31	14.90
17.77	14.78
15.23	14.68
12.70	14.60
10.16	14.52
7.62	14.47
5.08	14.45
2.54	14.42
0.00	14.42

Table 2a:- Nozzle Geometry-Convergent Section

Axial dist. from throat x(mm)	Height of Nozzle wall above centre-line y(mm)
2.54	14.47
5.08	14.58
7.62	14.77
10.16	14.99
12.70	15.28
15.23	15.64
17.77	16.02
20.31	16.43
22.85	16.88
25.39	17.34
27.93	17.80
30.47	18.28
33.01	18.76
35.55	19.19
38.09	19.60
40.62	20.01
43.16	20.41
45.70	20.77
48.24	21.10
50.78	21.40
53.32	21.71
55.86	22.01
58.40	22.27
60.94	22.52
63.48	22.75
66.01	22.98
68.55	23.18
71.09	23.38
73.63	23.56
76.17	23.74
78.71	23.92
81.25	24.07
83.79	24.20
86.33	24.30
88.87	24.40
91.40	24.48
93.94	24.53
96.48	24.58
99.02	24.63
101.56	24.68
104.10	24.70
106.64	24.73
108.39	24.76
111.00	24.76
113.50	24.76
116.00	24.76
118.50	24.76
121.00	24.76
121.08	24.76

Table 2b:- Nozzle Geometry-Divergent Section

x (mm)	y (mm)
0.00000	0.00000
0.08005	-0.14004
0.27287	-0.18209
0.58402	-0.17518
1.01830	-0.16560
1.57439	-0.15348
2.25061	-0.13895
3.04490	-0.12217
3.95490	-0.10334
4.97786	-0.08226
6.11076	-0.06036
7.35025	-0.03671
8.69267	-0.01195
10.13412	0.01363
11.67042	0.03976
13.29716	0.06614
15.00969	0.09248
16.80315	0.11850
18.67252	0.14392
20.61258	0.16845
22.61795	0.19183
24.68314	0.21382
26.80247	0.23417
28.97023	0.25267
31.18056	0.26912
33.42752	0.28335
35.70512	0.29520
38.00729	0.30455
40.32793	0.31129
42.66090	0.31537
45.00000	0.31674

Table 3a:- Cascade Geometry for zero-stagger
- Pressure Surface

x (mm)	y (mm)
47.33920	0.31537
49.67216	0.31129
51.99281	0.30455
54.29498	0.29520
56.57257	0.28335
58.81953	0.26912
61.02986	0.25267
63.19762	0.23417
65.31696	0.21382
67.38213	0.19183
69.38750	0.16845
71.32756	0.14392
73.19693	0.11850
74.99039	0.09248
76.70293	0.06614
78.32965	0.03976
79.86594	0.01363
81.30739	-0.01195
82.64981	-0.03671
83.88930	-0.06036
85.02219	-0.08266
86.04514	-0.10334
86.95514	-0.12217
87.74942	-0.13895
88.42563	-0.15348
88.98172	-0.16560
89.41599	-0.17518
89.72713	-0.18209
89.91995	-0.14003
90.00000	0.00000

Table 3a(contd.) -Cascade Geometry at zero-stagger
-Pressure Surface

x (mm)	y (mm)
0.00000	0.00000
0.04331	0.15533
0.22019	0.24325
0.52409	0.31205
0.94852	0.40733
1.49244	0.52802
2.15452	0.67281
2.93312	0.84011
3.82632	1.02809
4.83190	1.23468
5.94734	1.45763
7.16982	1.69449
8.49623	1.94266
9.92319	2.19942
11.44699	2.46197
13.06357	2.72742
14.76898	2.99287
16.55840	3.25540
18.42717	3.51215
20.37024	3.76030
22.38234	3.99712
24.45798	4.22004
26.59145	4.42660
28.77684	4.61454
31.00809	4.78180
33.27892	4.92556
35.58296	5.04722
37.91373	5.14246
40.26462	5.21125
42.62897	5.25283
45.00000	5.26574

Table 3b:- Cascade Geometry at zero stagger
- Suction Surface

x (mm)	y (mm)
47.37114	5.25283
49.73549	5.21125
52.08636	5.14246
54.41714	5.04721
56.72119	4.92655
58.99202	4.73179
61.22325	4.61453
63.40865	4.42659
65.54211	4.22003
67.61775	3.99711
69.62985	3.76028
71.57291	3.51214
73.44167	3.25539
75.23111	2.99285
76.93640	2.72741
78.55309	2.46196
80.07689	2.19941
81.50383	1.94264
82.83025	1.69447
84.05272	1.45762
85.16815	1.23467
86.17372	1.02808
87.06693	0.84010
87.84550	0.67280
88.50758	0.52801
89.05150	0.40732
89.47591	0.31205
89.77982	0.24324
89.95668	0.15532
90.00000	0.00000

Table 3b (contd.) - Cascade Geometry at zero-stagger
- Suction Surface

Inlet Mach Number	= 0.995
Inlet Air Angle	= 58.42°
Static Pressure Ratio	= 1.242
Blockage	= 1.16
Chord	= 90 mm
Stagger	= 47.4°
Pitch	= 56.43
Aspect Ratio	= 1.878

Table 3c:- Cascade Operating Conditions

FIGURES

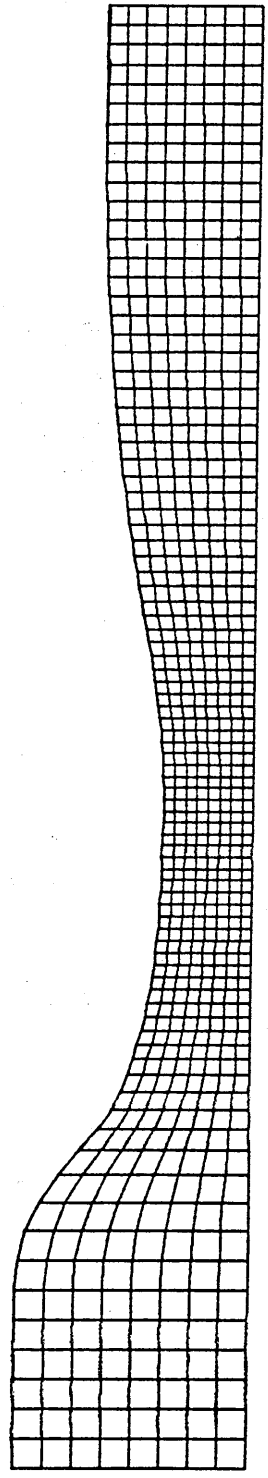

FIGURE 1. The Computational Grid for the Solution of the Nozzle

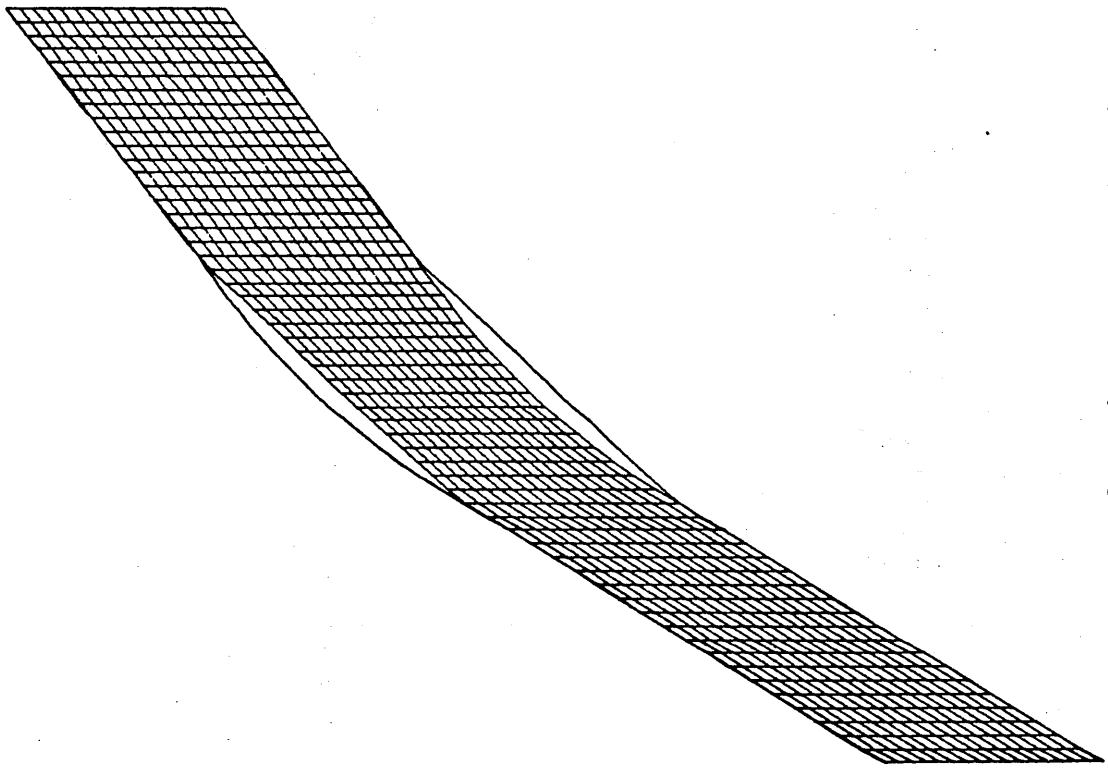

FIGURE 2. The Computational Grid for the Solution of the Cascade Problem

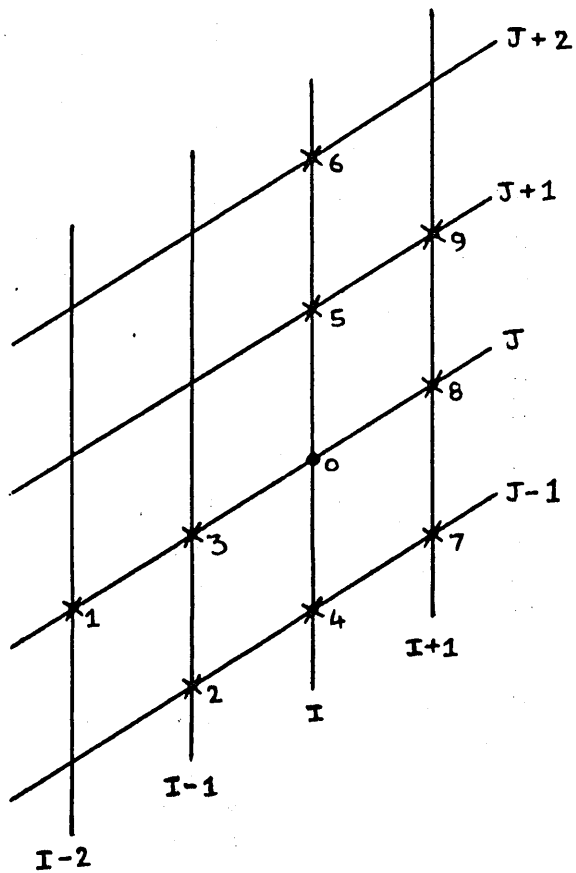

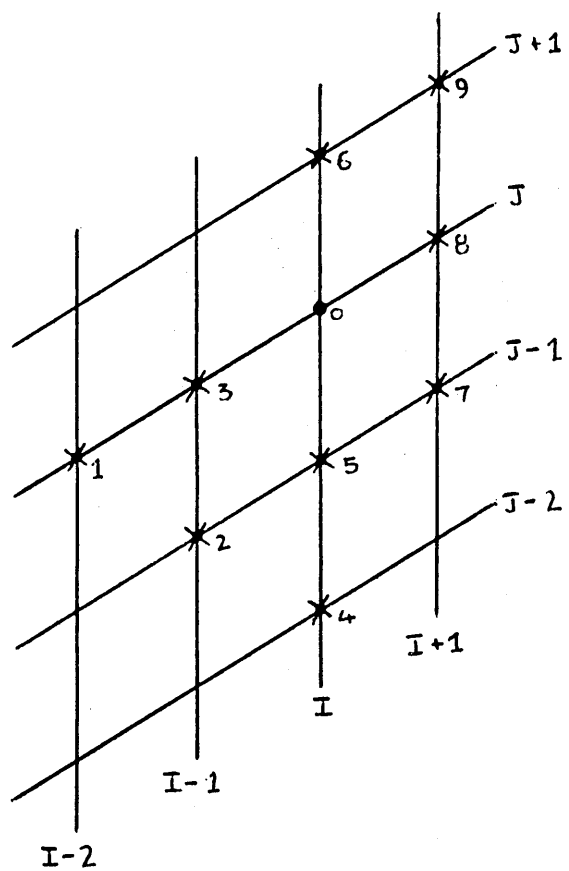

FIGURES 3 & 4. The Central Finite Difference Lattice for Reference Nodes in the lower and upper halves of the Computational grid respectively

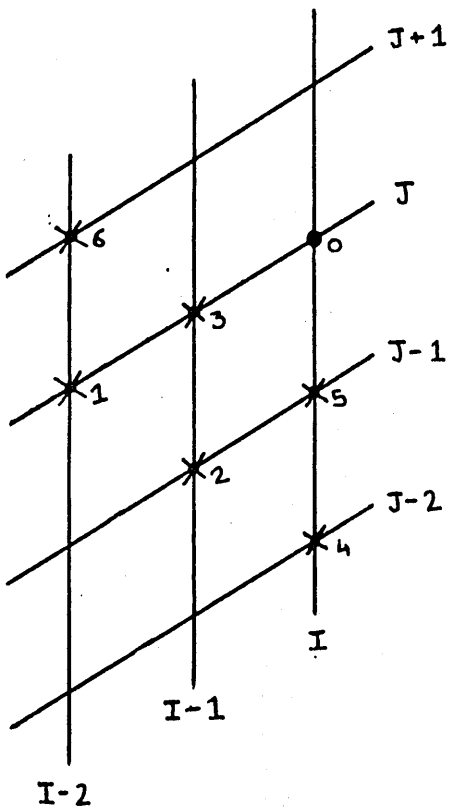

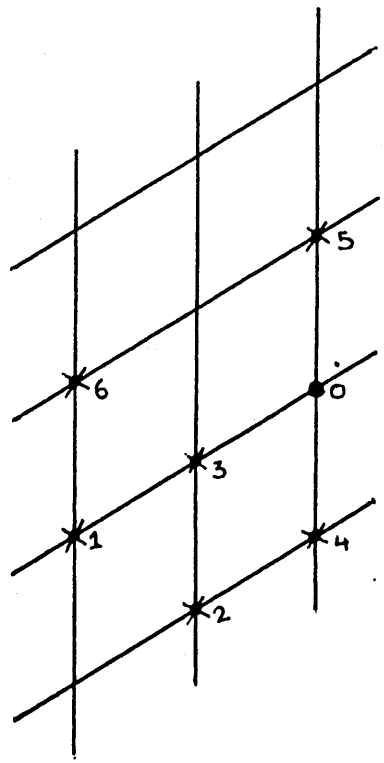

FIGURES 5 & 6. The Upwind Finite Difference Lattice for Reference Nodes above and on, respectively, the second row of Nodes of the Computational Grid

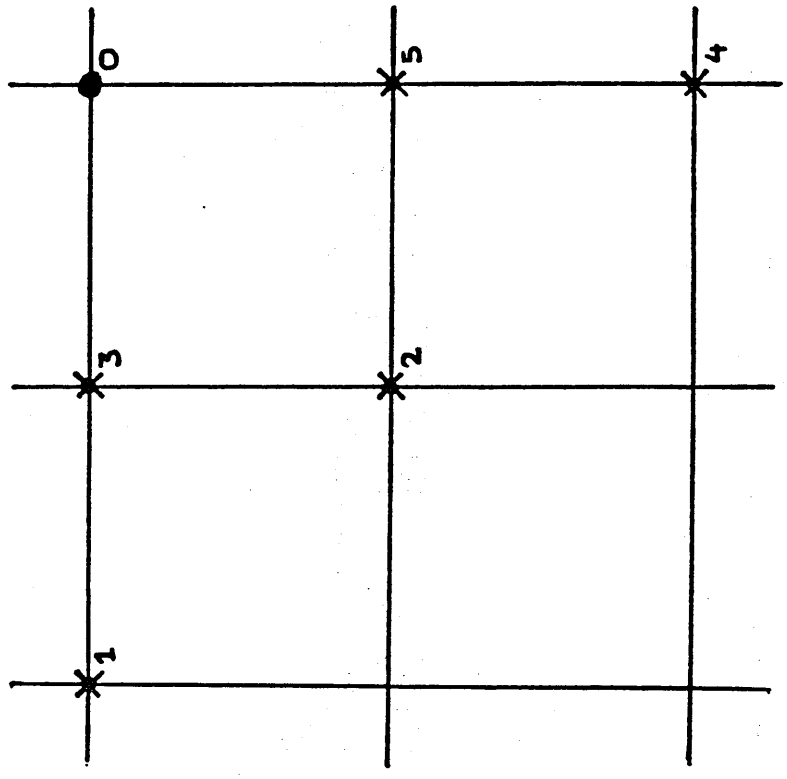

FIGURE 7. The Five Node Upwind Difference Lattice for a Square Computational grid

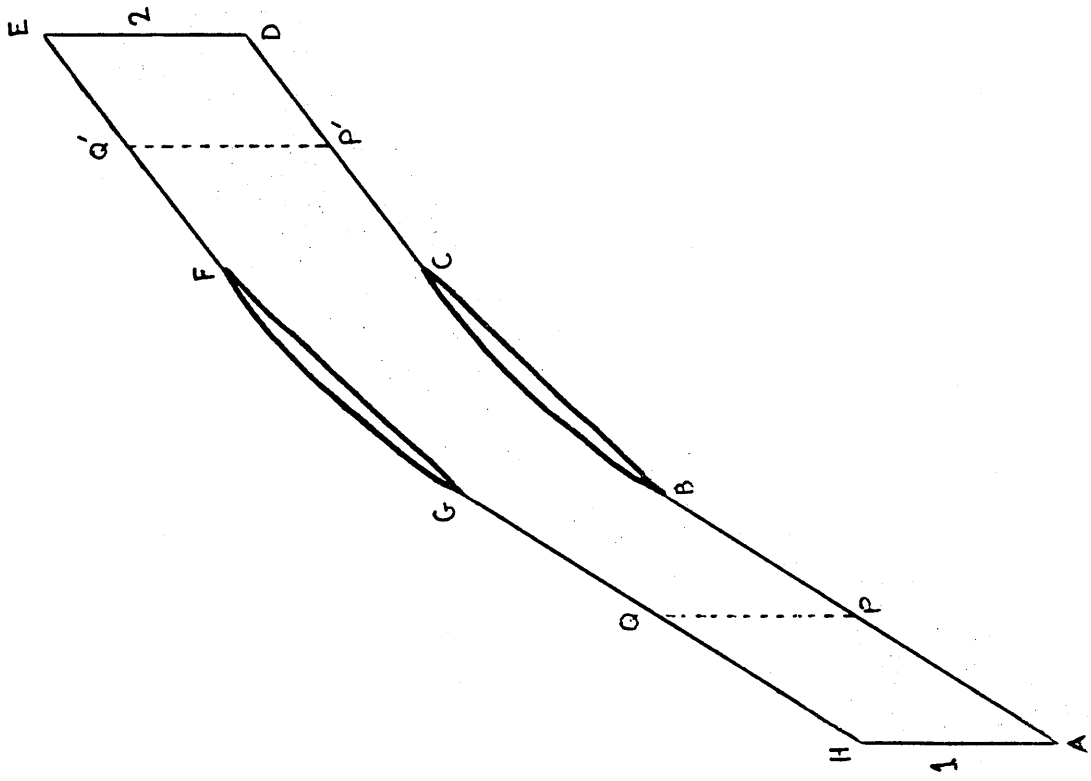

FIGURE 8. Boundary Conditions for the Cascade Blade Row

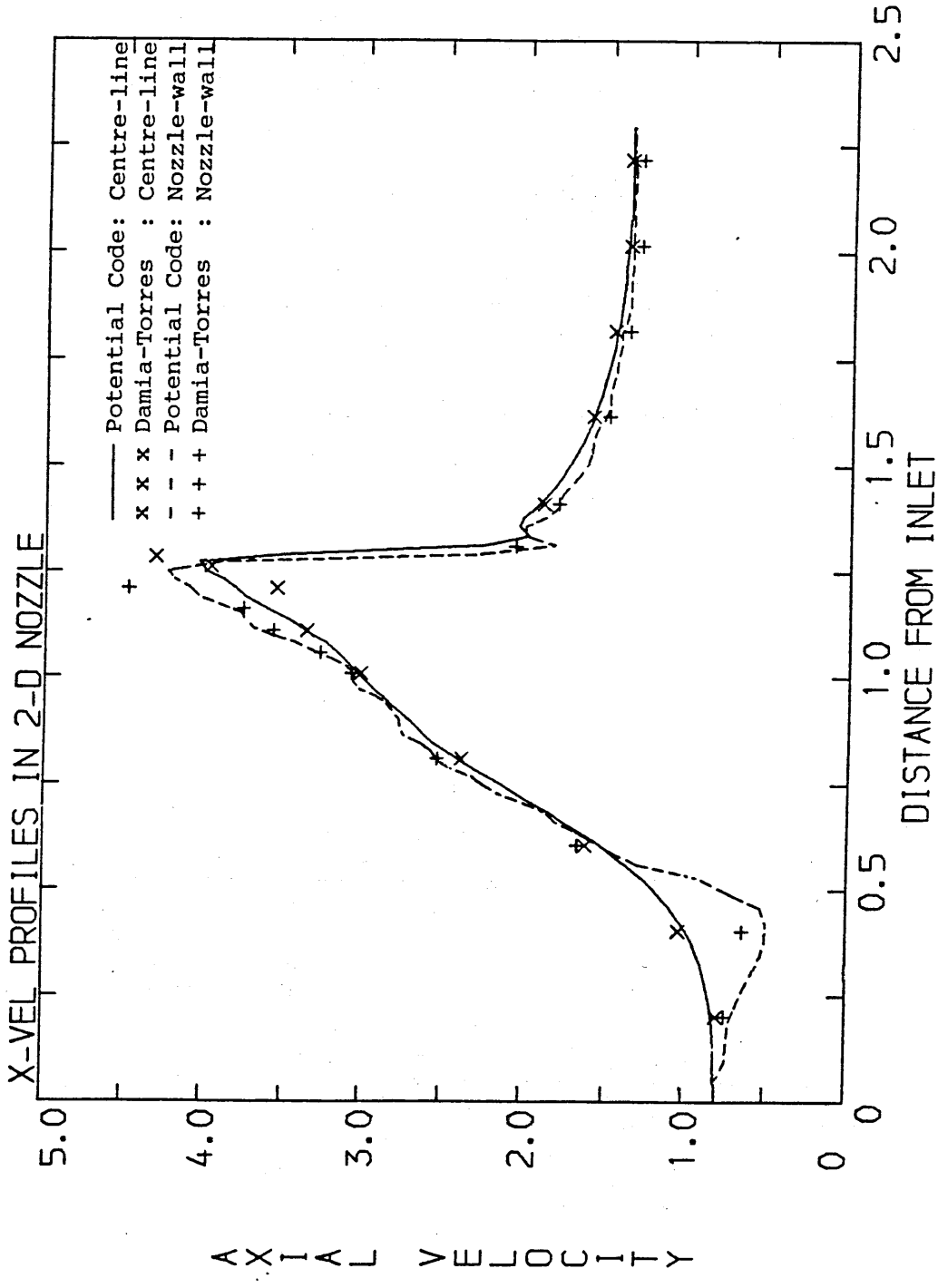

FIGURE 9. Distributions of Axial Velocity along the Nozzle, predicted by the 2D-IN Potential Code

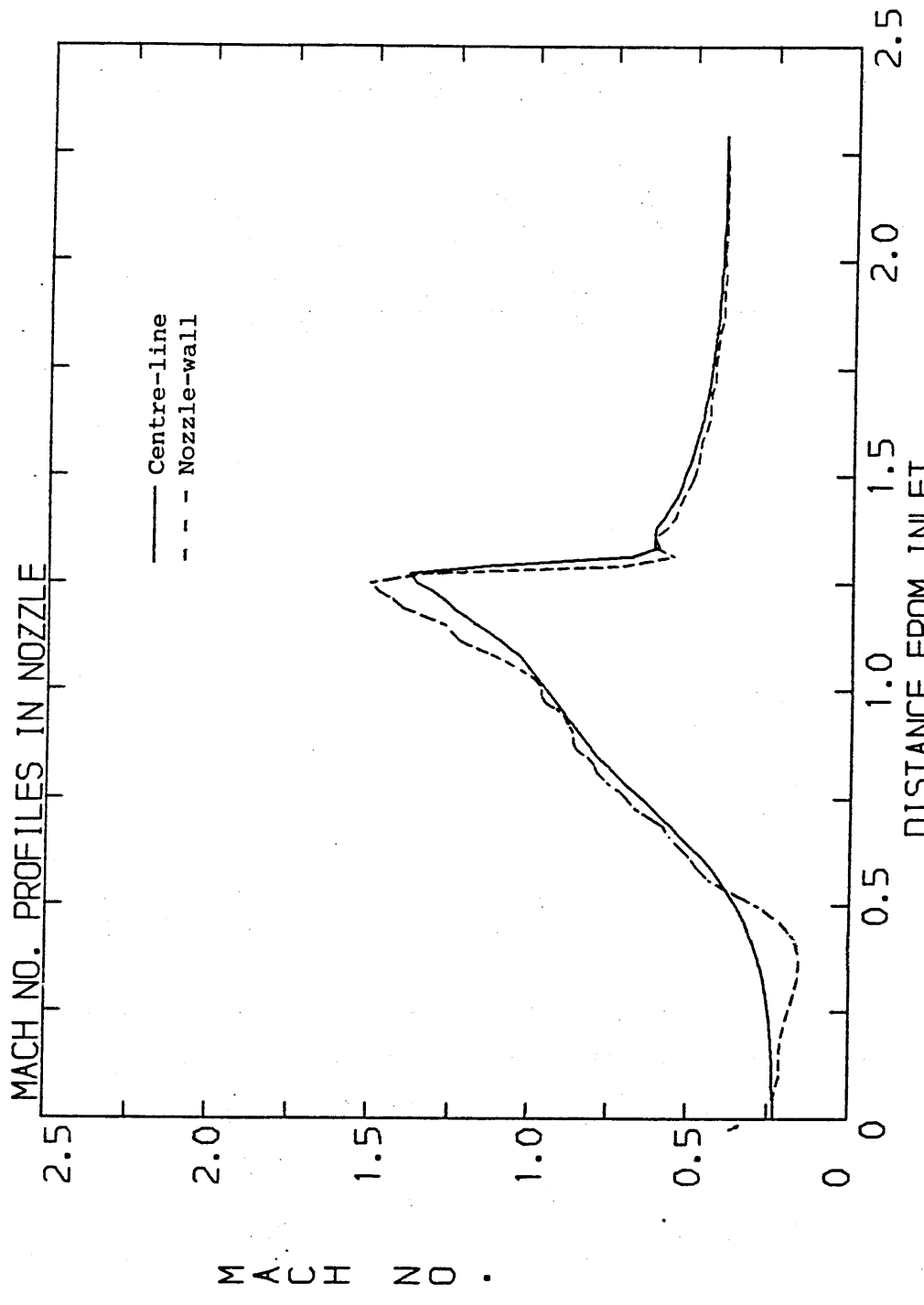

FIGURE 10. Distributions of Axial Mach Number along the Nozzle, predicted by the 2D-IN Potential Code

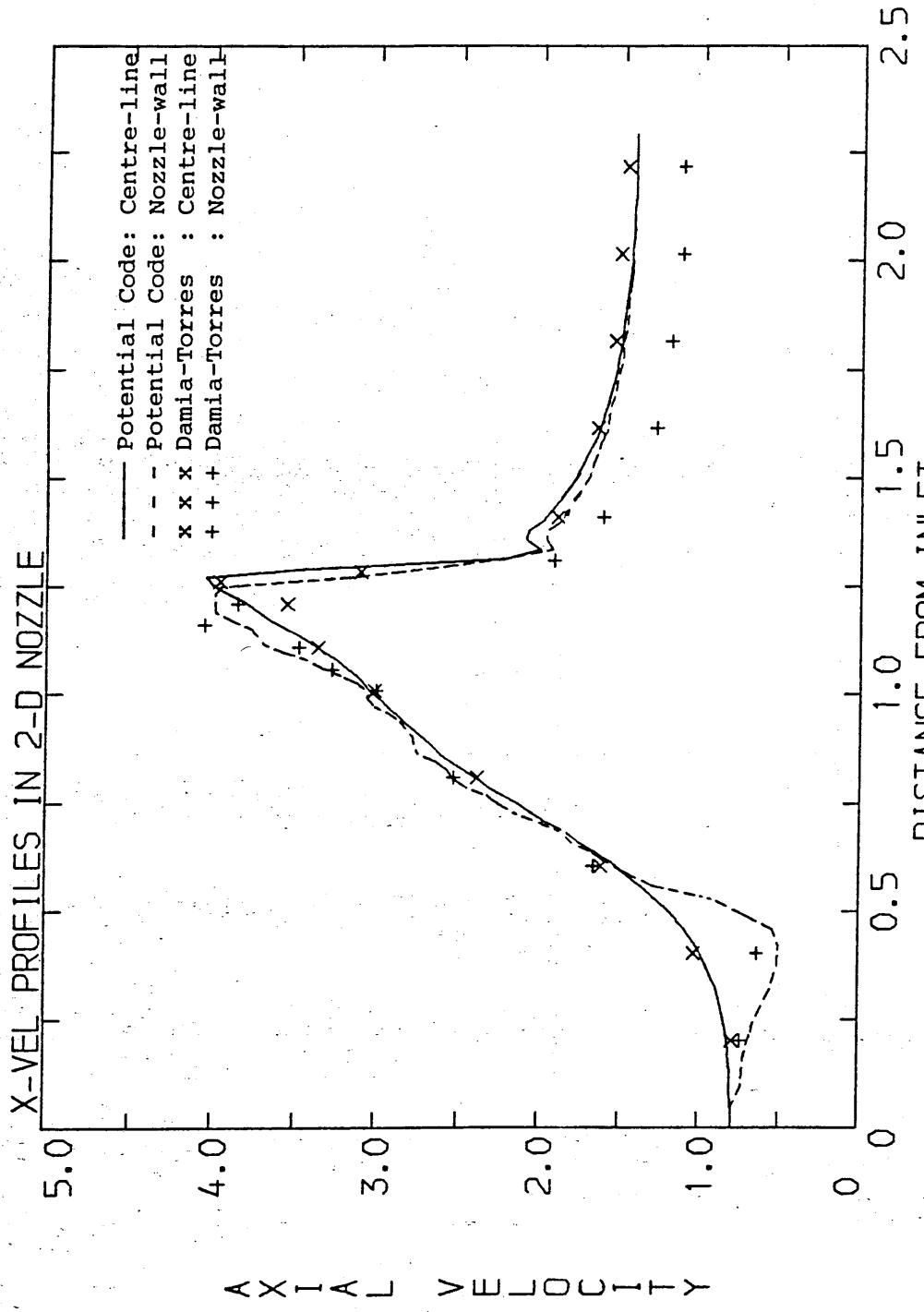

FIGURE 11. Distributions of Axial Velocity along the Nozzle, predicted by the 2D-VI Potential Code

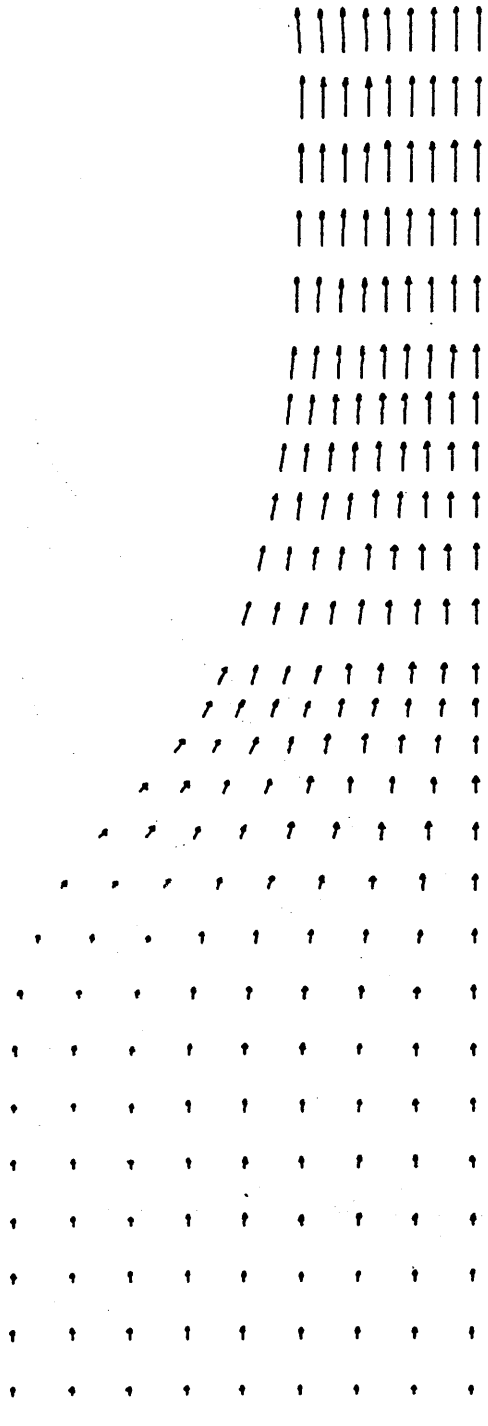

FIGURE 12. Vectors of Velocity in the Convergent Section of the Nozzle predicted by the 2D-VI Potential Code

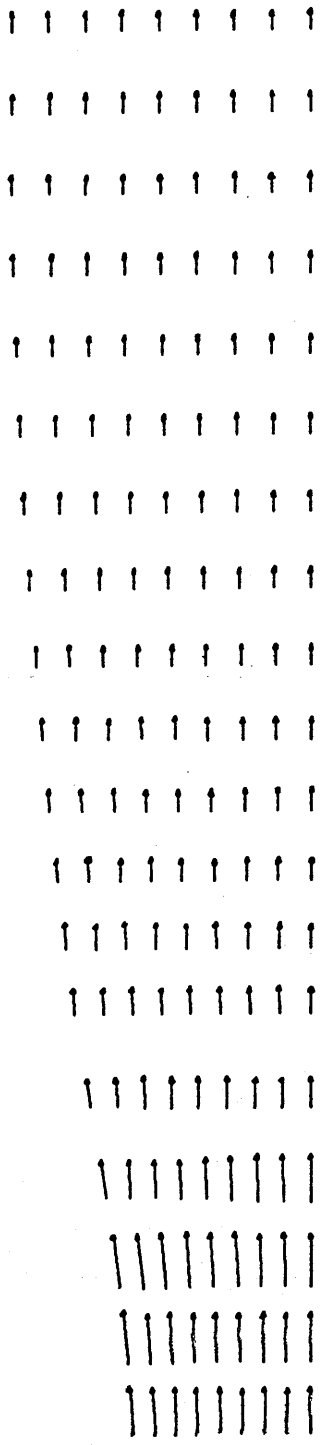

FIGURE 13. Vectors of Velocity in the Divergent Section of the Nozzle predicted by the 2D-VI code

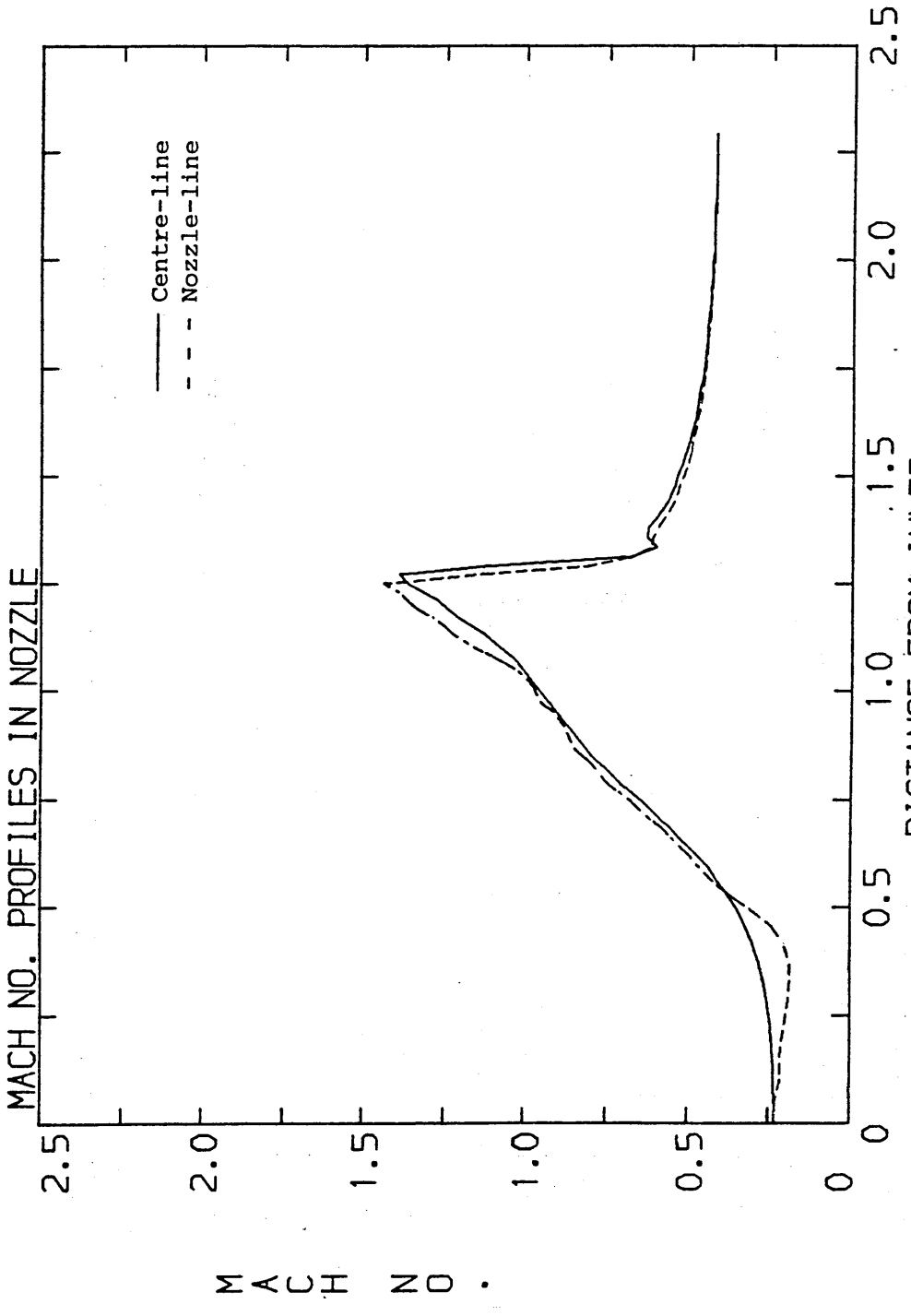

FIGURE 14. Distributions of Mach number along the nozzle predicted by the 2D-VI code

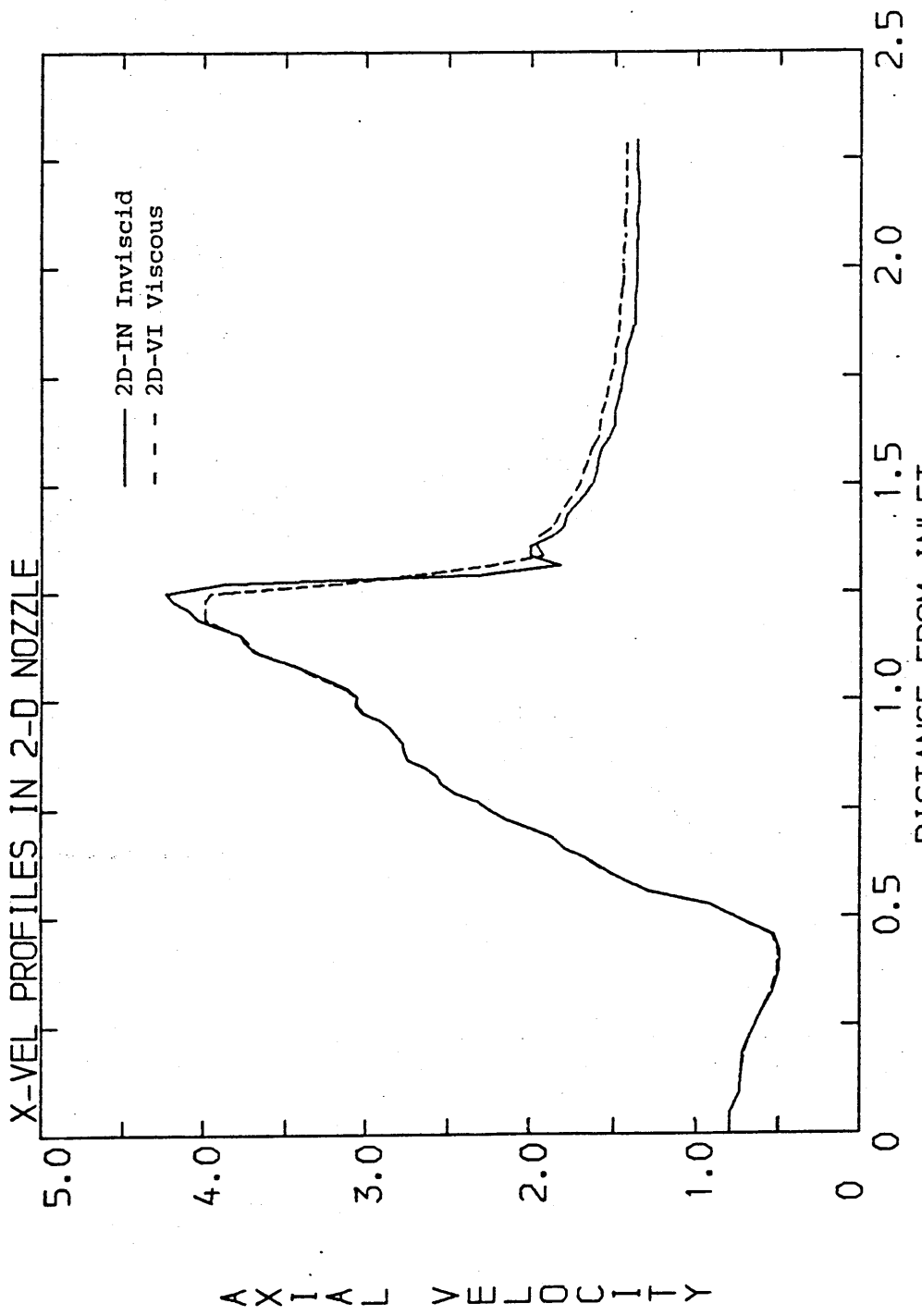

FIGURE 15. Distribution of Axial Velocity along the Nozzle-wall predicted by both the 2D-IN and the 2D-VI code

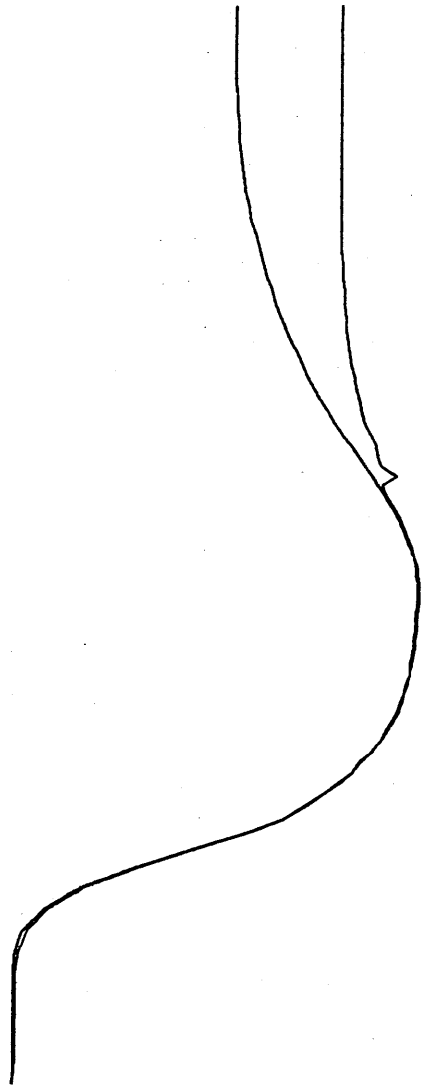

FIGURE 16. Distribution of Boundary-Layer Displacement along the Nozzle wall

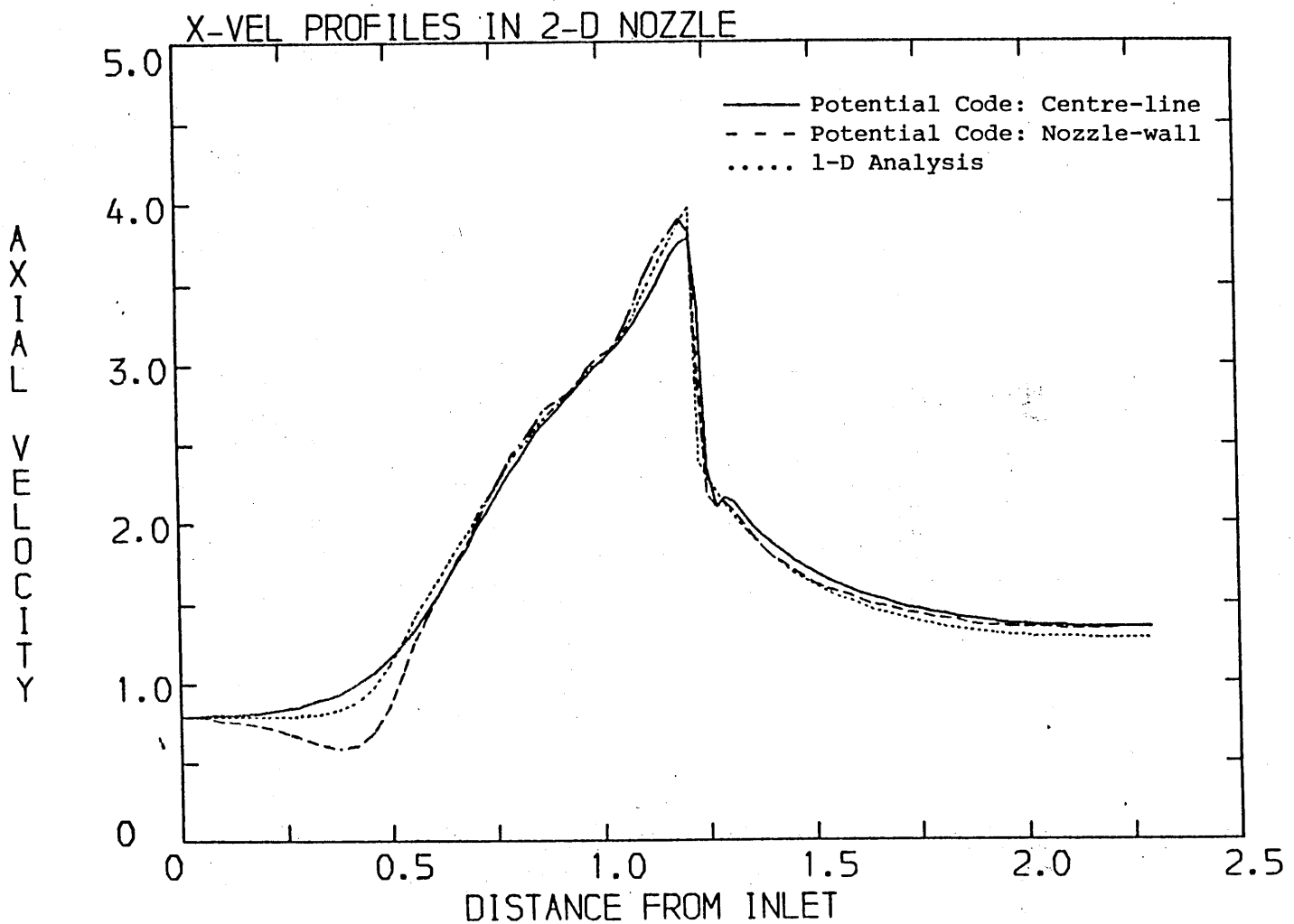

FIGURE 17. Distributions of Axial Velocity along the Nozzle, operating at a low pressure-ratio, predicted by the 2D-IN code

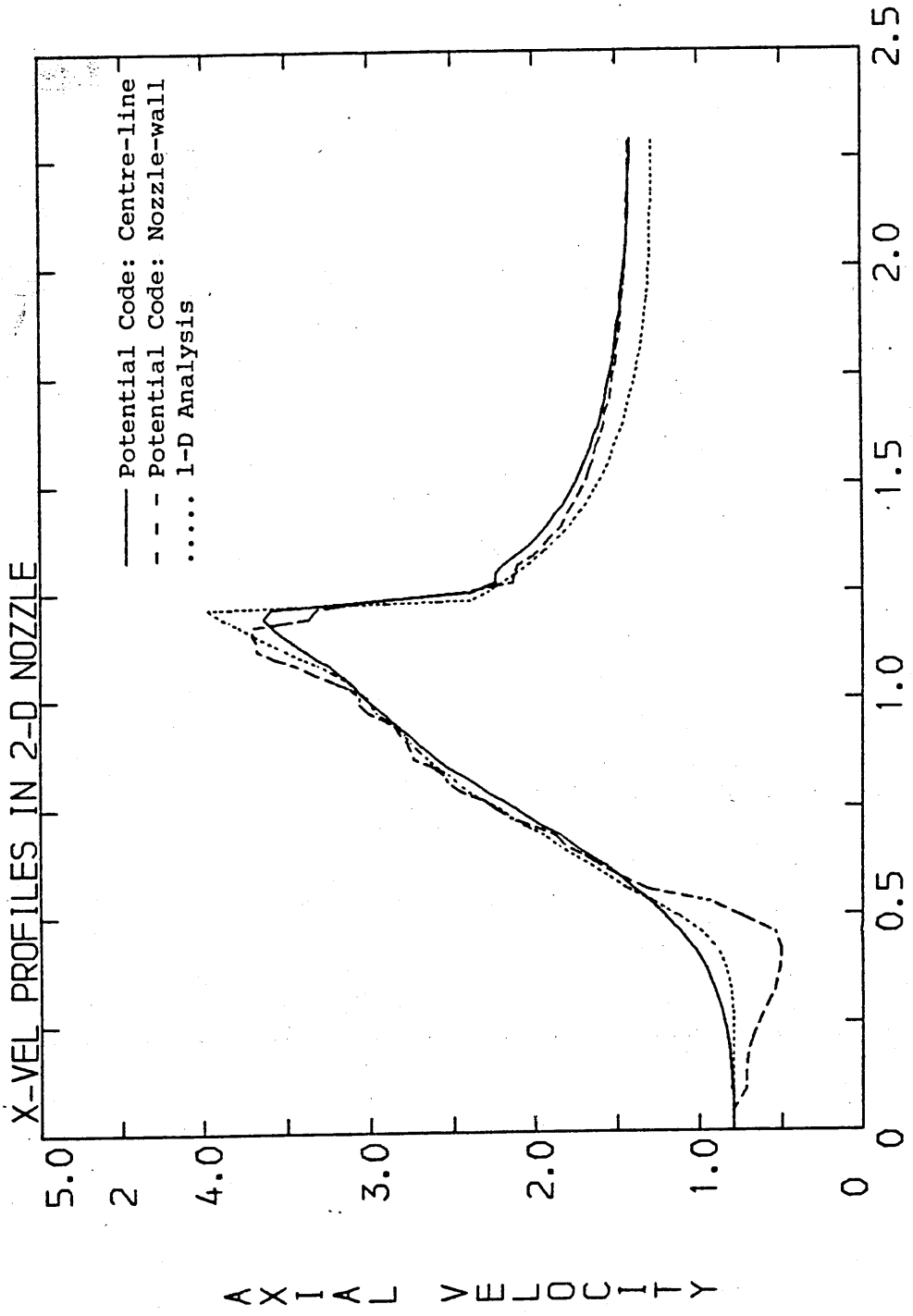

FIGURE 18. Distributions of Axial Velocity along the Nozzle, operating at a low pressure ratio, predicted by the 2D-VI code

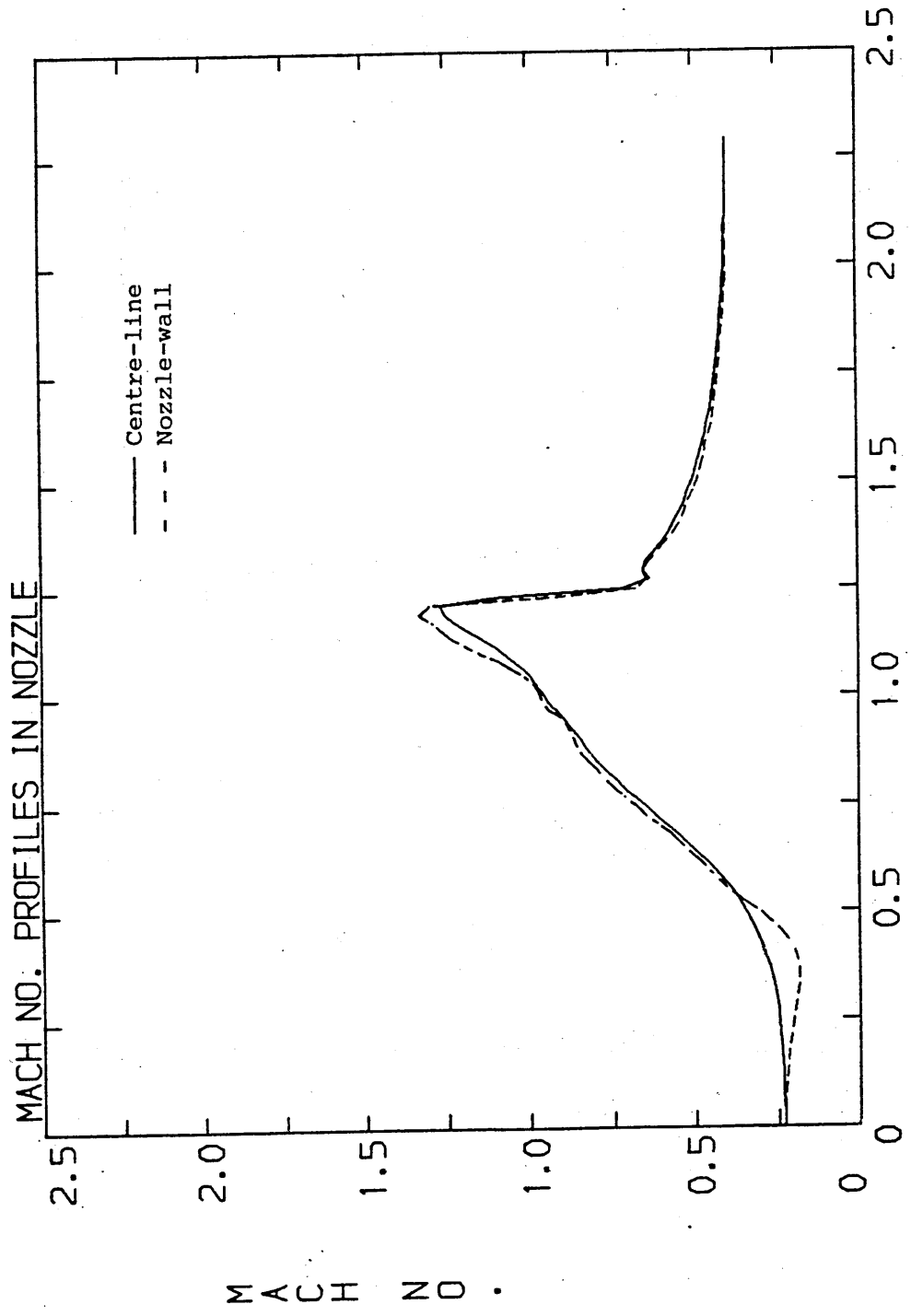

FIGURE 19. Distributions of Mach number along the Nozzle, operating at a low pressure ratio, predicted by the 2D-IN code

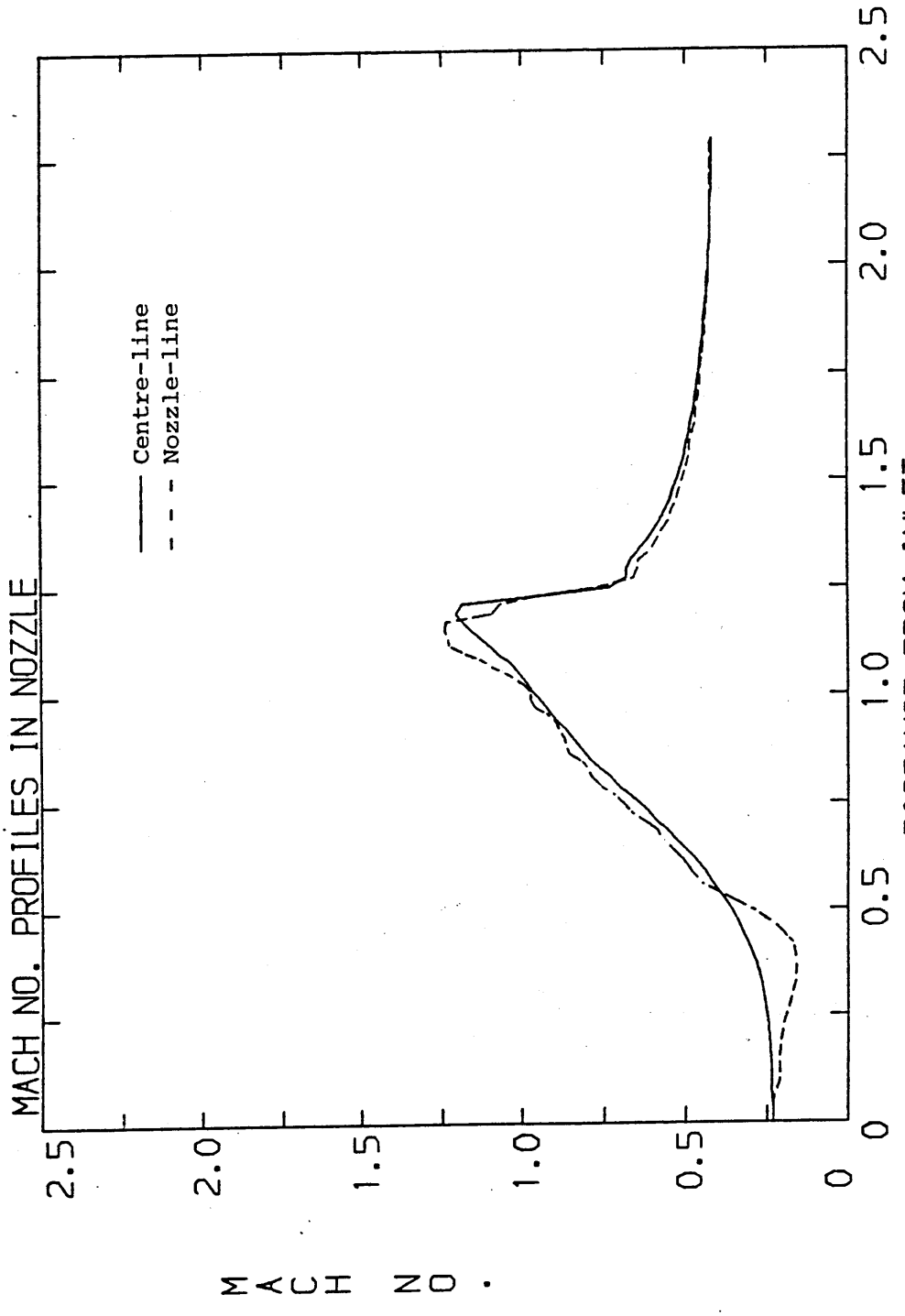

FIGURE 20. Distributions of Mach number along the Nozzle, operating at a low pressure ratio, predicted by the 2D-VI code

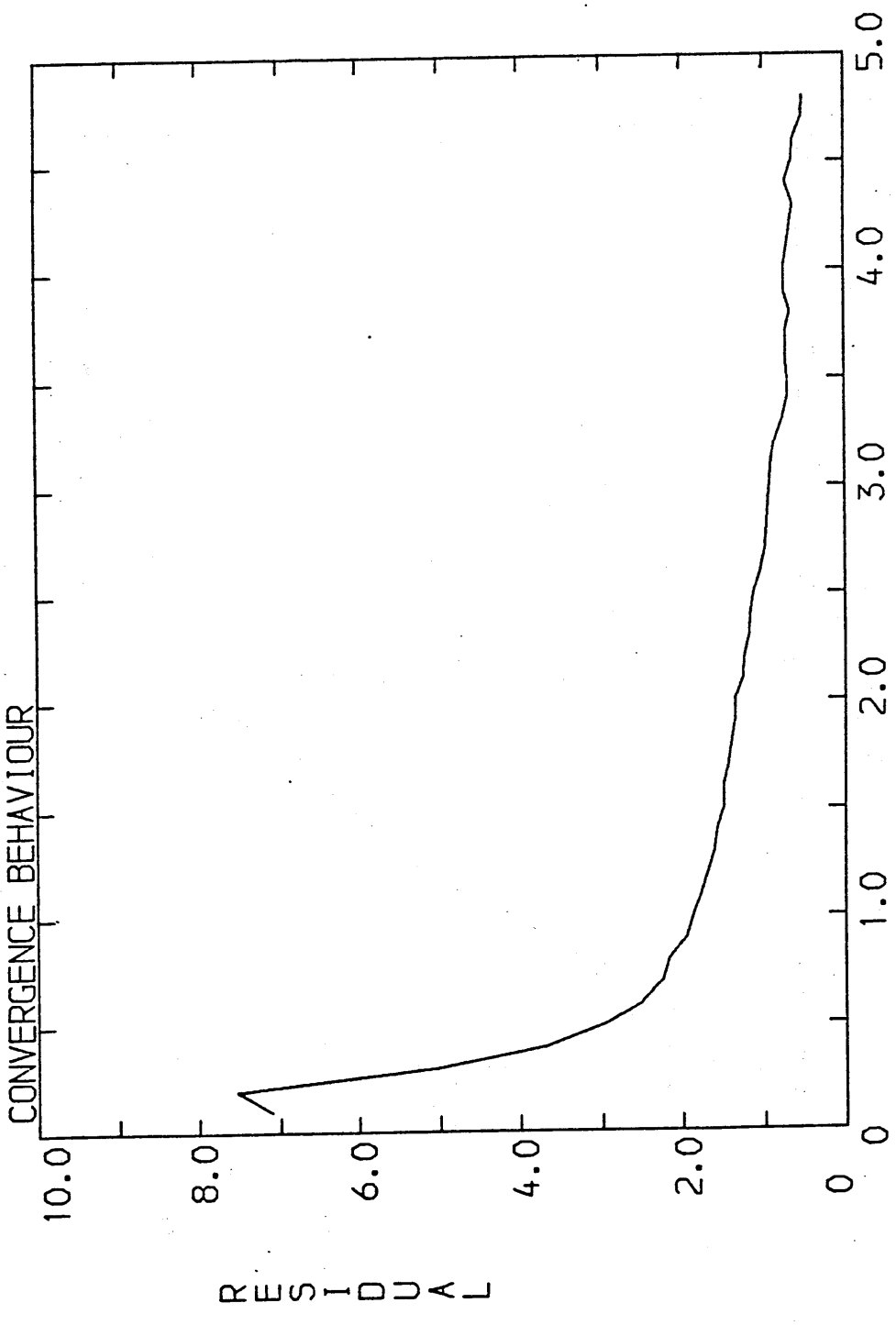

FIGURE 21. The Convergence Behaviour of the 2D-IN solution

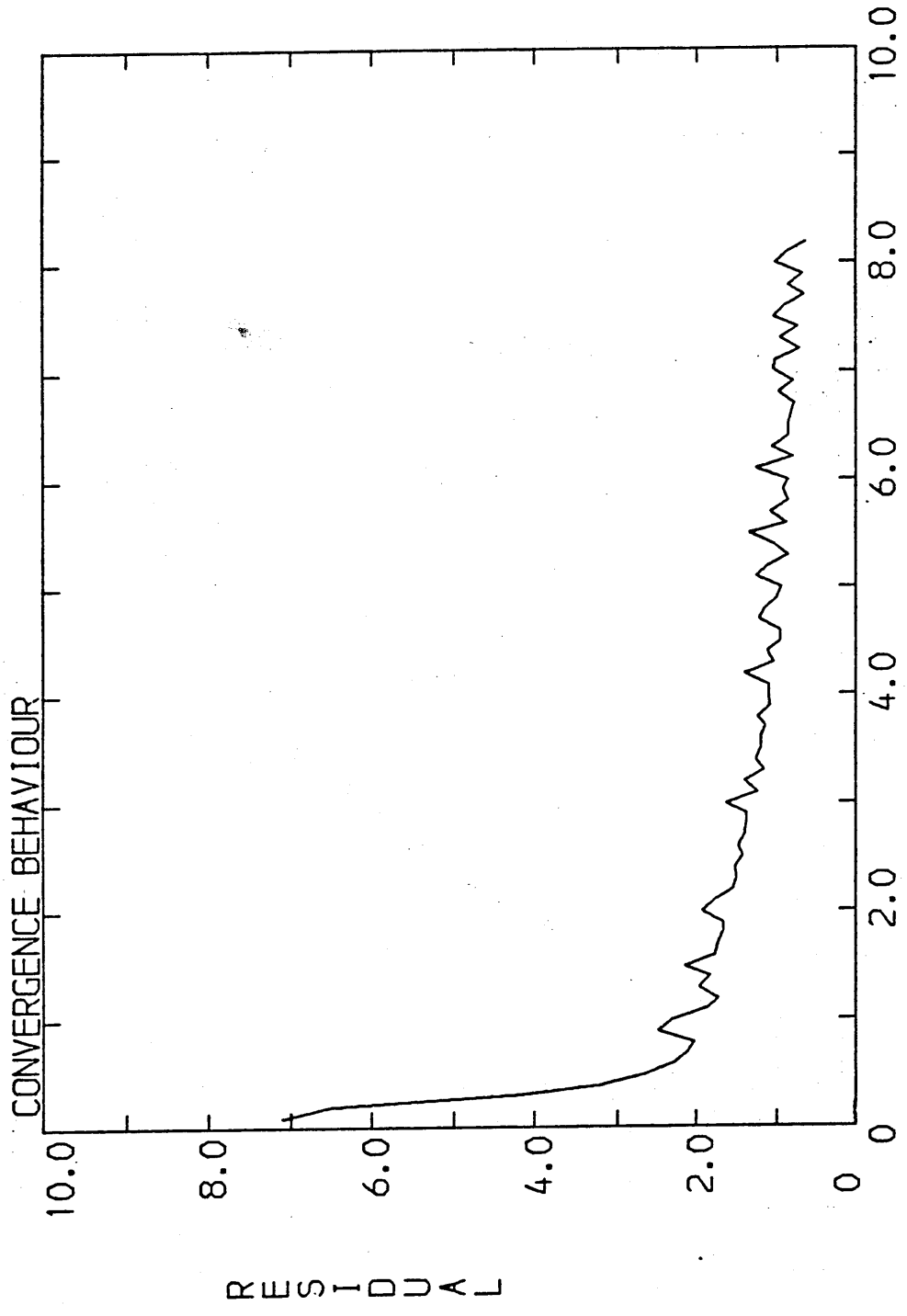

FIGURE 22. The Convergence Behaviour of the 2D-VI solution

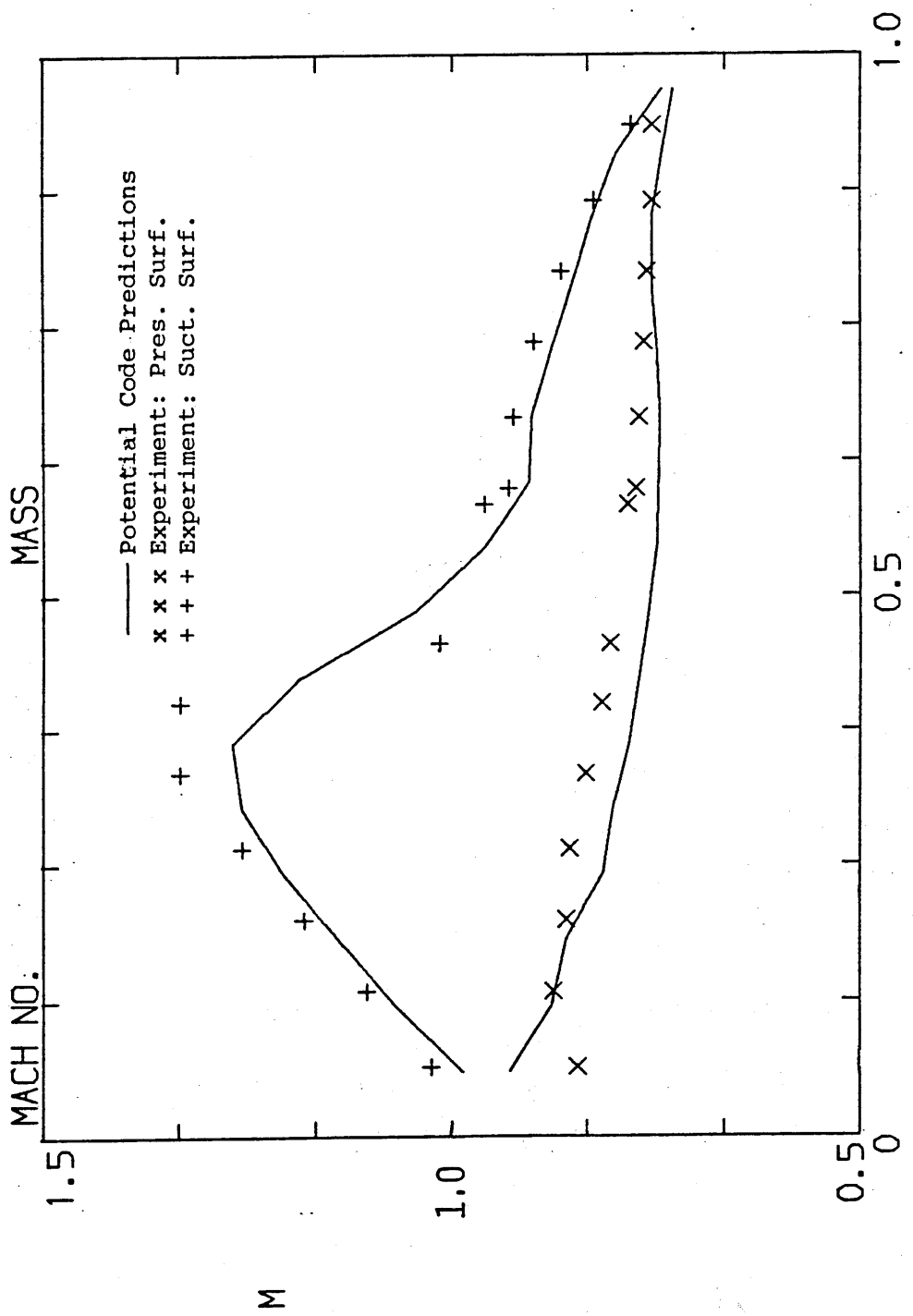

FIGURE 23. The Distributions of Mach number along the Blade surfaces, predicted by the CAS-IN code

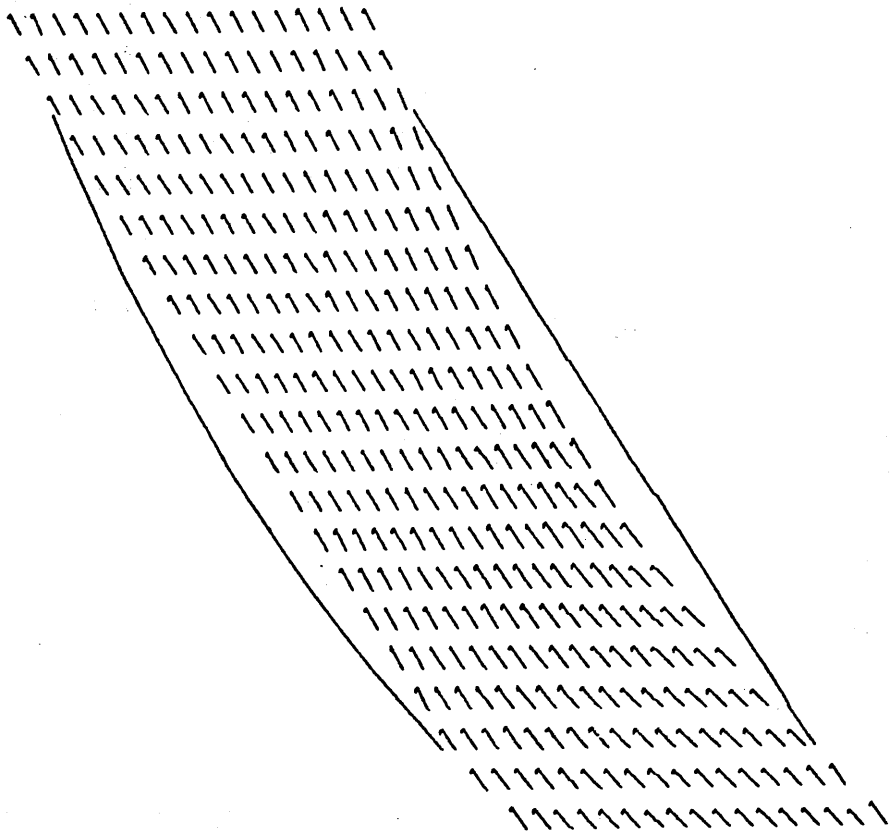

FIGURE 24. The Vectors of Velocity within the Cascade Blade channel, predicted by the CAS-IN code

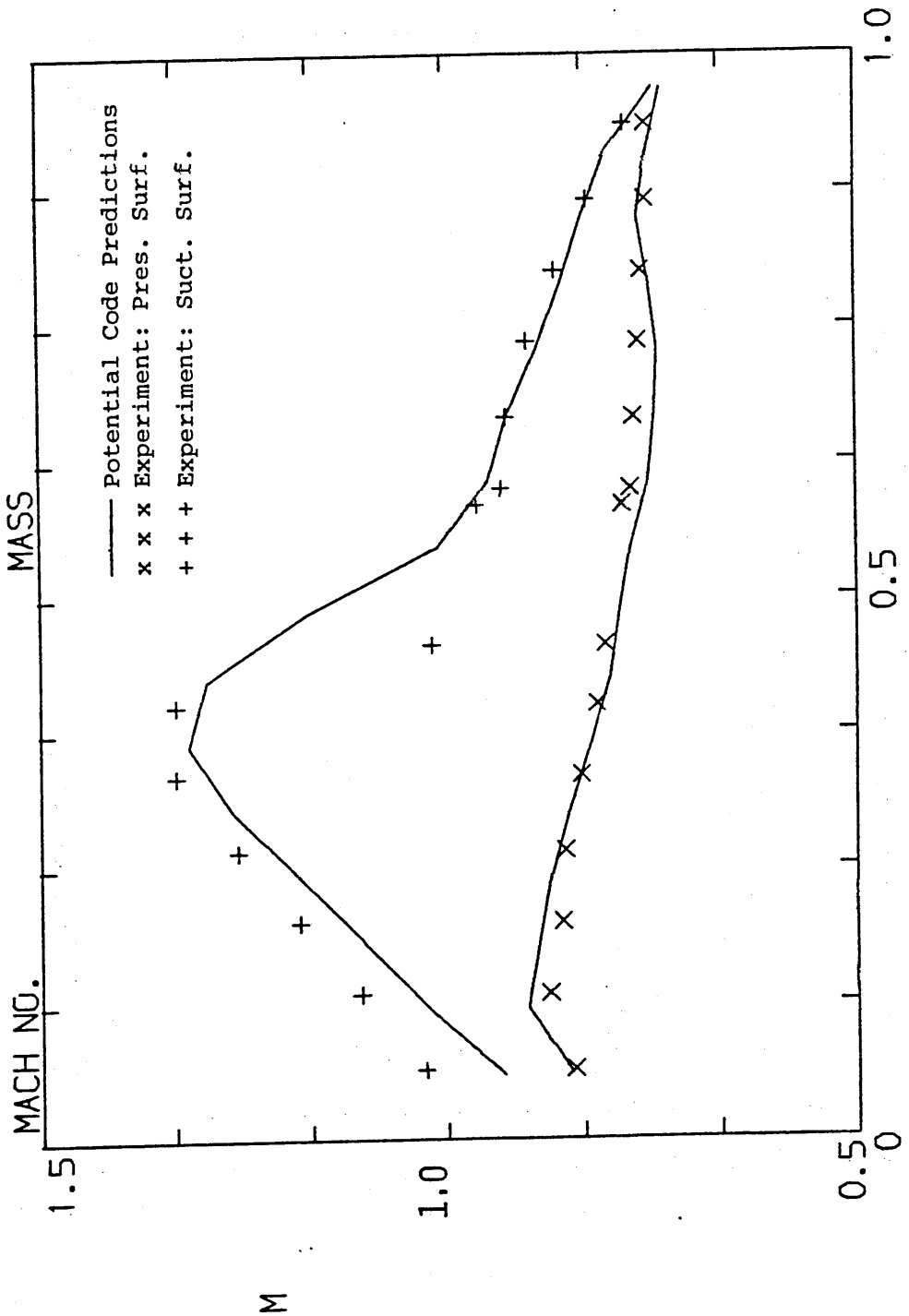

FIGURE 25. The Distribution of Mach number along the Blade surfaces predicted by the CAS-VI code

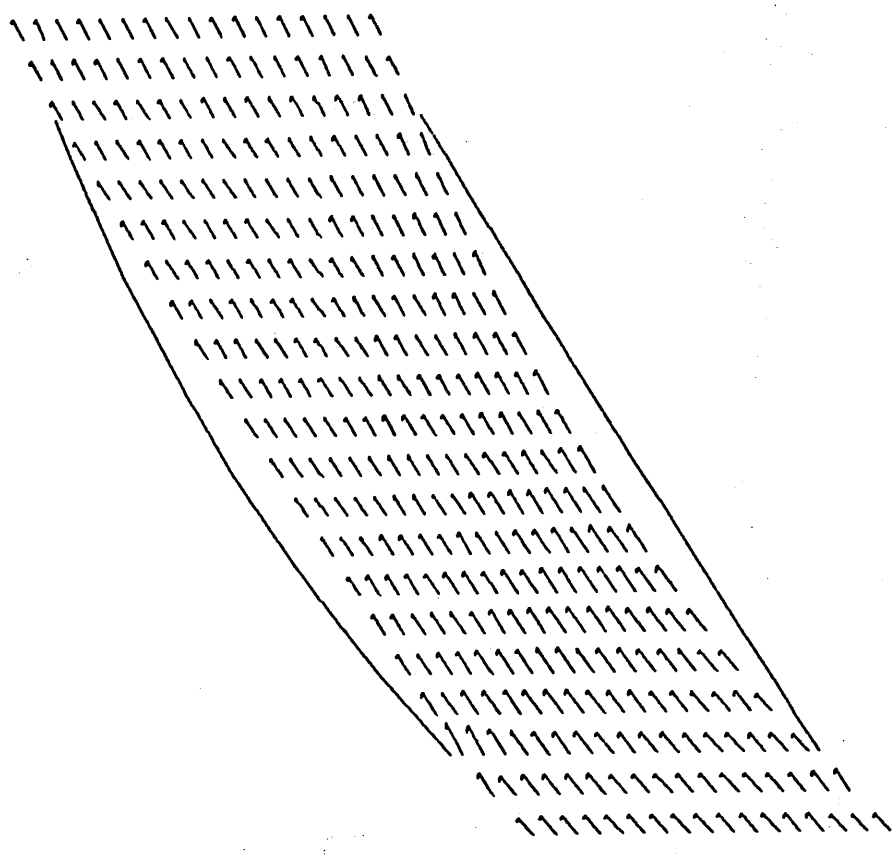

FIGURE 26. The Vectors of Velocity within the Cascade Blade channel predicted by the CAS-VI code

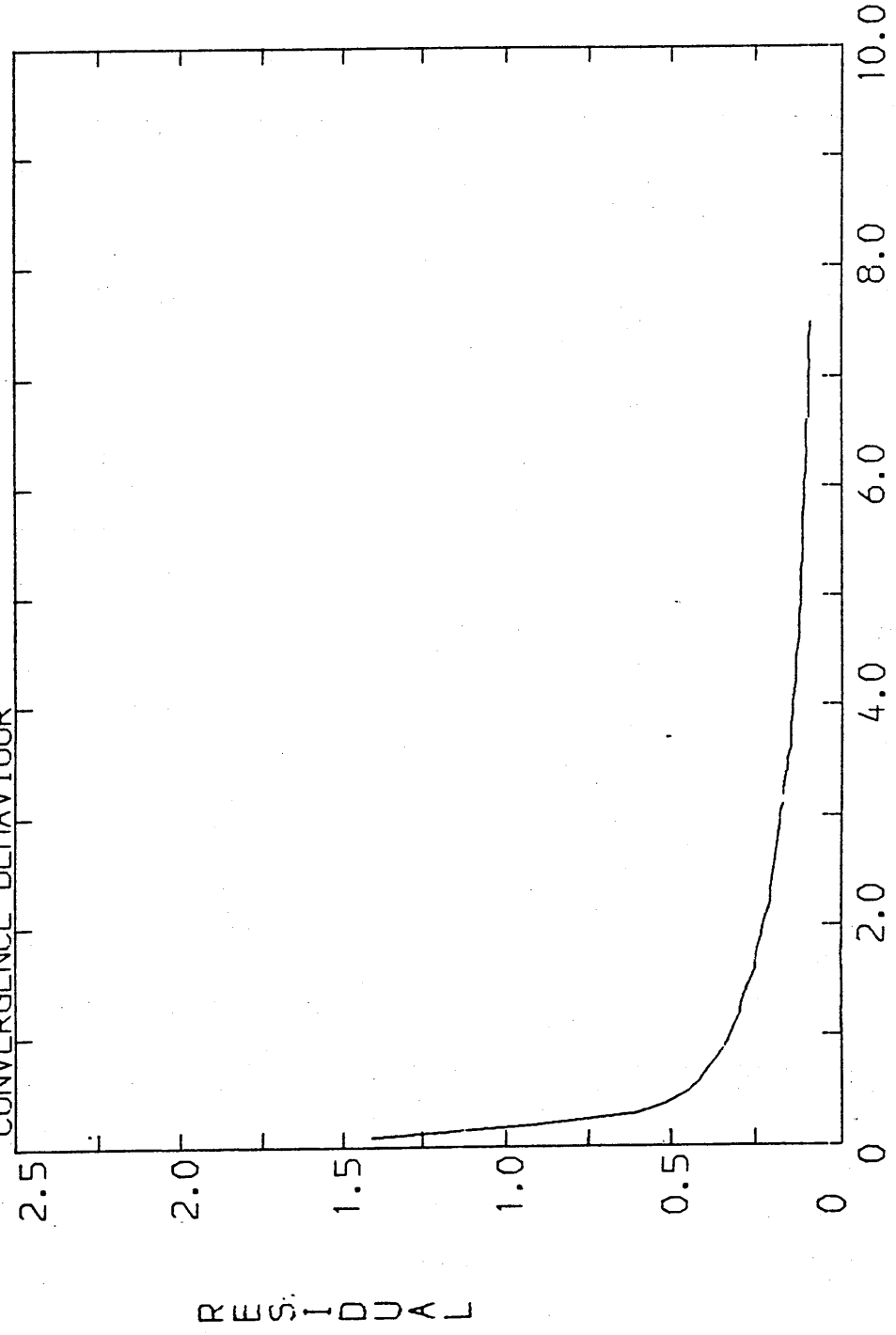

FIGURE 27. The Convergence Behaviour of the CAS-IN code

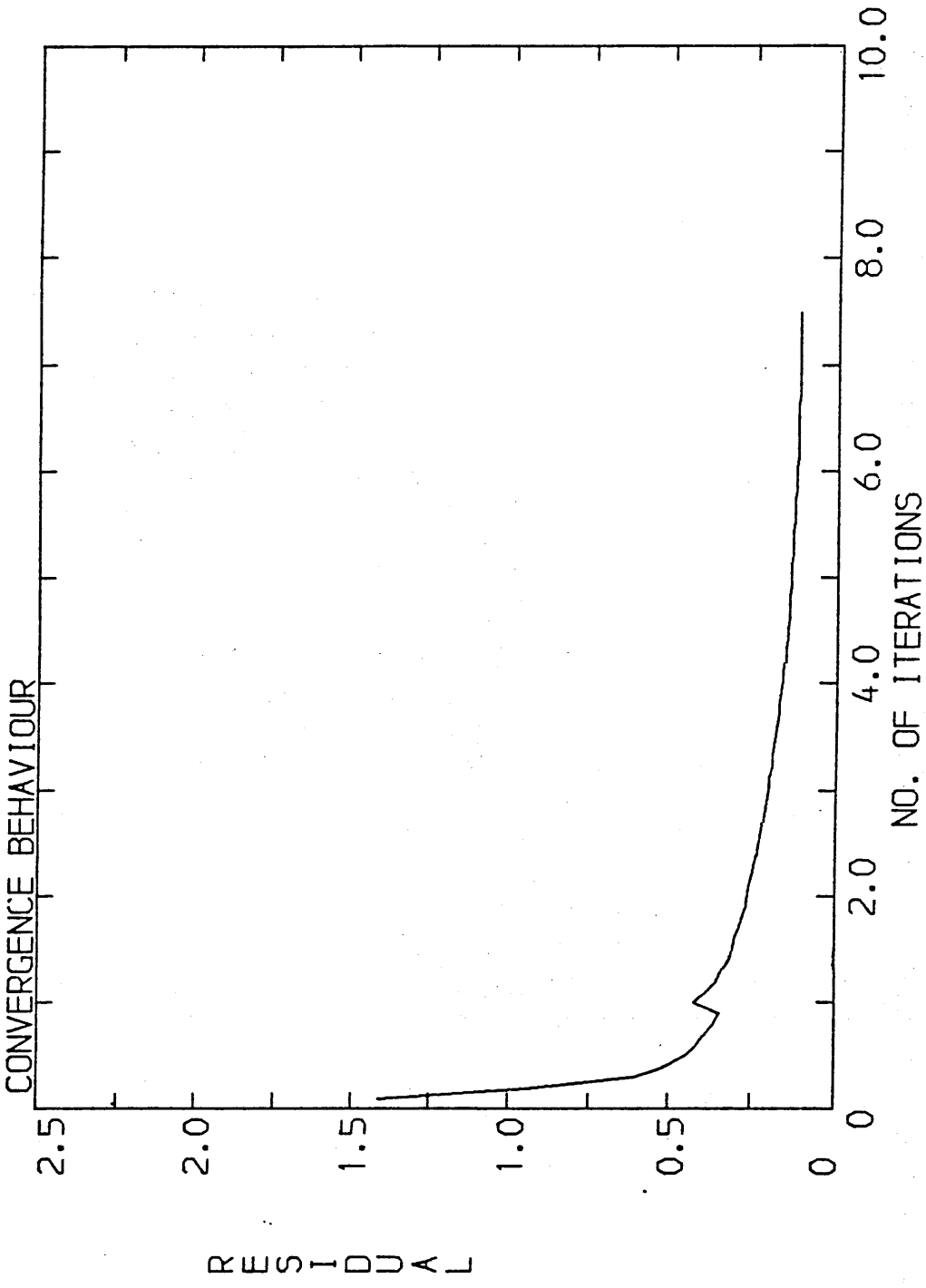

FIGURE 28. The Convergence Behaviour of the CAS-VI code

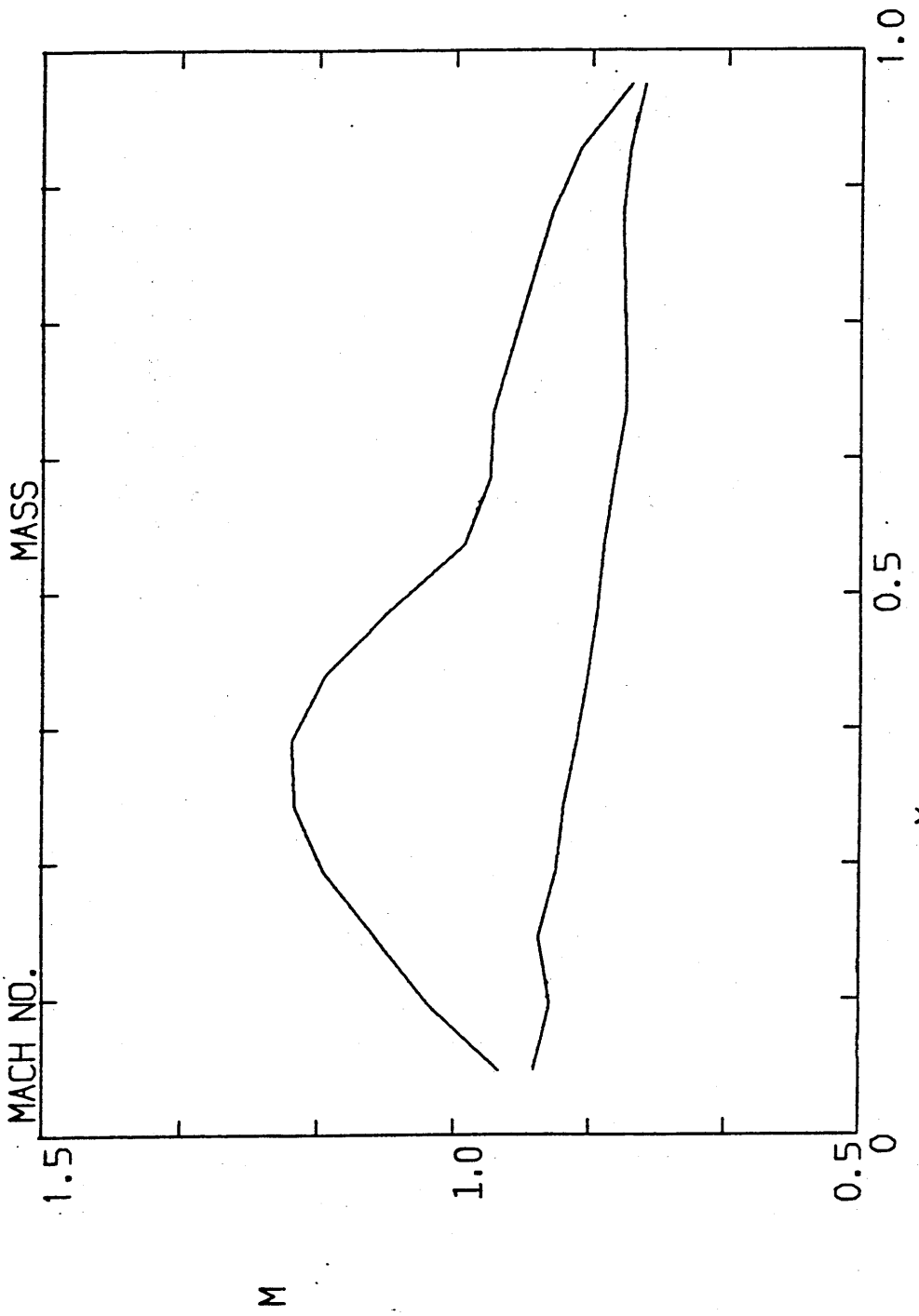

FIGURE 29. The Distributions of Mach number predicted by the CAS-VI code for an Inlet-Airflow Angle of 56.42°

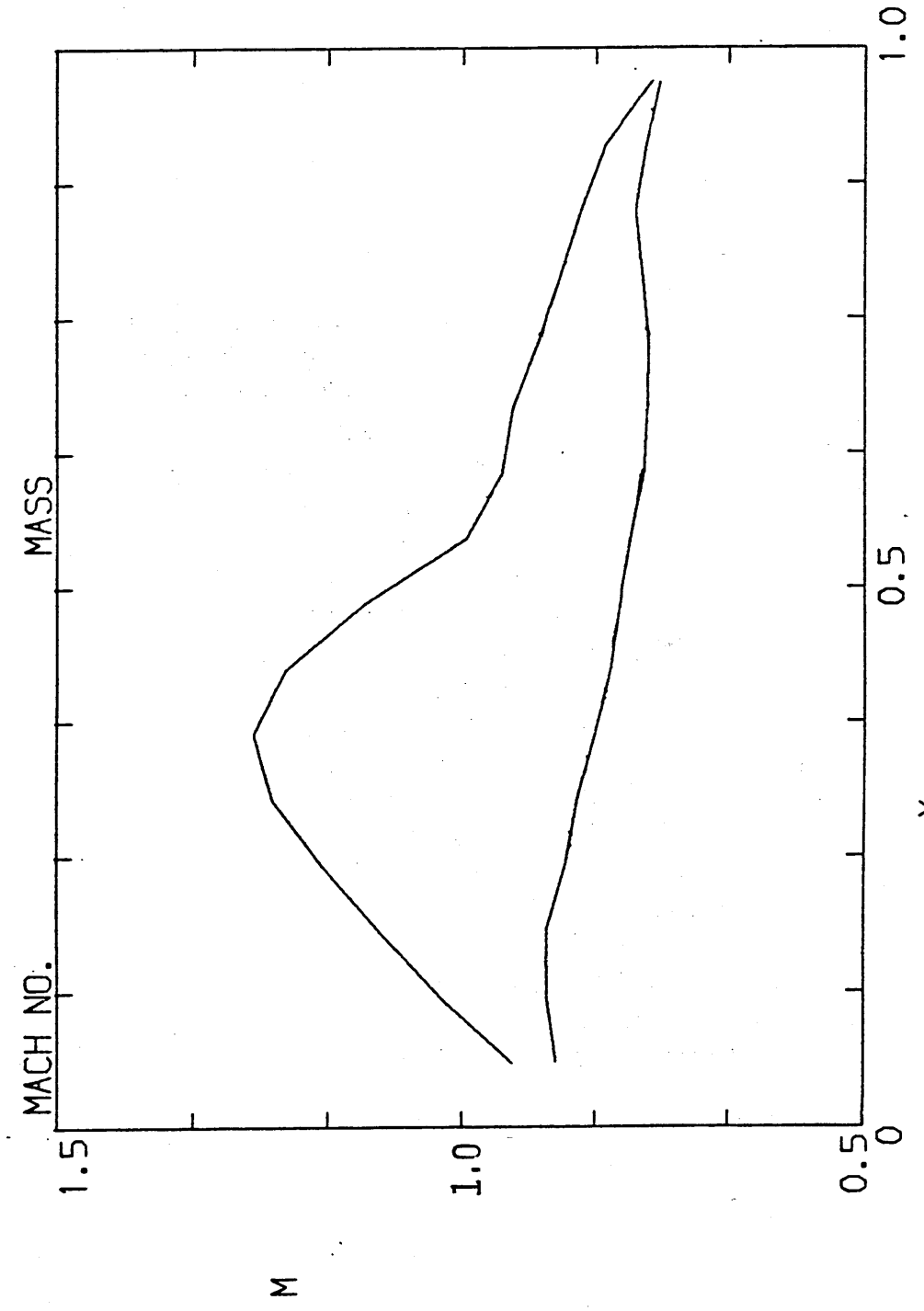

FIGURE 30. The Distributions of Mach number predicted by the CAS-VI code for an Inlet-Airflow Angle of 57.42°

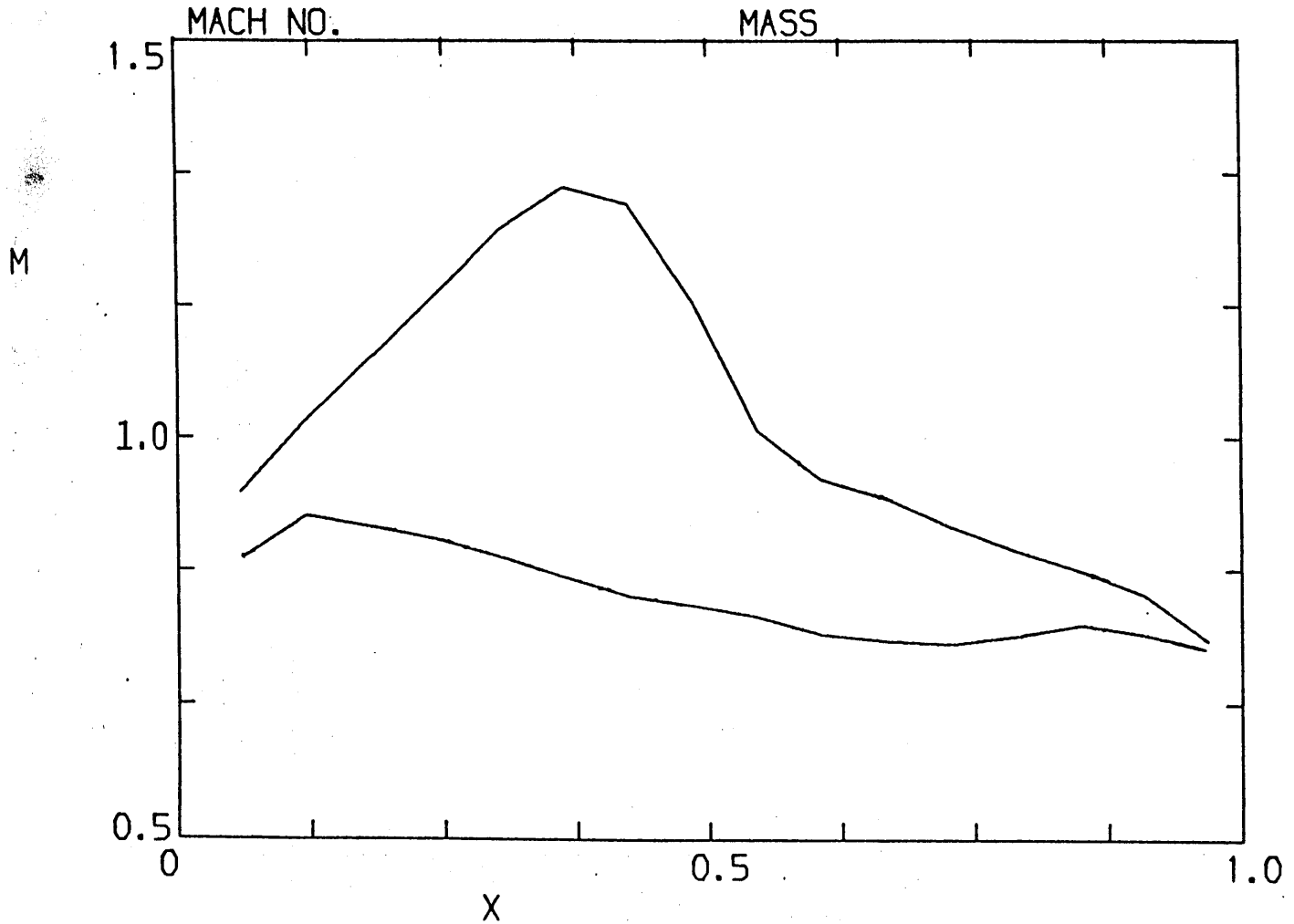

FIGURE 31. The Distributions of Mach number, predicted by the CAS-VI code, for an Inlet-Airflow Angle of 58.42°

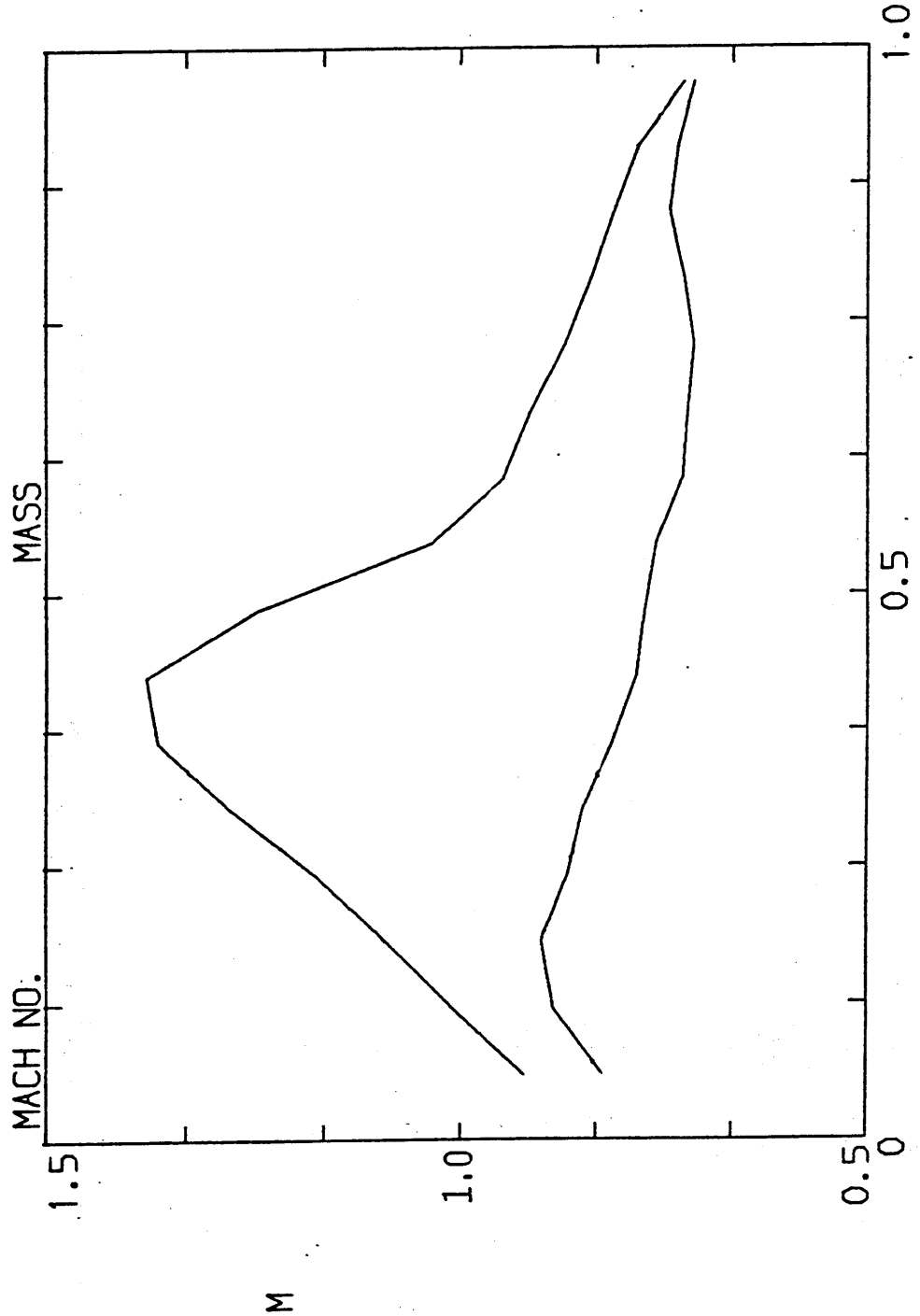

FIGURE 32. The Distributions of Mach number, predicted by the CAS-VI code, for an Inlet-Airflow Angle of 59.42°

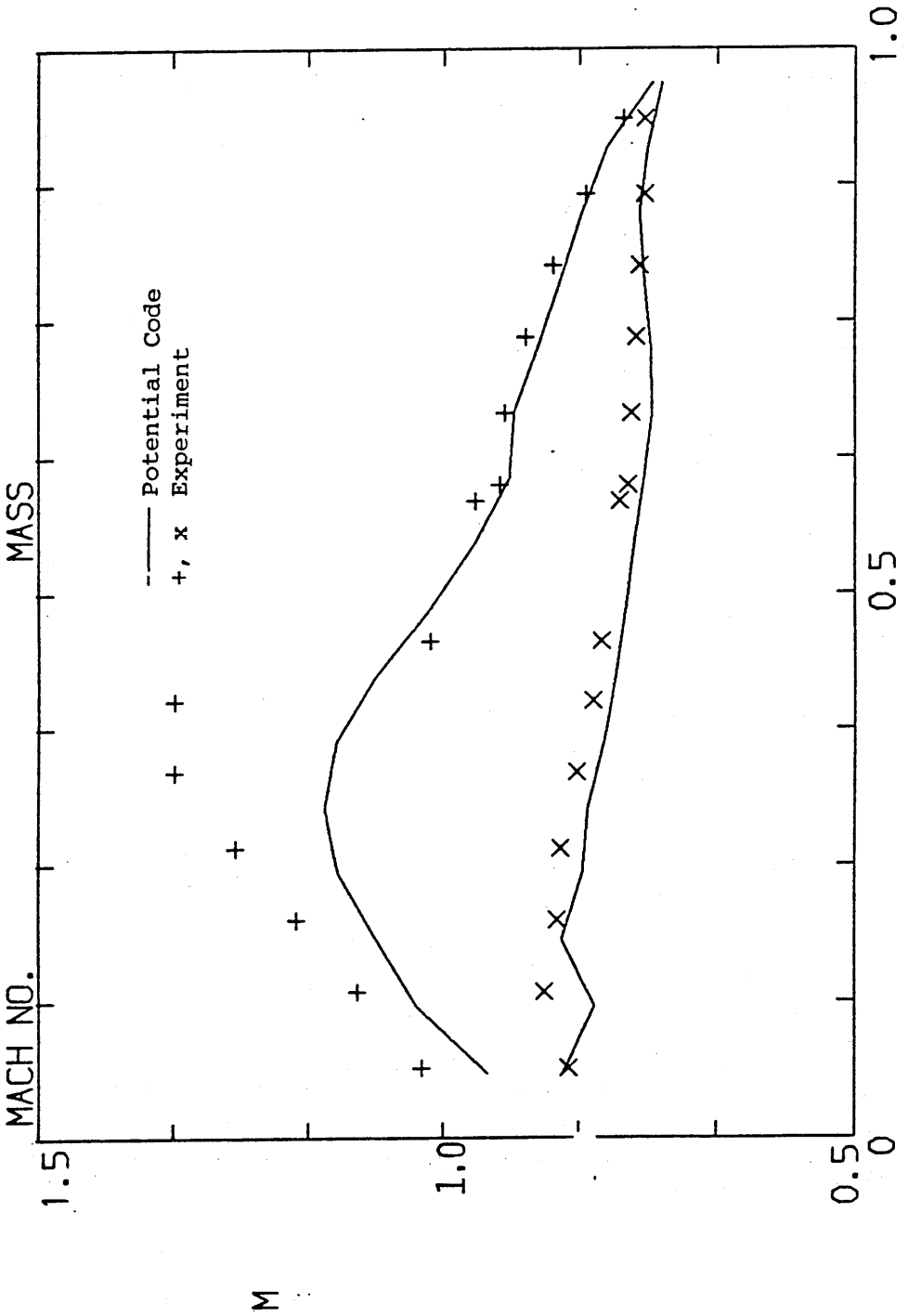

FIGURE 33. The Distribution of Mach number, corresponding to a set exit pressure of 67141.9 Pa, predicted by the CAS-VI code

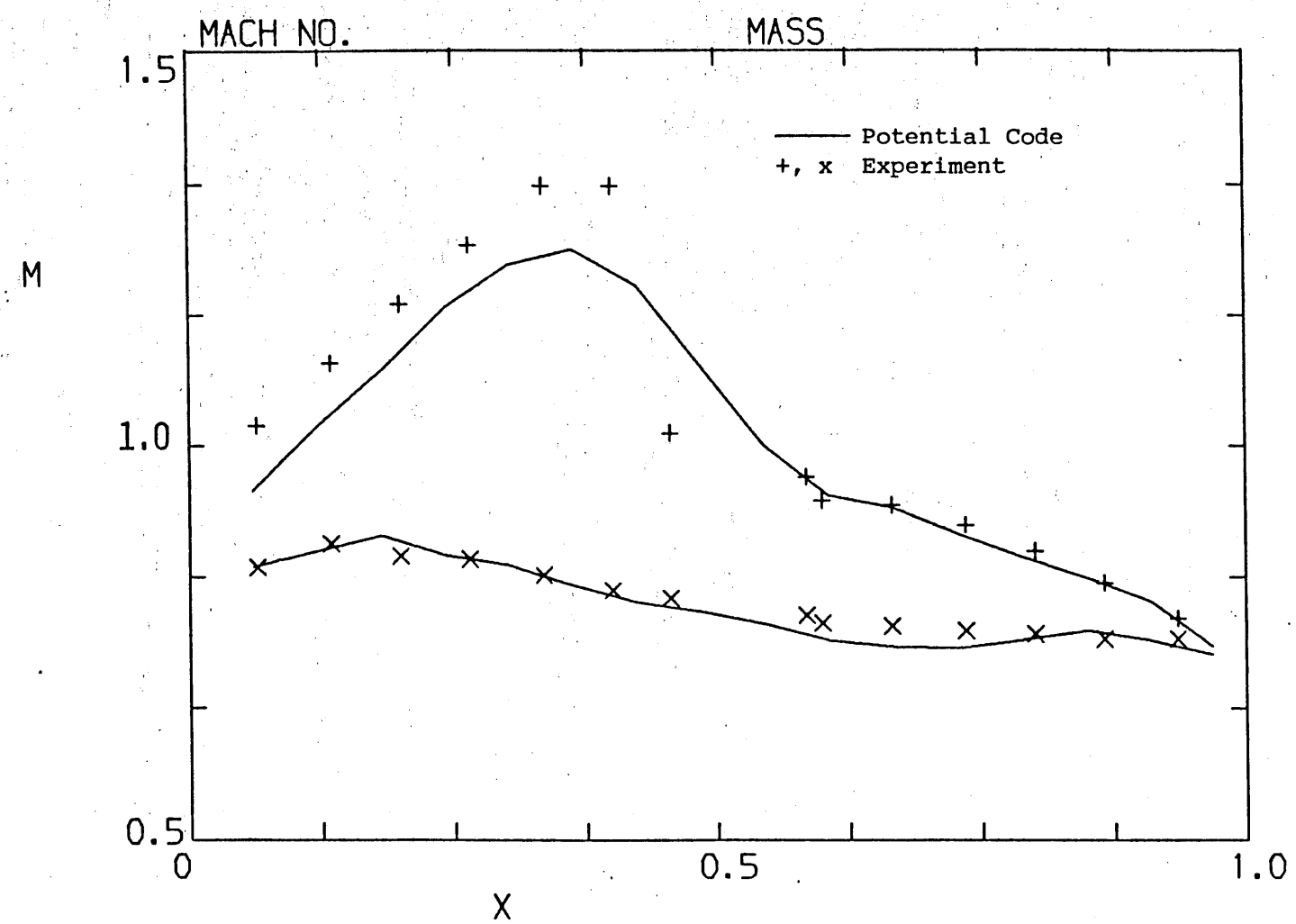

FIGURE 34. The Distributions of Mach number, corresponding to a set exit pressure of 66962.9 Pa, predicted by the CAS-VI code

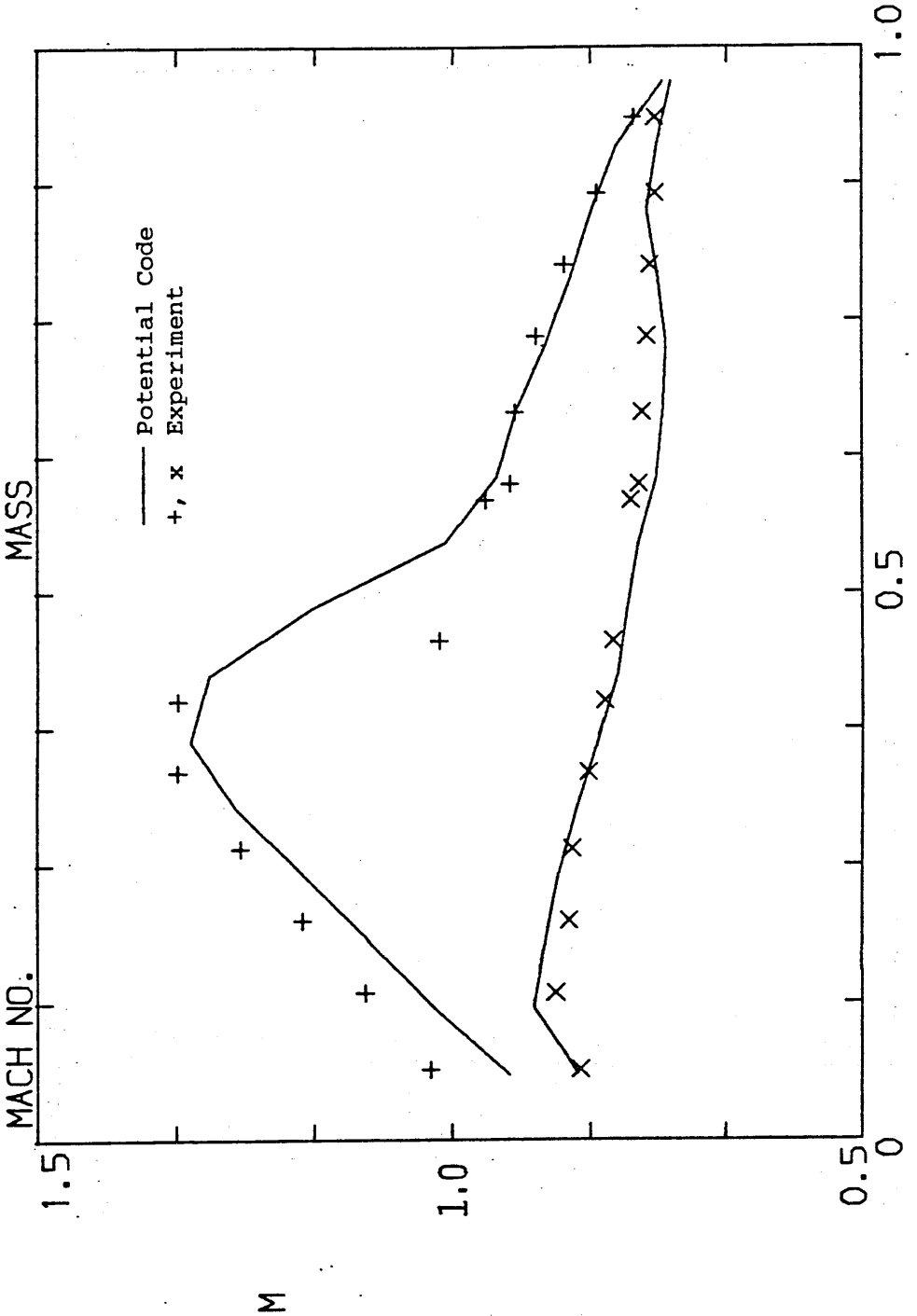

FIGURE 35. The Distributions of Mach number, corresponding to a set exit pressure of 66804.9 Pa, predicted by the CAS-VI code

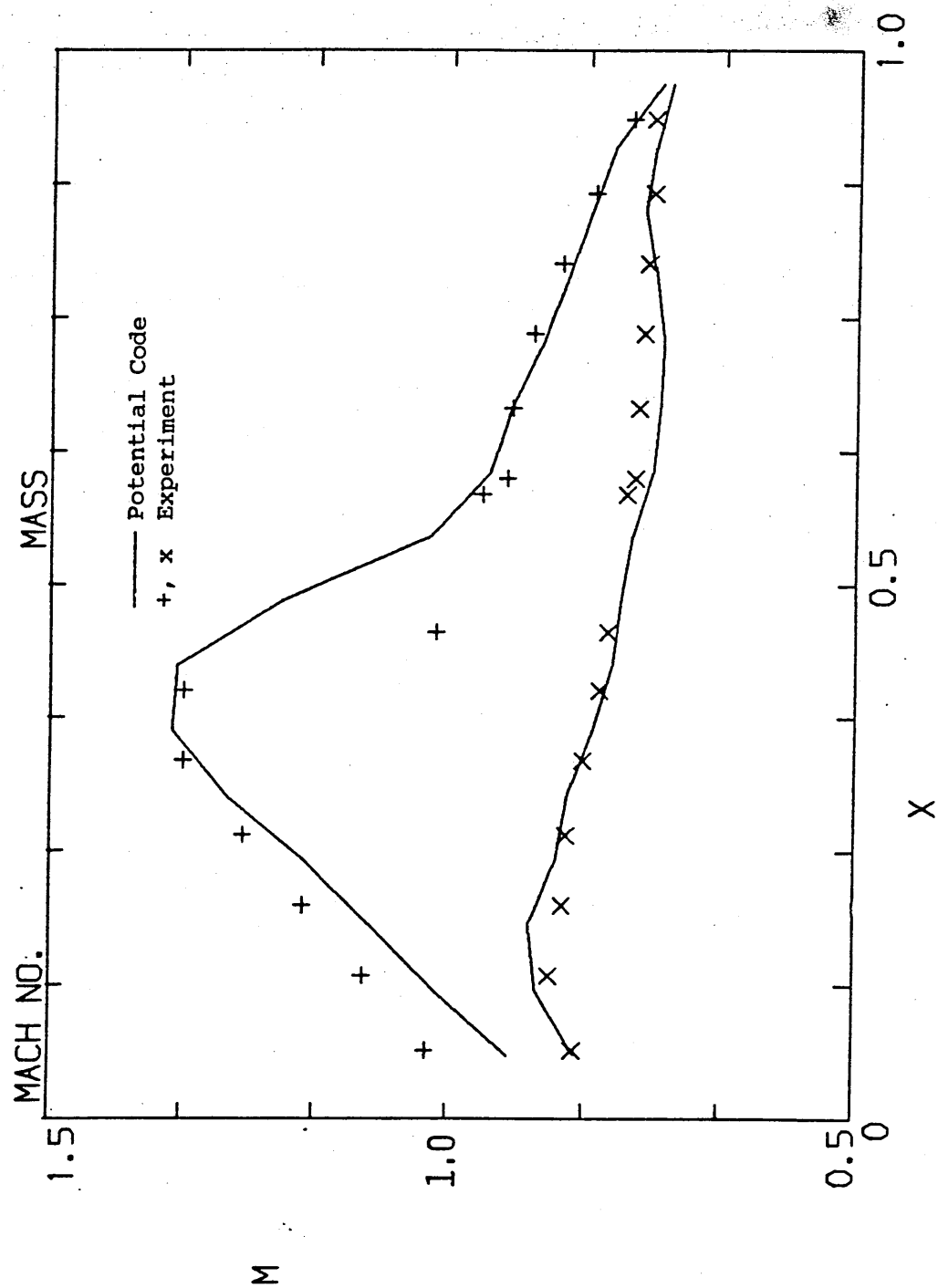

FIGURE 36. The Distributions of Mach number, corresponding to a set exit pressure of 66672.1 Pa, predicted by the CAS-VI code

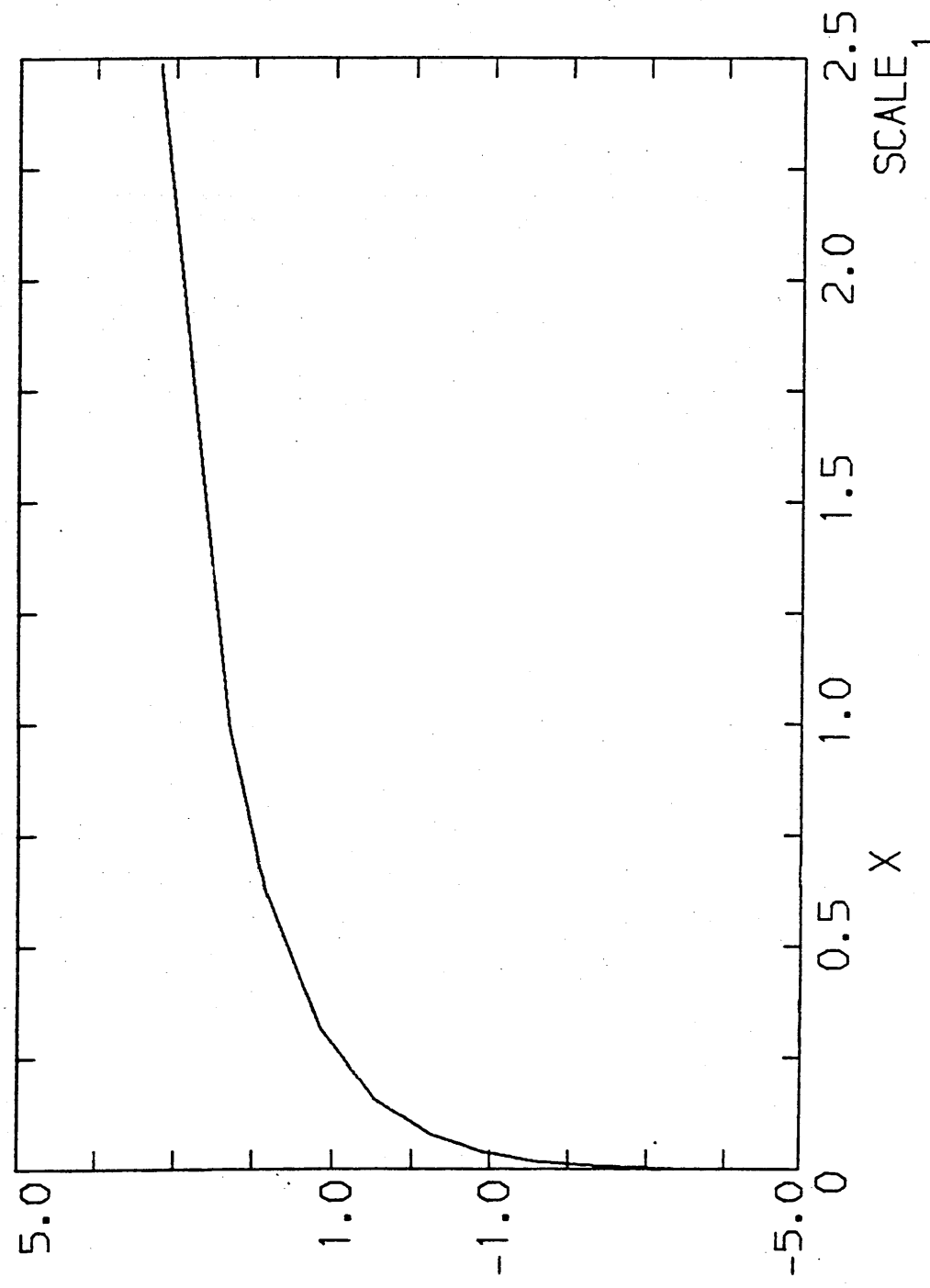

FIGURE 37. Variation of the natural log of a function with the function itself

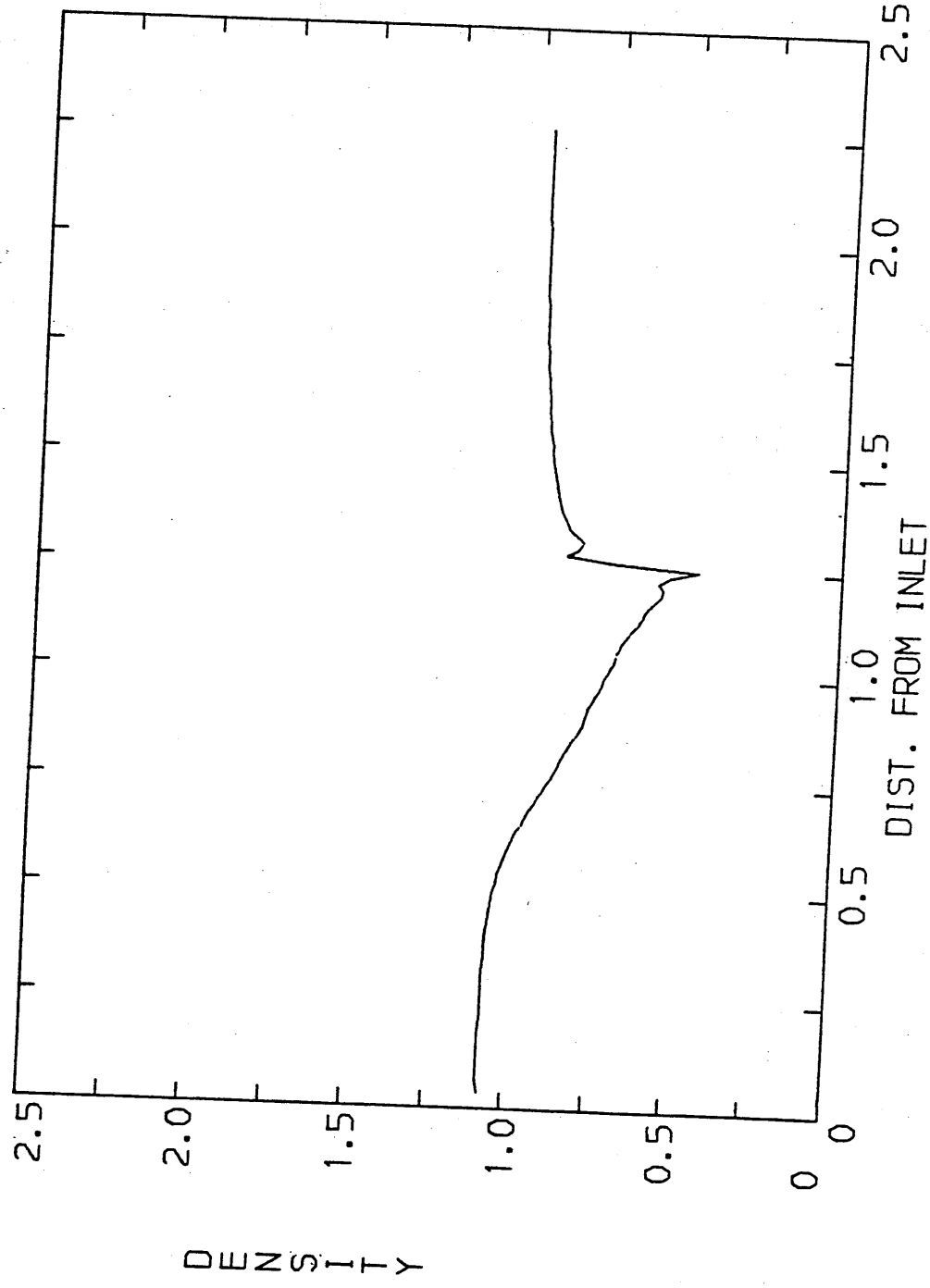

FIGURE 38. Distribution of the product of density and blockage, along the nozzle wall, predicted by the 2D-IN code

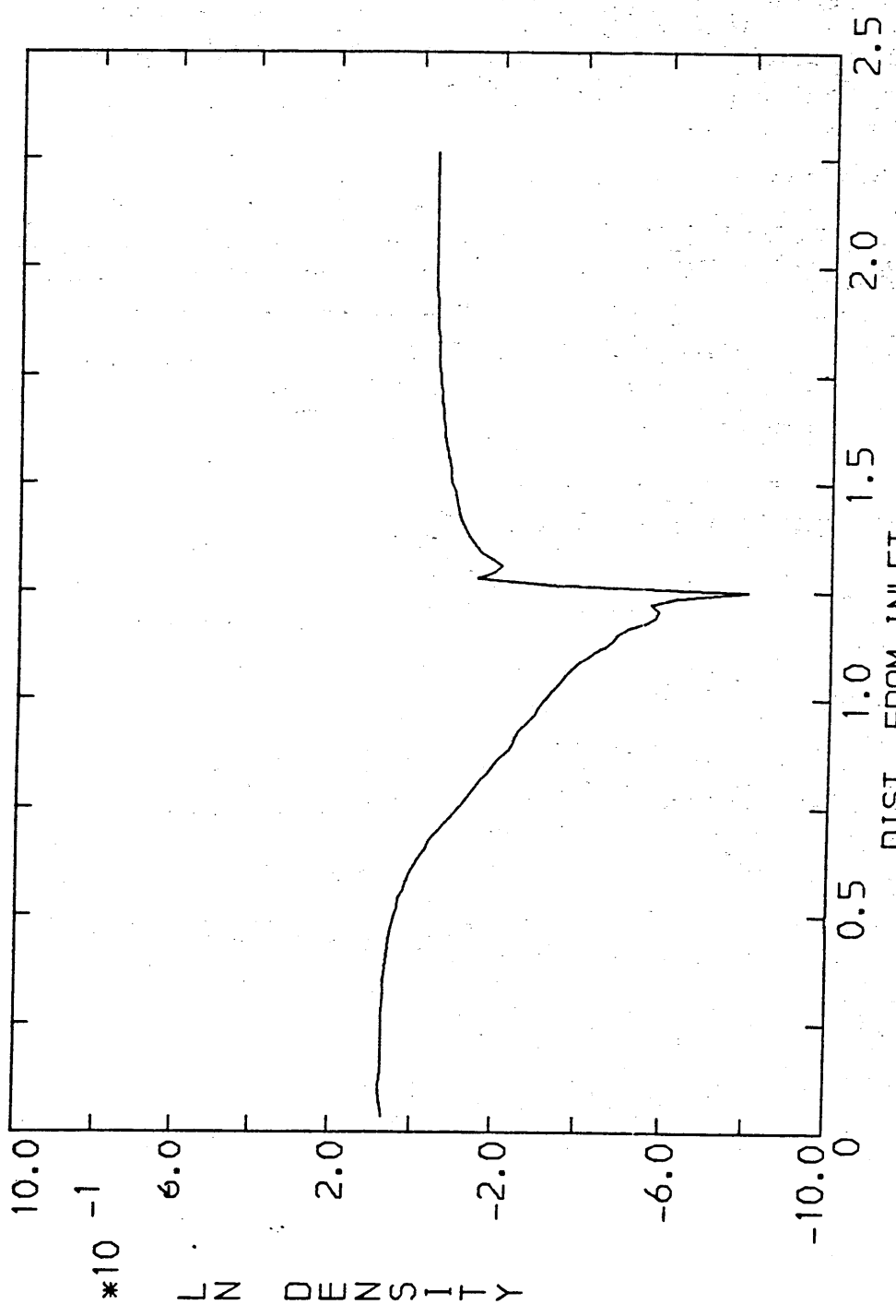

FIGURE 39. Distribution of the ln (density x blockage along the nozzle wall, predicted by the 2D-IN code

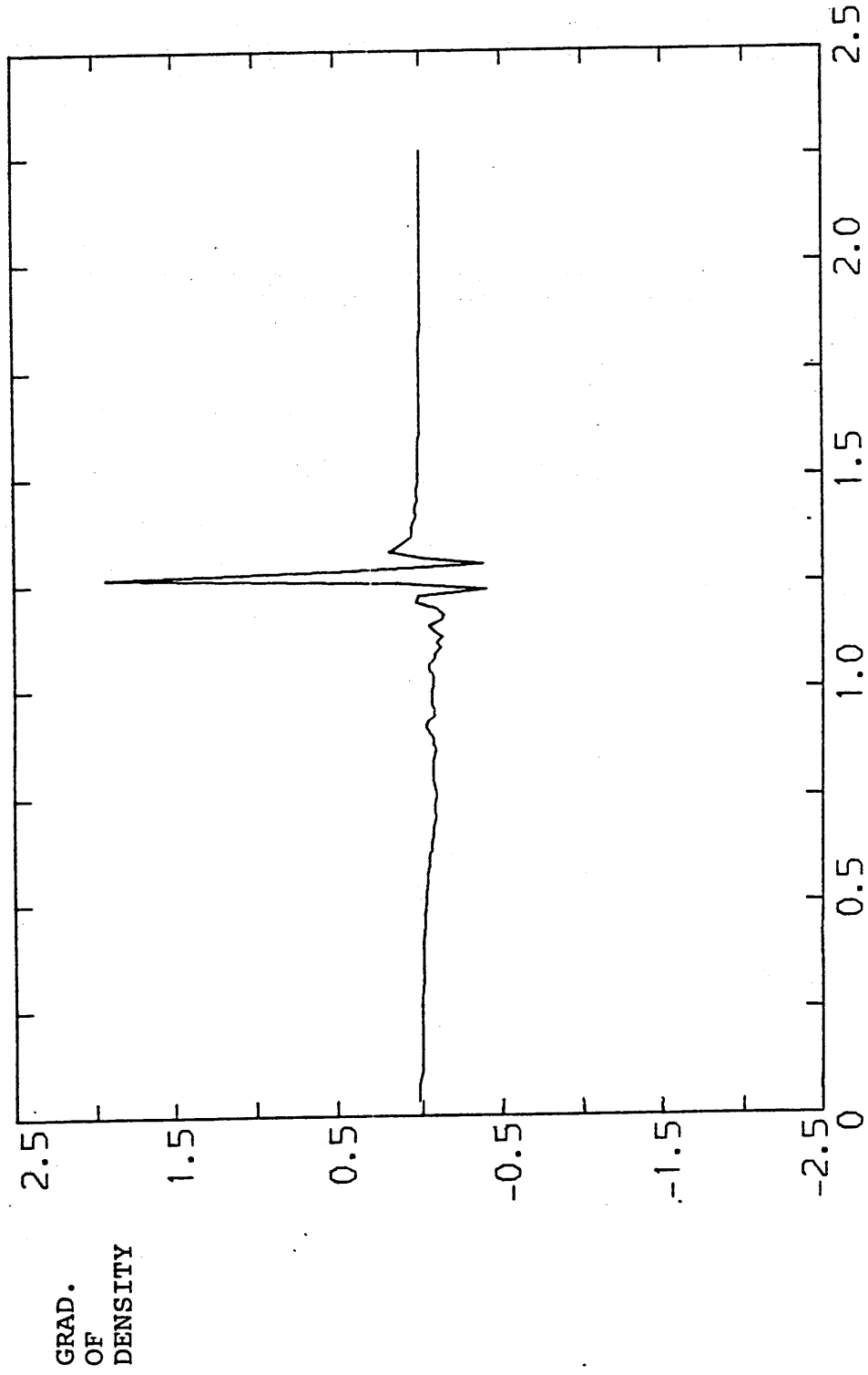

FIGURE 40. Distribution of the gradient of density along the nozzle wall, predicted by the 2D-IN code

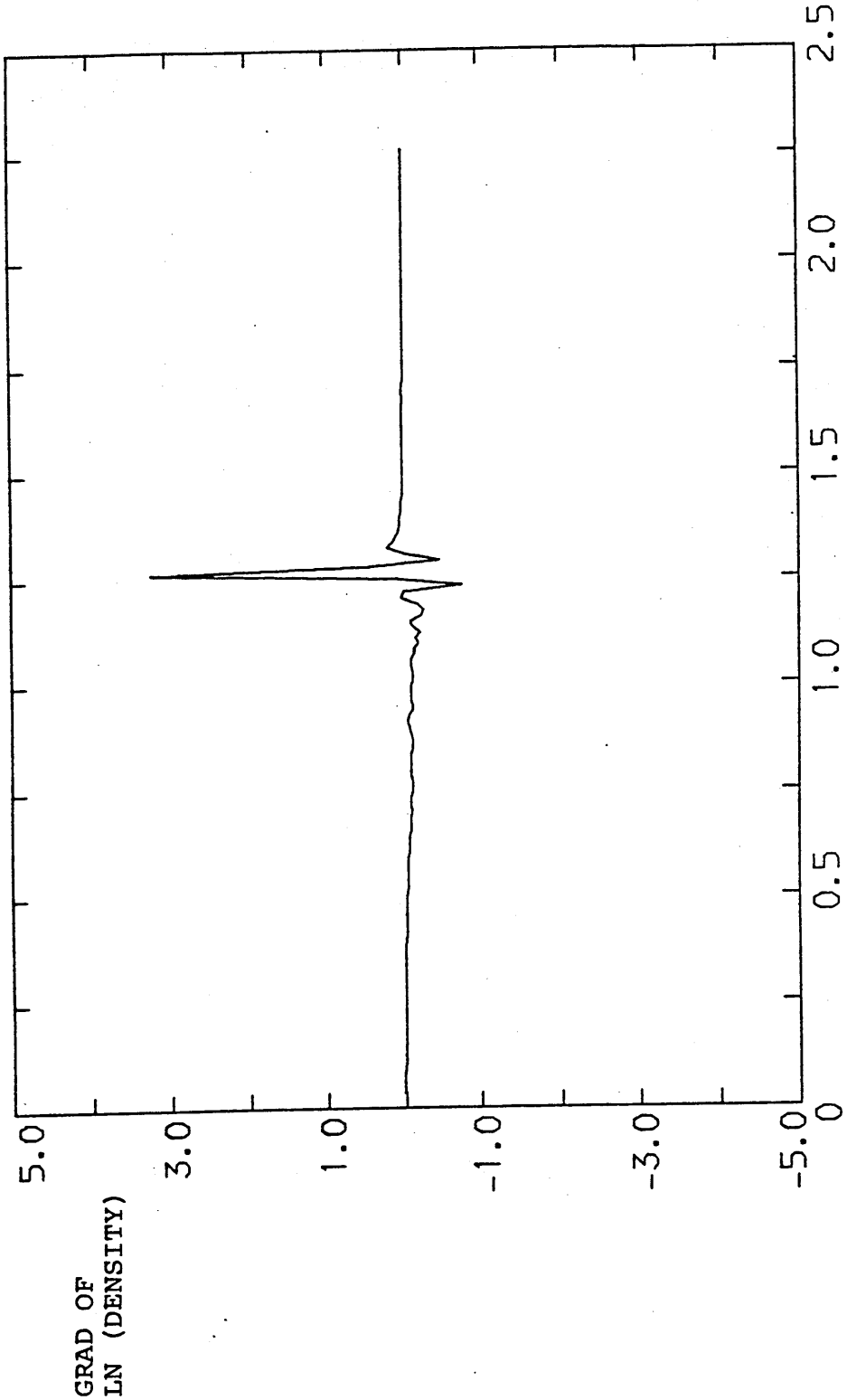

FIGURE 41. Distribution of the gradient of ln (density x blockage), along the nozzle wall, predicted by the 2D-IN code

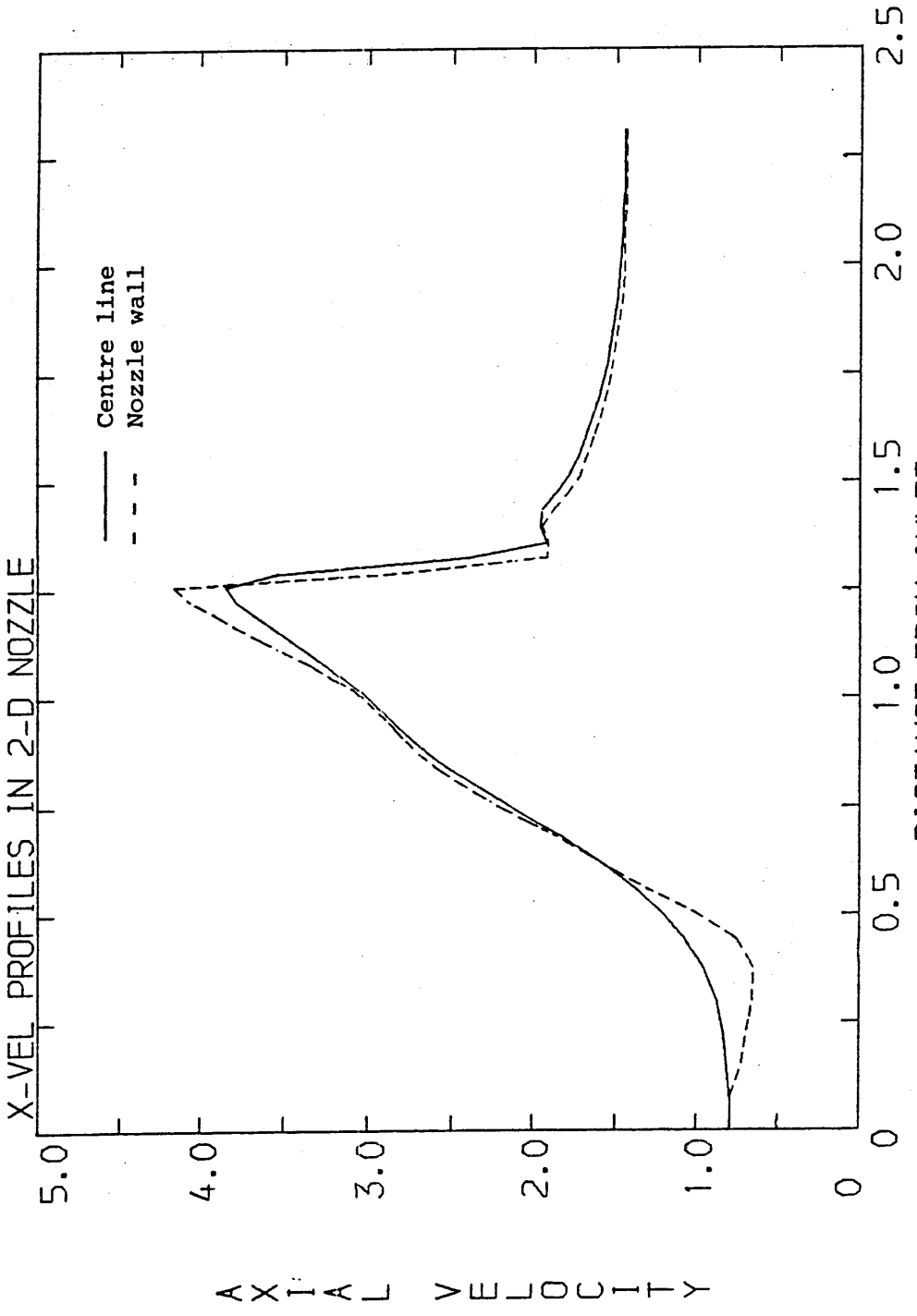

FIGURE 42. Distributions of Axial-Velocity along the Nozzle predicted by the 2D-IN code on a coarse computational grid

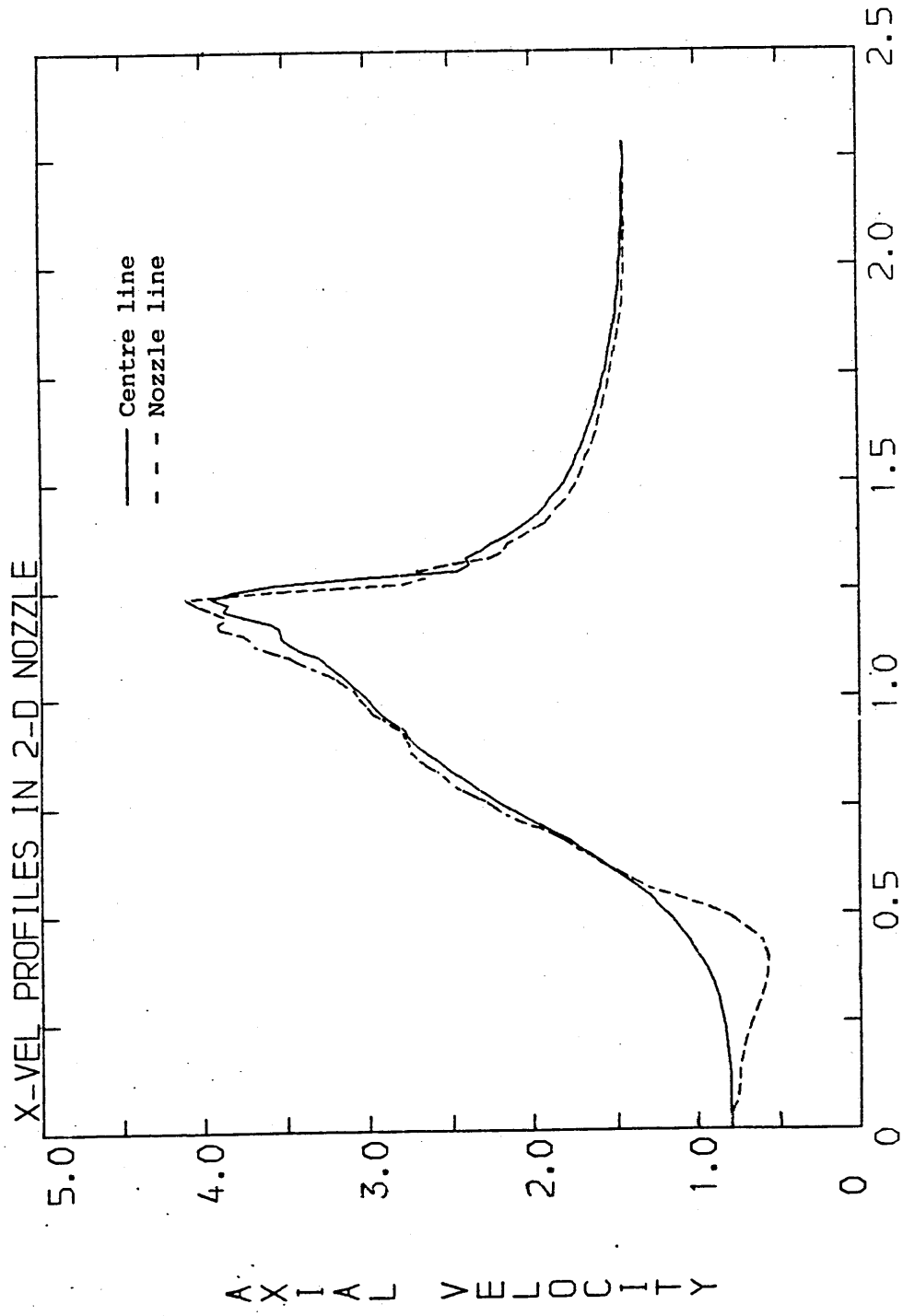

FIGURE 43. Distributions of Axial-Velocity along the Nozzle predicted by the 2D-IN code on a fine computational grid

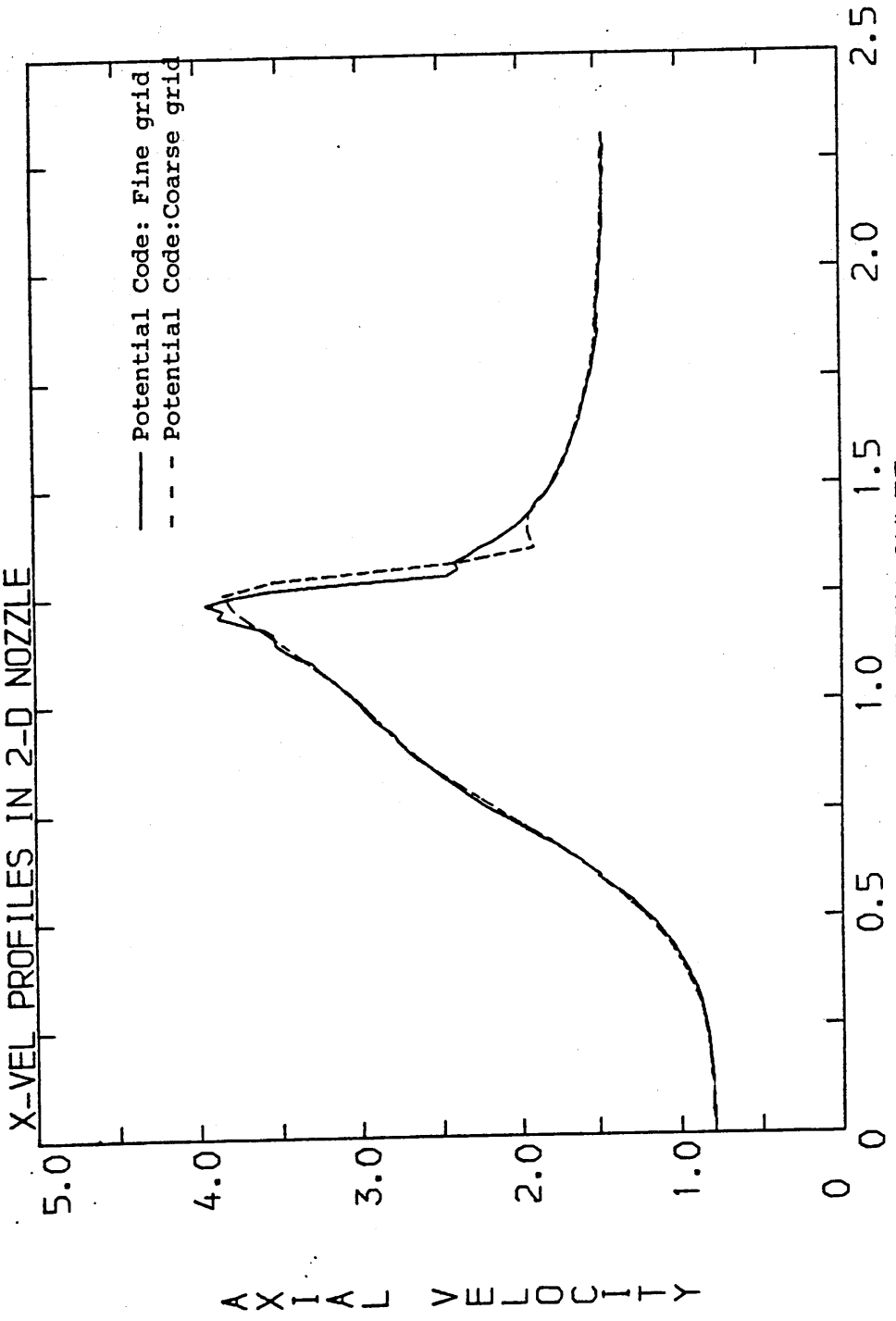

FIGURE 44. Distributions of Axial Velocity along the Nozzle centre-line predicted by the 2D-IN code on both a fine and a coarse grid

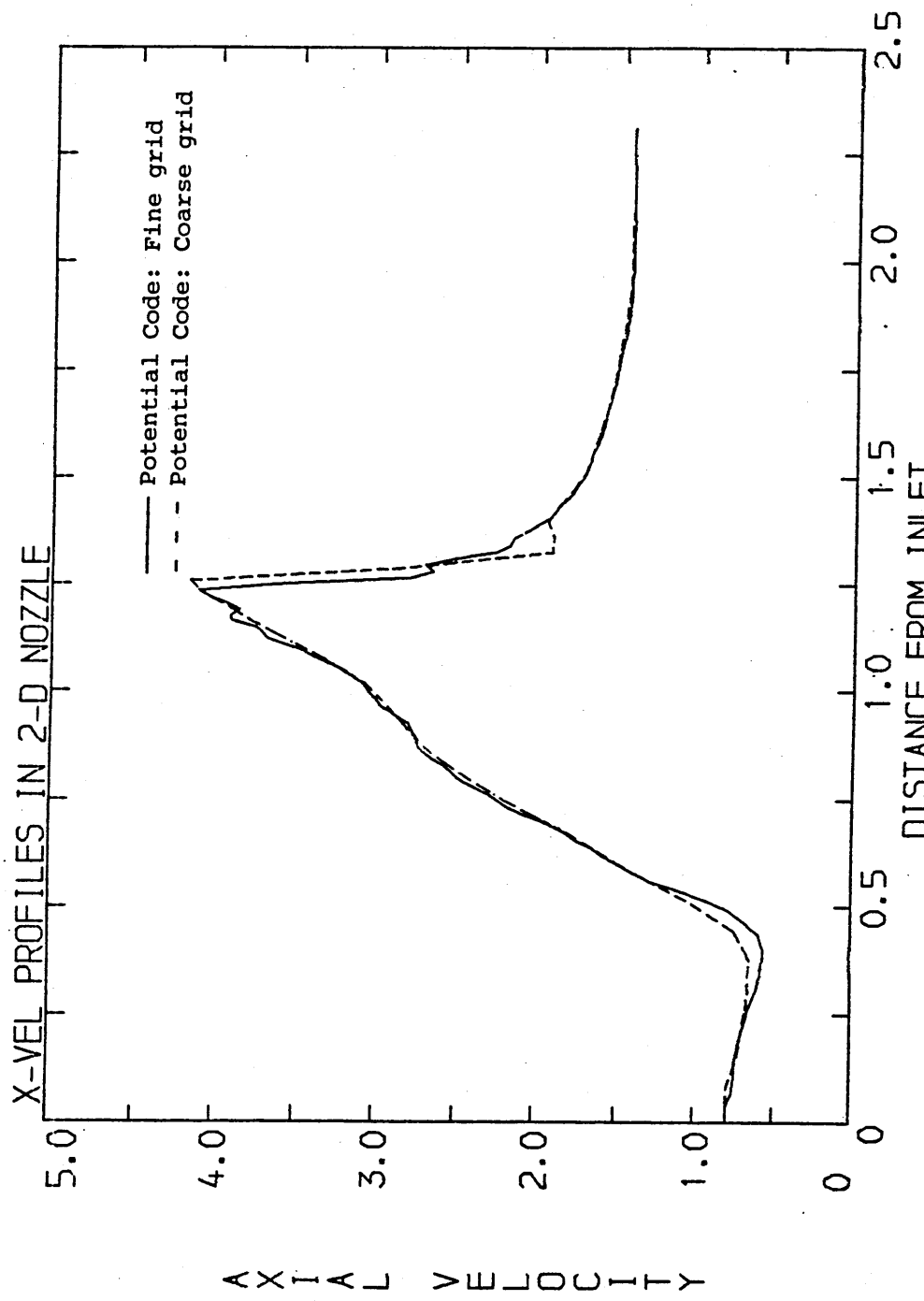

FIGURE 45. Distribtuion of Axial-Velocity along the Nozzle-wall, predicted by the 2D-IN code on both a fine and a coarse grid